

3D NLTE radiative transfer on a Sun-like atmosphere model

DISSERTATION

ZUR ERLANGUNG DES DOKTORGRADES AN DER FAKULTÄT FÜR MATHEMATIK,

INFORMATIK UND NATURWISSENSCHAFTEN

FACHBEREICH PHYSIK

UNIVERSITÄT HAMBURG

VORGELEGT VON

MARIO ARKENBERG

GEBOREN AM

6. JANUAR 1990 IN BERLIN

HAMBURG

2019

Gutachter/innen der Dissertation:	Prof. Dr. Peter Hauschildt Prof. Dr. Sebastian Wolf
Zusammensetzung der Prüfungskommission:	Prof. Dr. Peter Hauschildt Prof. Dr. Sebastian Wolf Prof. Dr. Jochen Liske Prof. Dr. Edward Baron Prof. Dr. Robi Banerjee
Vorsitzende/r der Prüfungskommission:	Prof. Dr. Jochen Liske
Datum der Disputation:	20.08.2019
Vorsitzender Fach-Promotionsausschusses PHYSIK:	Prof. Dr. Michael Potthoff
Leiterdes Fachbereichs PHYSIK:	Prof. Dr.Wolfgang Hansen
Dekander Fakultät MIN:	Prof. Dr. Heinrich Graener

ZUSAMMENFASSUNG

Die Forschung an Trümmerscheiben konnte in dem letzten Jahrhundert substantielle Fortschritte verzeichnen, sowohl in der Beobachtung als auch der Modellierung. Detailliertes Wissen um das Strahlungsfeld des Zentralgestirns ist jedoch Voraussetzung für die genaue Bestimmung der Eigenschaften von Trümmerscheiben; die Generierung entsprechender Spektren sind das ausgesprochene Ziel dieser Doktorarbeit ist.

Der massive Anstieg an verfügbarer Rechenleistung und Speichermöglichkeiten ermöglicht die detaillierte Berechnung von synthetischen Spektren, basierend auf dreidimensionalen magnetohydrodynamischen Strukturen. Im Unterschied zu den weit weniger Ressourcen lastigen, traditionellen eindimensionalen Atmosphärenmodellen können diese dreidimensionalen Modelle, unter anderem, die beobachteten Turbulenzen in der Atmosphäre und auch die Chromosphäre konsistent wieder geben.

Die Existenz von Trümmerscheiben kann bei vielen Hauptreihensternen nachgewiesen werden. Dies gilt insbesondere auch für Sterne des Typs G2. Deshalb können Strahlungstransportrechnungen, die auf dreidimensionalen magnetohydrodynamischen Sonnen-ähnlichen Atmosphärenstrukturen basieren, als geeignete Vorlage für das Strahlungsfeld generischer Sterne des Typs G2 dienen. Folglich stellen diese Modelle einen großen Mehrwert für die weitere Erforschung von Trümmerscheiben dar.

Die Temperatur, die Dichte und der Gasdruck unterscheiden sich in den photosphärischen Schichten im Mittel nur wenig von den Werten der eindimensionalen Model. In den höheren Atmosphärenschichten zeigen sich jedoch die zu erwartenden, signifikanten Abweichungen der genannten Größen.

Der Oberflächenfluss der betrachten dreidimensionalen Struktur variiert merklich und ist im Mittel strickt größer als der Oberflächenfluss der eindimensionalen Atmosphäre. Die Abweichung ist im ultravioletten Wellenlängenbereich besonders ausgeprägt, beträgt jedoch auch im optischen und infraroten Bereich einige Prozent.

Dieses Ergebnis präsentiert jedoch nur das temporäre Strahlungsfeld des magnetohydrodynamischen Modells zu einem willkürlich ausgewählten Zeitpunkt. Es ist daher nicht zu erwarten, dass dieses Ergebnis zwangsläufig repräsentativ ist für den Stern. Gleichwohl liefert das Modell ein sehr nützliches Ergebnis und betont die Relevanz des dreidimensionalen Strahlungstransports für die Trümmerscheibenforschung und andere Bereiche der Astrophysik.

ABSTRACT

The capabilities to observe and model debris disks have substantially increased over the last few decades. The derivation of the disks properties relies, however, on the detailed knowledge of the host star's radiation field.

The drastic increase of computational resources over the last century facilitated the calculation of detailed, synthetic spectra based on three-dimensional magnetohydrodynamic models. In contrast to the computationally inexpensive, more traditional one-dimensional atmosphere models, the enhanced three-dimensional models are capable of representing turbulences on different scales as well as the chromosphere in a consistent manner.

Debris disks are being observed around a variety of main-sequence stars including numerous G2 type stars. The calculation and analysis of detailed synthetic spectra based on a sophisticated three-dimensional Sun-like atmosphere structure may, therefore, serve as a template for the radiation fields of generic G2 type stars and, consequentially, supplies the debris disk research with valuable data which is the expressed scientific goal of this thesis.

In the scope of this work, the layer-averaged mean values of the temperature, density and gas pressure in the photosphere of the models were in good agreement with a comparable one-dimensional solar atmosphere model but unsurprisingly showed significant deviations in the upper layers of their respective atmospheres.

Moreover, the radiation flux of the presented three-dimensional models demonstrated notable surface variations, while their layer-averaged mean value were strictly larger than the corresponding surface flux of the one-dimensional model in all wavelengths ranges. While massive radiation flux deviation can be observed in the ultra-violet wavelength range, the relative radiation flux differences in the optical and infrared are only of the order of several percent.

These results, however, do only present the instantaneous radiation field of the magnetohydrodynamic structure at one arbitrarily chosen point in time which may not necessarily be representative for the stars radiation field at different times. Nonetheless, the models demonstrates meaningful results and stress the importance of a detailed radiative treatment based on three-dimensional atmospheres for debris disk research and the stellar astrophysics in general.

CONTENTS

1	Introduction	1
2	Theory	4
2.1	The particle distribution function	6
2.2	Ideal magnetohydrodynamics	9
2.2.1	Implementation - CO ⁵ BOLD	12
2.3	Radiation Field	13
2.4	Equation of state	15
2.5	Rates and thermodynamic equilibria	16
2.5.1	Radiative Rates	21
2.5.2	Collisional rates	26
2.6	Radiative Transfer	27
2.6.1	Implementation - Phoenix/3D	32
3	Inspection and analysis of data	35
3.1	Hydrodynamic structure	35
3.1.1	Structure 1	36
3.2	Radiative transfer models	42
3.2.1	Model 1	45
3.2.2	Model 2	54
3.3	Model comparison	63
3.3.1	3D model comparison	64
3.3.2	3D to 1D model comparison	72
4	Results and future prospects	77
	List of figures	81
	List of tables	83

Literaturverzeichnis	84
--------------------------------	----

CHAPTER 1

INTRODUCTION

The detection of ever-fainter, smaller or more distant stellar objects and their respective features have been driven by drastic enhancements of telescopes and observation methods over the last few decades.

Debris disks are being detected around a considerable fraction of main-sequence stars and are, therefore, one of many recent research topics substantially benefiting from these improvements. These optically thin, circumstellar disks orbit their host stars at few AU to Kuiper-belt distances and are composed from a mixture of solid bodies exhibiting vastly differing sizes and properties. Assuming the debris disk's dust to be in thermal equilibrium with its host star's radiation field at the typical distances, the dust can be expected to re-emit radiation in the far infrared at about a several hundred-thousand Ångström, see e.g., Krivov (2010).

Detailed knowledge of the host star's radiation field is of utmost importance for the determination of the debris disk's properties, as is true for most indirectly observed objects and their features. Hence, the demand for high quality stellar spectra from simulations and observations alike is enormous and highlights the close interrelationship between the theoretical and experimental astrophysics. The calculation of advanced synthetic spectra with a particular focus on the application to debris disk research is the expressed science goal of this thesis.

The Sun's close proximity to Earth brings about the best opportunity to study the dynamics of a stellar surface. And, even though the extreme physical conditions in and about the Sun prohibit direct measurements of its internal structure, the Sun's radiation carries a vast wealth of information from which many central properties can be deduced. On that account, the Sun's surface has been and is being mapped in great detail for a wide range of wavelengths. By virtue of the varying formation region altitudes of lines and continua in stellar spectra, the Sun's atmosphere can be probed at different altitudes by inspecting these maps at different

wavelengths.

Consequentially, the Sun used to have and is still having an unparalleled impact on the development of sophisticated astrophysical stellar theories, observation instruments and powerful methods for data-analyses.

In the early 19th century, Wollaston (1802) and Fraunhofer (1817), independently, reported the occurrence of dark lines in the Sun's spectrum while investigating the optical properties of prisms and coloured glasses, respectively. This phenomenon was soon related to characteristic properties of atomic and molecular species which led to Kirchhoff's (1862-1863) pioneering treatise "Untersuchungen über das Sonnenspectrum und die Spectren der chemischen Elemente" discussing the Sun's atmosphere chemical composition.

Modern magnetohydrodynamic simulations have proven to generate stellar atmosphere models which emulate the observed dynamics in the Sun's atmosphere very well. For more information on this topic see , e.g., Wedemeyer-Böhm et al. (2012).

While magnetohydrodynamic simulations can produce reasonably detailed hydrodynamic atmosphere models, they usually fail to describe the atmosphere's radiation field thoroughly.

The classical formulation of the radiative transfer problem describing the interaction of light and matter in a "foggy" atmosphere, i.e., including scattering on top of the material's emission and absorption properties, was proposed by Schuster (1905) at the beginning of the 20th century.

Adopting the quantum mechanical description of light and matter, the radiative transfer problem was refined and enhanced over the course of a century. One famous example is the introduction of an operator splitting method by Cannon (1973) overcoming a long standing convergence issue of radiation transfer problems solved by iterative methods.

At the same time, the theory of stellar atmospheres massively benefited from the invention of computers. The rapid evolution of computational resources and the development of advanced numerical methods soon allowed for the computation of atmospheric models in ever-growing detail.

A consistent treatment of radiation, however, comes with significant computational costs and becomes unsustainable in the case of sufficiently resolved, time-dependent, three-dimensional problems.

The radiation field can, nevertheless, be calculated in great detail for *individual temporal snapshots* of such atmosphere simulations. Taking advantage of large, massively parallelised com-

puting facilities available today, Hauschildt and Baron (2006) developed the state of the art 3D NLTE radiative transfer code Phoenix/3D applicable to pre-calculated, static hydrodynamic structures. See their paper series and section 2.6.1 for more details.

The application of Phoenix/3D to a three-dimensional Sun-like magnetohydrodynamic atmosphere model as well as the inspection and analysis of the resulting synthetic spectra are discussed throughout the following thesis.

Among other improvements, the aforementioned models exhibit two distinct advantages over the traditional one-dimensional treatment of stellar atmosphere. First and foremost, these models inherently feature convection, magnetic fields, turbulences and hydrodynamic instabilities. Second, they also allow for a self-consistent simulation of the lower chromosphere. On the one hand, these features can be expected to result in a rather non-uniform radiation field and, therefore, possibly large surface brightness variations. The treatment of the chromosphere, on the other hand, may be anticipated to have a non-vanishing impact on the radiation field in all wavelength ranges, especially so in the ultra-violet.

In these regards, the presented spectra can be understood as a direct upgrade as compared to the one-dimensional models and may enhance today's understanding of stars and their circumstellar companions like the above mentioned debris disks.

The models are, nevertheless, merely the next mile stone on the way to a consistent description of stellar atmospheres. Future work may need to consider the global dynamic of host stars, their activity cycles and their feedback to and from accompanying objects by the means of radiation and magnetic fields. This is all the more true for a fully-consistent simulation of debris disks.

And while only time will tell when the simulation of such in-depth models will become feasible, there is no doubt that step by step progress will be made and ever-better results will be derived.

CHAPTER 2

THEORY

In our endeavour to understand and characterise stellar atmospheres and their radiation fields it is imperative to introduce a number of quantities and equations. While this chapter does not cover all aspects in exhausting detail, it will outline a conceptional framework connecting the most important concepts and quantities of each aspect. For more details consult the books and articles stated below.

The theory of statistical mechanics sets an excellent point of origin for the following discussion and provides us with a set of useful concepts for dealing with thermodynamic systems governed by a huge amount of particles. It relates microscopic properties of atoms, molecules and possibly massless particles like photons to measurable macroscopic quantities. After giving a short overview on the concepts of the *particle distribution function* (section 2.1) and *magneto-hydrodynamics* (section 2.2), the essential aspects of radiative transfer problem (subsection 2.5.1) will be introduced and discussed. The books **Basics of Plasma Astrophysics** (Chiuderi and Velli, 2016) and **Plasma Astrophysics, Part I** (Somov, 2012) serve as main guidelines on the topic of statistical mechanics and plasma astrophysics in connection to the magneto-hydrodynamics. Most notations and information about the radiative transfer problem have been gathered from the textbooks **Theory of stellar atmospheres** (Hubeny and Mihalas, 2014), **Stellar Atmospheres** (Mihalas, 1978) and **Kinetic Theory of Particles and Photons** (Oxenius, 1986) as well as from the paper series **A 3D radiative transfer framework** (Hauschildt and Baron, 2006, 2014) and the theses on this topic by Knop (2007), Berkner (2015) and Aquino (2016).

Notation

In order to avoid misunderstandings for the reader, the non-trivial notation in this work is specified as follows:

- a compact three dimensional integral

$$\int d^3x \equiv \int d^3\vec{x} \equiv \int d\vec{x} \equiv \int \int \int dx_1 dx_2 dx_3 .$$

- the dirac-delta distribution $\delta(x)$

$$\delta(x) = \begin{cases} +\infty, & x = 0 \\ 0, & x \neq 0 \end{cases}$$

and

$$\int_{-\infty}^{\infty} \delta(x) dx = 1.$$

- a (Cartesian) unit vector in the i-th direction \vec{e}_i
- the del or nabla operator acting on variable $\vec{x} = \{x_1, \dots, x_n\}$ in Cartesian coordinates

$$\nabla_{\vec{x}} = \left(\frac{\partial}{\partial x_1}, \dots, \frac{\partial}{\partial x_n} \right) = \sum_{i=1}^n \vec{e}_i \frac{\partial}{\partial x_i}$$

- the dyadic tensor product

$$\vec{c} = \vec{a} \otimes \vec{b} \text{ with } c_{ij} = a_i b_j$$

- the differential surface element $d\vec{S}$

$$d\vec{S} = \vec{n} dS$$

where \vec{n} is the surface normal of the surface element

- a set $\{a_1, a_2, \dots, a_n\}$ holding elements a_1, a_2, \dots, a_n

- an open interval $(a, b) = \{x \in \mathbb{R} \mid a < x < b\}$

- the curvature κ is defined as

$$\kappa_r = \frac{|f(x)''|}{(1 + f(x)'^2)^{\frac{3}{2}}} \quad (2.0.1)$$

where $f(x)''$ is the second and $f(x)'$ is the first derivative of a continuous, two times differentiable function $f(x)$ with respect to x

2.1 The particle distribution function

The concept of the *particle distribution function* $f(t, X)$, where t is time and X is a suitable *phase-space*, can be applied to describe systems under most general conditions, i.e., gas mixtures of interacting massive and massless particles.

It is oftentimes useful to separate the massive from the massless particles with regards to their statistical description, as we shall do in this thesis as well. Consequently, the expression *gas* is used only for particles with non-zero restmass contained in the system.

The internal structures and general properties of a general gas are numerous and complex, yet it is often adequate to simplify their description as is usually the case for statistical thermodynamic theories. In the limit of low gas densities the dynamics of real gases can be approximated very well by the *classical ideal gas*.

*The **classical ideal gas** is composed by indistinguishable, point-like particles exhibiting no internal structure and interacting only through inelastic collisions. (Def. 1) These particles are experiencing no friction and neither attractive nor repulsive forces besides these collisions.*

It can be useful to extent this definition to allow mixed species of gas particles and internal atomic structures.

*In the following work the mixture of (possibly charged) point particle species with atomic level structure will be referred to as **ideal gas**. (Def. 2)*

For simplicity, this chapter only introduces the concept of particle distribution functions for massive particles with a constant *number of particles* N_{tot} , following the books by Somov (2012, Plasma Astrophysics, Part I) and Chiuderi and Velli (2016, Basics of Plasma Astrophysics) as guidelines. A constant number of particles “implies that we are neglecting, for instance, all ionization or recombination processes, that, however, could be easily reintroduced at later stage” (Chiuderi and Velli, 2016, ch. 3 sec. 1) and will not be part of this exemplary summary. Both above-mentioned books work in the (*spatial*) *position velocity phase-space* $X = \{\vec{r}, \vec{v}\}$ with *position* \vec{r} and *velocity* \vec{v} . With respect to the description of the radiative transfer problem below, it is, however more instructive to employ the (*spatial*) *position momentum phase-space* $X = \{\vec{r}, \vec{p}\}$ for the following derivations as it can be used to describe massive and massless particles alike.

The *exact particle distribution functions* $\hat{f}_k(t, X)$ characterises the precise state of an arbitrary

interacting N -particle system and can be represented by

$$\hat{f}_k = \hat{f}_k(t, X) = \hat{f}_k(t, \vec{r}, \vec{p}) = \sum_{i=1}^{N_k} \delta(\vec{r} - \vec{r}_{i,k}(t)) \delta(\vec{p} - \vec{p}_{i,k}(t)). \quad (2.1.1)$$

It relates momentary position $\vec{r}_{i,k}(t)$ and the momentary momentum $\vec{p}_{i,k}(t)$ of particle i of every involved species k at time t in the phase-space $X = \{\vec{r}, \vec{p}\}$.

For massive particles *Liouville's equations* dictate the evolution of the system through the change in the exact particle distribution function

$$\frac{\partial \hat{f}_k}{\partial t} + \frac{\vec{p}}{m_k} \nabla_{\vec{r}} \hat{f}_k + \hat{\vec{F}}_k \nabla_{\vec{p}} \hat{f}_k = 0. \quad (2.1.2)$$

Here the *total force* $\hat{\vec{F}}_k$ depends on the type of interactions between species and m_k denotes the species mass. A closer investigation of this quantity leads to a closure problem and is discussed in more detail in the literature, e.g., Chiuderi and Velli (Basics of Plasma Astrophysics 2016, ch. 3 sec. 2).

Given a full set of initial conditions, we could determine the state of the system for any given time. The exact particle distribution functions are a useful concept for the development of a sound statistical mechanics theory but are prohibitive to deal with due to the enormous number of particles in systems like stellar atmospheres.

A connection to macroscopic quantities, intensive properties in thermodynamic terms, can be established by averaging the exact particle distribution functions in a suitable way. The *particle distribution functions* f_k in the 6-dimensional position momentum phase-space $X = \{\vec{r}, \vec{p}\}$

$$f_k = f_k(t, \vec{r}, \vec{p}) = \frac{1}{\Delta \vec{r} \Delta \vec{p}} \int_{\Delta \vec{r}} d^3 \vec{r} \int_{\Delta \vec{p}} d^3 \vec{p} \hat{f}_k(t, \vec{r}, \vec{p}) \quad (2.1.3)$$

of *species* k emerge as a result for integrating (and averaging) over small volumes $\Delta \vec{r}$ and $\Delta \vec{p}$ centered around \vec{r} and \vec{p} , respectively. Details on this averaging procedure, imposing first constraints on system times-scales and its particle densities, can be found for instance in Somov (2012, ch. 2).

It is defined such that the number of particles in a small volume $\{(\vec{r}, \vec{r} + d^3 \vec{r}), (\vec{p}, \vec{p} + d^3 \vec{p})\}$ in phase-space X at time t can be written as

$$dN_k(t, \vec{r}, \vec{p}) = f_k d^3 \vec{r} d^3 \vec{p}. \quad (2.1.4)$$

It immediately follows that the total number of particles in the system N_{tot} can be written as an integration over the whole phase-space and summing over all species k

$$N_{tot} = \sum_k N_{k,tot} = \sum_k \left(\int \int f_k d^3\vec{r} d^3\vec{p} \right). \quad (2.1.5)$$

We can easily connect physically measurable quantities to the particle distribution functions. The number density n_k of a species k is given by

$$n_k = n_k(t, \vec{r}) = \int f_k d^3\vec{p}. \quad (2.1.6)$$

It is the zeroth-order moment of the species' particle distribution function f_k with respect to momentum \vec{p} and implies that the mass density ρ can be written as

$$\rho = \rho(t, \vec{r}) = \sum_k \rho_k(t, \vec{r}) = \sum_k m_k n_k. \quad (2.1.7)$$

*The **m^{th} -order moment** $M(x)$ of a quantity $\zeta(x)$ with respect to its argument x for a given distribution function $f(x)$ is defined as* (Def. 3)

$$M(x) = \int \zeta(x) f(x) dx \quad (2.1.8)$$

where the order of m is determined by the highest order of multiplicity in argument x for $\zeta(x) \propto \prod_{i=0}^m x$. ⋮

The *statistical average* of a momentum dependent quantity $\zeta(\vec{p})$ can be expressed as

$$\langle \Phi \rangle_k = \frac{\int \zeta(\vec{p}) f_k(t, \vec{r}, \vec{p}) d^3\vec{p}}{\int f_k d^3\vec{p}} = \frac{\int \zeta(\vec{p}) f_k(t, \vec{r}, \vec{p}) d^3\vec{p}}{n_k(t, \vec{r})} \quad (2.1.9)$$

the m th-order moment of the particle distribution function normalised by the zeroth-order moment of the particle distribution function, i.e., the number density n_k .

It follows that the *flow (average particle) velocity* v_i in the i th direction for species k can be expressed as

$$v_{i,k}(t, \vec{r}) = \frac{\langle p_i(t, \vec{r}) \rangle_k}{m_k} \equiv \frac{1}{n_k(t, \vec{r})} \int_{-\infty}^{\infty} \frac{p_i}{m_k} f_k(t, \vec{r}, \vec{p}) d^3\vec{p}. \quad (2.1.10)$$

Here the assumption has been made, that we can write the particle momentum $p_{i,k}$ as the sum of an averaged particle momentum $\langle p_i \rangle_k$ and some random momentum $p_{i,k}^{rand}$, which is dependent

on the particle distribution function. This definition implies that the random motions of the particles are isotropic, i.e., integrating this random momentum over the particle momentum space equates to zero. Therefore we can define the complete fluid velocity of species k as

$$\vec{v}_k = \vec{v}_k(t, \vec{r}) = \sum_{i=1}^3 \frac{\langle p_i(t, \vec{r}) \rangle_k}{m_k} \vec{e}_i \equiv \sum_{i=1}^3 v_{i,k}(t, \vec{r}) \vec{e}_i. \quad (2.1.11)$$

Moreover it is convenient to introduce the *mass flux*

$$\vec{\pi}_k = \rho_k \vec{v}_k \quad (2.1.12)$$

as well as the *momentum flux tensor* for species k

$$\begin{aligned} \Pi_{ij}^k(t, \vec{r}) &= \frac{1}{m_k} \int f_k p_i p_j d^3p \\ &= m_k n_k \left[v_{i,k} v_{j,k} + \frac{\langle p_{i,k}^{rand} p_{j,k}^{rand} \rangle_k}{m_k^2} \right] \\ &= m_k n_k v_{i,k} v_{j,k} + \mathcal{P}_{ij}^k \end{aligned} \quad (2.1.13)$$

both commonly encountered in hydrodynamic theories. Here the (partial-) *pressure tensor*

$$\mathcal{P}_{ij}^k = \frac{\langle p_{i,k}^{rand} p_{j,k}^{rand} \rangle_k}{m_k} \quad (2.1.14)$$

has been introduced, which can be related to thermodynamic pressure and shear processes. The momentum flux tensor can also often expressed in its dyadic form

$$\overset{\leftrightarrow}{\Pi}_k \equiv \rho_k \vec{v}_k \otimes \vec{v}_k + \overset{\leftrightarrow}{\mathcal{P}}_k = \vec{\pi}_k \otimes \vec{v}_k + \overset{\leftrightarrow}{\mathcal{P}}_k. \quad (2.1.15)$$

As mentioned in the introduction of this chapter, we could extend the scope of particle distribution functions to include photons - or other massless particles - by adapting the given framework.

2.2 Ideal magnetohydrodynamics

As indicated before, it is illusory to expect that we can actually obtain a full solution of the problem in terms of exact particle distribution functions for systems such as stellar atmospheres.

The amounts of data required and generated for such a system go far beyond our technical capabilities of today and the foreseeable future. It is, however, feasible to compute detailed models, for a wide range of different systems, using statistical (thermodynamic) theories. As demonstrated in the previous section we can connect the microscopic quantities of the system to macroscopic quantities via particle distribution functions; by doing so we trade details on the level of individual particle information in favour of a more manageable number of information about averaged quantities. Thermodynamic theories have been applied very successfully to a wide range of different systems, justifying the approach and proving its viability.

Vise-versa most observations and measurements determine these macroscopic thermodynamic quantities, especially so in astrophysical context, and enable the symbiotic exchange of information between theory and observations. They test theories, give them constraints and initial conditions and allow the prediction of the systems behaviour, especially in regions and about phenomena that are inaccessible to direct measurements.

“The material in stellar atmospheres is a rarefied gas. Its density in observable layers is so low that it behaves mechanically like an ideal gas” (Hubeny and Mihalas, 2014, p. 21) and is well described by the term *plasma*, i.e., there are a significant number of free electrons in the gas. Furthermore, “at typical temperatures in the solar atmosphere (6000°K) hydrogen is essentially neutral, and the electrons are contributed mainly by the ‘metals’ such as Na, Mg, Al, Si, Ca, and Fe” (Mihalas, 1978, p. 115), which implies that the fraction of electrons in the gas compared to other species is significantly smaller than in hotter stars but still big enough to consider the gas a (partly ionised) plasma. Since the number of free electrons in the atmosphere drastically decreases with falling temperature, there are but a few free electron in cooler star atmospheres (e.g., *M-dwarfs*) while the vast majority of particles consist of neutral elements and/or complex molecules and, consequently, can not be characterised as plasma.

*In many astrophysical contexts the expression **metals** refers to all chemical elements/species except for hydrogen and helium, and must not be confused with the chemical group of metals in the Periodic Table.* (Def. 4)

The stated typical temperature must be understood as a rough, time and spacial averaged, mean temperature at about photospheric altitudes; it is well known and understood that the structure in stellar atmospheres is usually far from uniform and that the kinetic temperatures of the particles varies drastically. “Single-fluid models are the simplest but sufficient approximation to describe many large-scale low-frequency phenomena in astrophysical plasma ” (Somov, 2012,

ch. 12) and thus can be considered a well suited initial point to derive the dynamics of stellar atmospheres. In a process of elaborated approximations and assumption the four *ideal magnetohydrodynamics* equations can be derived from the single-fluid models. In the following *ideal magnetohydrodynamics* will abbreviated MHD. These four equations can be written as:

1. the conservation of mass

$$\frac{\partial \rho}{\partial t} + \vec{\nabla}(\vec{\pi}) = 0, \quad (2.2.1)$$

2. the momentum equation

$$\frac{\partial \vec{\pi}}{\partial t} + \vec{\nabla}(\overset{\leftrightarrow}{\Pi}) = \rho \vec{g} \quad (2.2.2)$$

with the (mechanic and Maxwell) stress tensors

$$\overset{\leftrightarrow}{\Pi} = \underbrace{\vec{\pi} \otimes \vec{v} + (P_{gas})\mathbb{1}}_{\text{mechanic stress}} + \underbrace{\left(\frac{\vec{B}\vec{B}}{2}\right)\mathbb{1} - \vec{B} \otimes \vec{B}}_{\text{Maxwell stress}} \quad (2.2.3)$$

$\vec{B}(t, \vec{r})$ the magnetic field vector and the gravitational acceleration

$$\vec{g} = \vec{g}(t, \vec{r}) = \sum_i \frac{\partial}{\partial r_i} \Phi(\vec{r}), \quad (2.2.4)$$

where $\Phi(\vec{r})$ is the gravitational potential and

$$P_{gas} = P_{gas}(t, \vec{r}) = \sum_{i=j} \mathcal{P}_{ij} \quad (2.2.5)$$

the gas pressure,

3. the conservation of magnetic flux

$$\frac{\partial \vec{B}}{\partial t} + \vec{\nabla}(\vec{v} \otimes \vec{B} - \vec{B} \otimes \vec{v}) = 0, \quad (2.2.6)$$

4. the conservation of total energy density

$$\frac{\partial(\rho e_{tot})}{\partial t} + \vec{\nabla} \left[\left(\rho e_{tot} + P_{gas} + \frac{\vec{B}\vec{B}}{2} \right) \vec{v} - \vec{v}(\vec{B} \otimes \vec{B}) + \vec{F}_{rad} \right] = 0 \quad (2.2.7)$$

with the total energy density defined as

$$\rho e_{tot} = \rho e_{int} + \rho \frac{\vec{v}\vec{v}}{2} + \frac{\vec{B}\vec{B}}{2} + \rho \Phi, \quad (2.2.8)$$

e_{int} being the internal energy and \vec{F}_{rad} being the radiation flux.

The approximations/assumptions involved in deriving the above set of equations include that the gas can be described as

- ideal (see definition 2),
- nonviscous but compressible (explicitly excluding frictional forces),
- electrically quasi-neutral (reasonable globally but not necessarily locally),
- non-relativistic (not a problem for most parts of a stellar atmosphere although we can expect the occurrence of relativistic electron/particle velocities in the chromosphere and above),
- the fluid velocity of all particles in the gas can be represented by only one fictitious particle species (one fluid approximation), implying chemical homogeneity of the gas throughout the system (potentially inaccurate since the chemical composition of the gas is highly correlated to the local temperatures and pressure)

Furthermore, the time- and length- scales of interest have to be **macroscopic**, i.e., many orders of magnitude larger than their respective microscopic scales on the ion and electron levels.

These approximations serve the purpose to reduce the complexity of the system's description, apply prior knowledge and experience for the benefit of feasibility and can often be used to generate very solid results, despite a severe reduction in detail.

2.2.1 Implementation - CO⁵BOLD

CO⁵BOLD (Freytag et al., 2012) is a “COnservative CODE for the COmputation of COmpressible COnvection in a BOx of L Dimensions with L = 2, 3”. It numerically solves the time-dependent MHD equations, coupled with a non-local radiation transport. Various simulation for Sun-like stellar atmospheres were generated and claimed to “deserve the label *realistic* because

they reproduce the various observables very well” (Wedemeyer-Böhm et al., 2012). These models served as input for the “3D multi-level NLTE radiative transfer framework” **PHOENIX/3D** (Hauschildt and Baron, 2014), see section 2.6.1.

2.3 Radiation Field

As mentioned in chapter section 2.1 the particle distribution function can in principle be used to describe massless particles (e.g., photons) as well as massive particles. However, the properties of the radiation field can not be covered by the one-fluid approximation that was used to derive the MHD equations for the dynamics of the gas. Since we are interested in the detailed behaviour of the radiation field, it is useful to introduce the photon distribution function $f_R(t, \vec{x}, \vec{p})$, explicitly and separately representing the photonic part of the particle distribution functions $f_k(t, \vec{r}, \vec{p})$.

As is true for its massive particle counterpart the photon distribution function is not observable; but it carries the information about the statistical likelihood of encountering a number of photons of a given momentum \vec{p} , and thus propagation direction $\vec{n} = \vec{p}/\sqrt{(\vec{p})^2}$, at a given point in space \vec{r} and time t .

The number of photons crossing an orientated surface element $d\vec{S}$ in time dt can be expressed as

$$dN_{\text{photon}} = f_R(t, \vec{r}, \vec{p}) (c \cdot dt)(d\vec{S} \cdot d^3\vec{p}), \quad (2.3.1)$$

so that the transported differential energy is given by

$$dE = c \cdot p \cdot dN_{\text{photon}}, \quad (2.3.2)$$

where $p = \sqrt{(\vec{p})^2}$ is the absolute value of the momentum and $c \cdot p$ the energy of a photon with this momentum moving with the (vacuum) speed of light c . It is more convenient to write its dependencies in terms of a wavelength $\lambda = \frac{h}{p}$, or frequency $\nu = \frac{cp}{h}$, using the Planck constant h , and the solid angle $d\vec{\Omega}$ around the propagation direction \vec{n} by applying the transformation

$$d^3\vec{p} = p^2 dp d\vec{\Omega} = -\frac{h^3}{\lambda^4} d\lambda d\vec{\Omega}$$

instead of using the photons momenta \vec{p} . It is also common practice for dealing with the radiative transfer problem to express the radiation field and connected quantities in terms of the

so-called *specific intensity* $I(t, \vec{r}, \vec{p})$ instead of using the photon distribution function. The specific intensity is defined as the proportionality factor for the differential change of the energy dE transported by radiation going through the surface area $d\vec{S}$ into solid angle $d\Omega$ for wavelength $d\lambda$ in time dt .

$$\begin{aligned} dE &= -\frac{c^2 h^4}{\lambda^5} f_R(t, \vec{r}, \lambda, \vec{n}) \left(d\vec{S} \cdot d\vec{\Omega} \right) d\lambda dt \\ &= I(t, \vec{r}, \lambda, \vec{n}) \left(d\vec{S} \cdot d\vec{\Omega} \right) d\lambda dt \end{aligned} \quad (2.3.3)$$

From the first three order moments of the massive particle distribution functions we were able to derive central quantities for a dynamical description of our system. Hence, we can expect the first order moments of the specific intensity to be of great interest for a elaborate characterisation of the radiation field. The zeroth-order moment of the specific intensity

$$J(t, \vec{r}, \lambda) = \frac{1}{4\pi} \oint I(t, \vec{r}, \lambda, \vec{n}) d\vec{\Omega} \quad (2.3.4)$$

is called the *mean intensity* $J(t, \vec{r}, \lambda)$ which is the solid angle averaged intensity of the radiation field. For the rest of this section the moments of the specific intensity will be taken with respect to the propagation direction \vec{n} . As we shall see the mean intensity is a valuable choice for the description of radiation and its transport through media. Another prominent quantity, called *monochromatic radiative flux* $\vec{F}(t, \vec{r}, \lambda)$, can be acquired from the first-order moment of the specific intensity.

$$\vec{F}(t, \vec{r}, \lambda) = \oint \vec{n} I(t, \vec{r}, \lambda, \vec{n}) d\vec{\Omega} \quad (2.3.5)$$

It gives us a qualitative measure of energy flow in a given wavelength interval $(\lambda, \lambda + d\lambda)$ for propagation direction \vec{n} of the radiation field, so that $\vec{F} d\vec{S}$ is the net rate of energy flow through the surface area $d\vec{S}$. The “flux...is, in fact, nothing more than the contribution of the pencil of radiation moving in direction \vec{n} to the net energy flux” (Mihalas, 1978, p. 9). We can see that the flux is similar in construction, meaning and importance to the average fluid velocity \vec{v}_k which is the analogue to the first order moment of the massive particle distribution function f_k . Moreover, we already saw the radiative flux being considered in the conservation of total energy of the MHD equations as another contribution to the total energy of the system.

From the second-order moment of the specific intensity with respect to the solid angle we can

derive the *radiation pressure tensor*

$$\vec{P}_{rad}(t, \vec{r}, \lambda) = \frac{1}{c} \oint \vec{n} \otimes \vec{n} I(t, \vec{r}, \lambda, \vec{n}) d\vec{\Omega} \quad (2.3.6)$$

The components of this tensor $P_{i,j}^{rad}$ give “the net rate of transport of the j th component of photon momentum of” wavelength λ “through a unit area perpendicular to the i th coordinate axis, per unit time” (Hubeny and Mihalas, 2014) and are the equivalent to the pressure tensor for massive particles, both in meaning and importance.

Having introduced these quantities we need to look at the interaction and effects of the radiation field on matter properties and vice versa.

2.4 Equation of state

The *equation of state* (abbreviated EOS) describes the connection between different intensive thermodynamic variables and the chemical composition of the system. For any complete set of thermodynamic variables, like gas pressure P_{gas} , density ρ and temperature T , there exists a relation \mathfrak{r} with

$$\mathfrak{r}(P_{gas}, \rho, T) = 0 \quad (2.4.1)$$

that can be used to describe the dynamics of a system, i.e., a maximum two of these three variables are independent from each other. For the ideal gas, as defined in definition 2, in thermal equilibrium we can express the total gas pressure P_{gas} through density and temperature

$$P_{gas} = \frac{\mathcal{R}}{\bar{\mu}} \rho T. \quad (2.4.2)$$

Here \mathcal{R} denotes the *ideal gas constant* and $\bar{\mu}$ is the mean molecular mass of the gas

$$\bar{\mu} = \frac{\bar{m}}{m_H}, \quad (2.4.3)$$

where the mean weight \bar{m} can be expressed as number density weighted sum over all species

$$\bar{m} = \frac{n_e m_e + \sum_{k \neq e} n_k m_k}{n_e + \sum_{k \neq e} n_k}. \quad (2.4.4)$$

Moreover, m_H and m_e describe the rest mass of the hydrogen atom and the electron, respec-

tively. The former expression hints at the singular importance of electrons e in the sum over all species k on the equation of states. Although their total mass only equates to a tiny fraction of the total mass in typical systems, their total number can exceed the number of all other species in fully ionized plasma. The total gas pressure can be written as the sum over all partial pressures

$$P_{gas} = \sum_k \sum_j P_{gas,k,j} \quad (2.4.5)$$

for all species k and ionisation stages j .

2.5 Rates and thermodynamic equilibria

With the knowledge gained from the equation of state we can have a closer look at the system's processes, their probabilities and occurrence rates.

Both radiative and collisional processes redistribute energy from one source to another by transferring momentum, exciting and de-exciting internal degrees of freedom, ionising particles or the creation and destruction of particles. While sharing these properties, the typical scales and detailed mechanisms between radiative and collisional processes differ considerably making a distinction valuable and necessary.

“The number density of particles of a given (bound or free) state i of chemical species k will change in time according to the net flux of particles through the volume and the net rate at which particles are brought from other states” i' “, by radiative and collisional processes” (Mihalas, 1978, pp. 127,128) and, thus, its evolution may be written as a continuity equation

$$\left(\frac{\partial n_{i,k}}{\partial t} \right) + \vec{\nabla} \cdot (n_{i,k} \vec{v}) = \sum_{i' \neq i} (n_{i',k} \mathfrak{P}_{i',i,k} - n_{i,k} \mathfrak{P}_{i,i',k}) . \quad (2.5.1)$$

Here $\mathfrak{P}_{i,i',k}$ denotes the total rate, i.e. the sum over all rates of contributing processes, from state i to state i' for the species k . The hydrodynamic continuity eq. (2.2.1) (conservation of mass) can be restored by summing over all states i of the species k , multiplying the equations by their mass m_k and then summing over all species. It follows that we need to find a way to express these rates and to connect them to their quantum mechanical origin, i.e. cross sections, transition probabilities and the corresponding energy flow driving the processes.

It is common practice in stellar atmosphere theories to search for a steady state solution of a static atmosphere. In steady state the number density is constant in time and therefore $\frac{\partial n_{i,k}}{\partial t} = 0$,

while in a static atmosphere there is no macroscopic bulk flow, thus, $\vec{\nabla}(n_{i,k}\vec{v}) = 0$. Consequently, eq. (2.5.1) reduces to its right-hand side, i.e., a balance equation between the up- and downwards rates (and their number densities). Even though stellar atmospheres tend to be dynamic rather than static, the typical dynamical time-scales of atmospheric systems are often huge in comparison to the corresponding time-scales for collisional and radiative processes.

While the left-hand side of this equation primarily describes the macroscopic dynamics of the system, the right-hand side involves the microscopic processes. Thus it is often reasonable to drop the left-hand side of eq. (2.5.1) when calculating the radiation field of stellar atmospheres. This leaves us with a general form of the rate equations applied in many radiative transfer problems

$$\sum_{i' \neq i,k} (n_{i',k} \mathfrak{P}_{i',i,k} - n_{i,k} \mathfrak{P}_{i,i',k}) = 0. \quad (2.5.2)$$

Equation (2.5.2) is still quite general as we have yet to specify the nature of the participating processes. Therefore, it is useful to throw a glance at possible simplifications and their consequences.

The concept of *detailed balance* is of significant importance in this regard.

*A process is said to be in **detailed balance** if the rate at which a process occurs is exactly balanced by the rate at which its inverse process occurs, implying that a set of processes can be in detailed balance while others are not.* (Def. 5)

If all processes considered in the rate equation were in detailed balance, the solution of the equation would be trivial as any process would be counteracted by an inverse process. For example, collisional processes are (close to being) in detailed balance if the velocity distribution of (all) massive particles can be approximated sufficiently well by an equilibrium distribution.

It can be shown that the assumption of a Maxwellian velocity distribution for all massive particles is indeed well justified in most stellar atmospheres, see, e.g., Mihalas (1978, pp. 121,122), and we can consequently assign a kinetic temperature value T_k to each species k in the system. The *Maxwell-Boltzmann* distribution of velocity components $f_k^{\text{MB}}(t, w_i, T_k)$ is then characterised by the function

$$f_k^{\text{MB}}(t, w_i, T_k) = \left(\frac{m_k}{2\pi k_B T_k} \right)^{1/2} \exp \left(\frac{-m_k w_i^2}{2k_B T_k} \right), \quad (2.5.3)$$

where k_B is the Boltzmann constant and w_i the particle velocity component in the i -th direction (not to be confused with the fluid velocity v_i), assuming the gas can be described as the ideal

gas defined earlier (see definition 2).

It immediately follows that the distribution of the velocity vector can be written as

$$f_k^{\text{MB}}(t, \vec{w}, T_k) = \prod_i [f_k^{\text{MB}}(t, w_i, T_k)] \quad (2.5.4)$$

As previously mentioned, electrons bear a non-negligible fraction of the overall number of particles in moderate to high temperature stellar atmospheres and play a crucial part in equilibrating the thermal pools of the different species. Given a comparable kinetic temperature T_e , and, therefore, energy, the resulting electron velocities are higher than any other species' velocities, resulting in electrons being the most frequent collision partner. Apparently, this is not the case for cool atmospheres as there are usually too few free electrons in the gas mixture.

Thus, free electrons can serve as a mediator for collisional processes between any massive particle species, equilibrating their individual kinetic temperatures $T_k \approx T_e$, i.e., all massive particles share one unique temperature T . This greatly reduces the complexity of many related quantities and equations while enabling us to define a gas temperature.

Note that molecules may behave differently as additional degrees of freedom allow for efficient energy transfer channels outside of mechanical translations considered above. The chemical composition of Sun-like stellar atmosphere is dominated by hydrogen and atomic species and there is little to no abundance of (complex) molecules. Treating molecules in a rigorous way would, accordingly, have little impact on the overall scheme of velocity distribution and can usually be neglected.

*A region of a system is said to be in **strict local thermodynamic equilibrium** if all processes are (sufficiently close to being) in detailed balance and if, additionally, all massive particle velocities can be characterised well by (Maxwell-Boltzmann) thermal distributions corresponding to one unique temperature.* (Def. 6)

Internal and external forces may lead to local changes of the material properties, causing adjacent regions to potentially have slightly different detailed balances and allowing for locally differing temperatures.

This assumption allows us to derive a number of important relations well suited to characterise the internal properties of a gas mixture and its radiation field. For ease of notation we will introduce the number density $n_{i,j,k}^*$ of species k in excited state i of ionisation stage j . The asterisk on the number densities indicates that these number densities were computed under the assumption of (strict) local thermodynamic equilibrium.

Instead of solving the rate eq. (2.5.2) directly, the *Boltzmann law* can be applied to express the fraction of the population number $n_{i,j,k}^*$ of species k in excitation level i of ionisation stage j relative to the population number of the same species in another excitation level i' . Various synonyms can be found and are being used in the literature for the population number as it can be understood as the number density for a given state.

$$\frac{n_{i',j,k}^*}{n_{i,j,k}^*} = \frac{g_{i',j,k}}{g_{i,j,k}} \exp \left(\frac{-(\chi_{i',j,k} - \chi_{i,j,k})}{k_B T} \right) \quad (2.5.5)$$

The statistical weight $g_{i,j,k}$ accounts for possible degenerate levels in the species atomic structure. We refer to the ground state with $i = 0$ of the respective ionisation stage for the considered species and let $\chi_{i,j,k}$ denote the excitation energy relative to the ground state of this ionisation stage.

If there are ionisation stages for a given atomic species, it is apparent that there “exists a continuum of levels in which the electron is unbound and has a nonzero kinetic energy” (Mihalas, 1978). The ionisation potential $\zeta_{j,k}$ of ionisation stage j for atomic species k is defined to be the energy required to excite the electron from the ground level to such an unbound state.

The *Saha ionisation equation*

$$\frac{n_{0,j+1,k}^*}{n_{0,j,k}^*} = \frac{2}{n_e} \left(\frac{2\pi m_e k_B T}{h^2} \right)^{3/2} \left(\frac{g_{0,j+1,k}}{g_{0,j,k}} \right) \exp \left(\frac{-\zeta_{j,k}}{k_B T} \right), \quad (2.5.6)$$

relates the population numbers of two consecutive ionisation stages $n_{0,j+1,k}^*$ and $n_{0,j,k}^*$ in electronic ground state to their respective statistical weights, the ionisation potential, the temperature and the electron number density, which changes in ionisation and recombination processes.

Combining the Saha ionisation equation with the Boltzmann law a expression can be derived for the number density $n_{i,j,k}^*$ in any given excitation level i and ionisation stage j and for each species k . The most common form of this equation is given by

$$n_{i,j,k}^* = n_e n_{0,j+1,k} \Phi_{i,j,k}(T). \quad (2.5.7)$$

It highlights the dependencies on the (actual) electron number density as well as the total number density of the next higher ionisation stage $j + 1$ and masks the statistical aspects and constants involved in the *partition function* $\Phi_{i,j,k}(T)$. An explicit representation of this function

can be formulated as

$$\Phi_{i,j,k}(T) = \frac{g_{i,j,k}}{g_{0,j+1,k}} \left(\frac{h^2}{2\pi m_e k T} \right)^{2/3} \exp \left(\frac{\zeta_{j,k} - \chi_{i,j,k}}{k_B T} \right) \quad (2.5.8)$$

for which a detailed derivation can be found in e.g., Hubeny and Mihalas (2014, pp. 88-94).

Yet another well known concept of thermodynamic theories is the *thermodynamic equilibrium*.

*A perfectly isolated system filled with ideal gas of one particle species, experiencing neither internal- nor external- forces, inevitably develops towards its **thermodynamic equilibrium** (abbreviated TE) state, making the system macroscopically uniform in space and time and ensuring detailed balance between all processes.* (Def. 7)

Any process generating deviations from this equilibrium will be counteracted by other processes in the system and it can be shown that “even an extremely small departure from the equilibrium distribution implies an enormous reduction in the thermodynamic probability, and this implies that we will almost never observe a state that differs even slightly from the equilibrium state” (Mihalas and Mihalas, 2013, ch. 1 sec. 3). In TE the radiation field inside this closed system is “uniform, isotropic, time-independent and its frequency distribution is given by the Planck function” (Mihalas, 1978, p. 7)

$$B(\lambda, T) \equiv B_\lambda(T) = \frac{2hc^2}{\lambda^5} \left[\exp \left(-\frac{hc}{\lambda k_B T} \right) \right]. \quad (2.5.9)$$

Over and above eqs. (2.5.5) to (2.5.7) are strictly valid for a system in TE as all conditions are exactly met.

Contradicting the assumptions above, we have to accept that some processes may deviate from the assumptions of strict (local) thermodynamic equilibrium but, nevertheless, we can expect a stable stellar atmospheres to be in a statistical equilibrium. Radiative scattering processes, for example, are able to couple the radiation field of spatially disjoint regions potentially which may not share the same thermodynamic properties and, thereby, can add a explicit radiation field dependence to the formerly well defined thermal radiation produced in its local environment.

Local thermodynamic equilibrium (abbreviated LTE) commonly includes scattering (extending definition 6) by allowing the radiation field to depend on the local thermal radiation given by the Planck function and the radiation field itself. (Def. 8)

While there are prominent examples of systems - like our Sun's photosphere - that can be described and understood rather well as a system in LTE, there is no reason to generally assume LTE conditions to be a reasonable specification of a stellar atmosphere. Unfortunately, it is hard to estimate if the LTE assumption is well justified for a given atmosphere or atomic/molecular species before a detailed *non-local thermodynamic equilibrium* (abbreviated NLTE or non-LTE) calculation/analysis has been executed. More often than not we find good to excellent agreement between observations and models in LTE for a number of species, spectral features or atmospheric region while their agreement is questionable in other cases.

The term **non-local thermodynamic equilibrium** is used to characterise systems or processes that can not be sufficiently well described by LTE condition, different species may exhibit significantly different kinetic temperatures, a species velocity distribution may be non-thermal distribution, radiative processes may show strong non-locality and drive the population numbers away from their thermal distribution, etcetera. (Def. 9)

It is oftentimes useful to measure the deviation from the LTE conditions and hence we define *departure coefficient* (first introduced by Menzel and Cillié (1937)) as the fraction of the *actual* population number n_i and its respective LTE value n_i^*

$$b_i = \frac{n_i}{n_i^*} \quad (2.5.10)$$

when dealing with NLTE conditions. Consequentially, if the departure coefficient b_i deviate notably from unity the involved processes are not well described by the local detailed balance imposed from the LTE.

2.5.1 Radiative Rates

There are different kinds of excitation mechanisms that we can expect to see in a system involving colliding particles and radiation, thus we need to have a look at the most important processes in the regime of stellar atmospheres and discuss their origin and their influence on the

systems properties.

In section 2.3 we introduced the specific intensity $I(t, \vec{r}, \lambda, \vec{n})$ and its first three moments, explained the concepts of thermodynamic equilibrium, local thermodynamic equilibrium, non-local thermodynamic equilibrium and derived the rate equation from a conservation equation in steady state for a static atmosphere.

In the following subsections a connection between the radiative and collisional rates, the radiation field and the systems thermodynamic properties will be presented. A detailed discussion on this topic can readily be found in many textbooks, e.g., Mihalas (1978).

Transitions produced by radiative processes can be differentiated into four groups, namely *bound-bound*, *bound-free*, *free-free transitions* and *photon scattering*.

Neither scattering processes nor free-free transitions contribute directly to the rate equation but are crucial for the description and propagation of radiation and will thus be introduced here along with the other radiative absorption and emission processes. In general, we can describe the rates at which certain transitions occur in terms of a cross section (containing a transition strength and a trigger probability distribution) and a distribution function characterising the particles inducing the transitions.

A prominent example for transition strengths are the *Einstein-coefficients*. Here and for the rest of this section the state corresponding to level l is energetically lower then the energy associated with the upper level u . It can be shown that the Einstein-coefficients for spontaneous emission $A_{u,l}$, for stimulated emission $B_{u,l}$ and for stimulated absorption $B_{l,u}$ follow the relations

$$A_{u,l} \equiv \frac{2hc}{\lambda_{u,l}^3} B_{u,l} \quad (2.5.11)$$

and

$$g_l B_{l,u} \equiv g_u B_{u,l}, \quad (2.5.12)$$

, e.g., see Mihalas (1978, pp. 78,79).

The probability of absorbing or emitting a photon of a given wavelength additionally depends on their respective *profile functions*. Both, the absorption profile $\phi_{l,u}(\lambda, \vec{n})$ and emission profile $\psi_{u,l}(\lambda, \vec{n})$

$$\int \oint \{\phi_{l,u}, \psi_{u,l}\}(\lambda, \vec{n}) (d\vec{\Omega}/4\pi) d\lambda = 1$$

are normalised to one, so that $\{\phi_{l,u}(\lambda, \vec{n}), \psi_{u,l}(\lambda, \vec{n})\} d\vec{\Omega} d\lambda$ can be understood as the (conditional) probability of triggering the transition from level $\{l \rightarrow u, u \rightarrow l\}$ within a given

wavelength interval $(\lambda, \lambda + d\lambda)$ and in a solid angle $d\vec{\Omega}$ around the propagation direction \vec{n} . The exact shape of the profile function strongly depends on the environment and on the processes contributing to the transition related to this profile function and can be represented as a convolution of the profile functions representative for each effect.

Bound-bound and bound-free transitions

The (de-)excitation of an electron from bound electronic state i to another bound electronic state u by radiation with a corresponding excitation energy is called bound-bound transition. The rate for an radiative upwards (or absorption) process for a bound-bound transition from level i to u can be expressed by

$$R_{l,u} = B_{l,u} \int_0^\infty \frac{\lambda^2}{4\pi c} \oint I_\lambda(\vec{n}) \phi_{l,u}(\lambda, \vec{n}) d\vec{\Omega} d\lambda, \quad (2.5.13)$$

utilising the above introduced Einstein-coefficient $B_{l,u}$. In static media the absorption profile is isotropic and, thus, using the mean intensity J_λ introduced in section 2.3, defining the absorption cross section $\alpha_{l,u}(\lambda) = \frac{hc}{4\pi} \frac{\lambda}{c} B_{l,u} \Phi_{l,u}(\lambda)$ and integrating over all solid angles reduces the previous expression to

$$R_{l,u} = \frac{4\pi}{hc} \int_0^\infty \alpha_{l,u}(\lambda) J_\lambda \lambda d\lambda. \quad (2.5.14)$$

Here $\Phi_{l,u}(\lambda) = \oint \phi_{l,u}(\lambda, \vec{n}) d\vec{\Omega}$ is the angle averaged/independent absorption profile function. Using cross sections instead of Einstein-coefficients in the description allows the direct comparison with other rates later on.

Downward (or emission) processes may occur by the means of spontaneous and stimulated de-excitation. Therefore we have to write the radiative rate for bound-bound emission

$$R'_{u,l} = A_{u,l} + B_{u,l} \int_0^\infty \frac{\lambda^2}{4\pi c} \oint I_\lambda(\vec{n}) \psi_{u,l}(\lambda, \vec{n}) d\vec{\Omega} d\lambda \quad (2.5.15)$$

as the sum of spontaneous and stimulated processes. This expression can be brought into a similar shape as the upward rates by applying the Einstein-coefficient relations eq. (2.5.11) and 2.5.12, using the connection between the statistical weights and defining the emission cross section $\alpha_{l,u}(\lambda) = \frac{hc}{4\pi} \frac{\lambda}{c} B_{l,u} \Psi_{u,l}(\lambda)$ with the angle averaged/independent emission profile function $\Psi_{u,l}(\lambda)$. Furthermore, it is possible to include bound-free transitions into this formulation

leaving us with the *modified radiative downward (emission) rates*

$$R_{u,l} = \frac{4\pi}{hc} \int_0^\infty \alpha_{u,l}(\lambda) \left(\frac{2hc^2}{\lambda^5} + J_\lambda \right) \exp\left(-\frac{hc}{k\lambda T}\right) \lambda d\lambda \quad (2.5.16)$$

commonly used in radiative transfer problems.

Processes involving a bound electronic state of an atom and a free electron are referred to as bound-free transitions. An atom or a molecule absorbing a photon with an energy bigger than the electron's binding energy in a given bound state is being ionised by unbinding the electron and redistributing excessive energy to the electrons velocity \vec{v}_e .

This ion may be in its new ground state or in an excited state u . This process is called *photoionisation* and its inverse processes, in which a ionised particle captures a free electron and emits a photon, can be referred to as *recombination*. The radiative rates for bound-free transitions can be expressed in the same way as the bound-bound transition rates using the cross section formulation, bearing in mind that photo-ionisation cross sections $\alpha_{l,u}(\lambda) = 0$ for wavelength $\lambda > \lambda_0$, where λ_0 is the cutoff wavelength associated with the binding energy. A more detailed presentation and a derivation of the corresponding formula can be found in e.g., Mihalas (1978, ch. 4-3).

Free-free processes and photon scattering

Processes in which two unbound, charged particles interchange energy but stay unbound are referred to as *free-free transitions*. These transition do not contribute to the rate equations, since they do not change the occupation numbers of any species, but may have a significant contribution to the overall radiation field. Free-free processes are well known for being the source of *Bremsstrahlung* (and its inverse process). It describes the process of a free electron being (de-)accelerated in the electromagnetic field of an ion, (emitting or) absorbing a photon without being captured by the ion. Thus Bremsstrahlung couples the radiation field to the local thermodynamic properties and vice-versa. A more detailed description of this process can be found in, e.g., Hubeny and Mihalas (2014, pp. 137 and pp. 190).

Photon scattering processes, in contrast, are almost completely determined by the radiation field as non-relativistic velocities of the *scattering centers* (i.e., atoms or molecules) are irrelevant for these processes when neglecting Doppler shifts effects. The time t and the energy E are complementary variables in view of *Heisenberg's uncertainty principle* and, consequently, the inequality $\Delta E \Delta t \leq \frac{\hbar}{2}$ holds. This very fact is the reason for the existence of photon

scattering processes and it can only rigorously be derived from *quantum field theory* allowing the scattering center to be excited into a virtual state which must not exist under other circumstances.

In non-relativistic velocity ranges and for adequately low photon energies, photon scattering processes do not alter the kinematics of the scattering center but allow the scattering particle to “absorb” photons of any energy for a tiny fraction of time $\Delta t \leq \frac{\hbar}{2\Delta E}$. Within this time frame the photon will be re-emitted into a potentially biased random direction with respect to the electron’s restframe exhibiting a nearly unaltered photon energy. It can be shown that scattering processes are anisotropic in general and, consequently, there may be a preferential direction for the scattered photons, exhibiting a distinct angular dependence often referred to as *phase function*. In most cases this angular dependence is of minor importance for the topology of the radiation field, especially if it was close to being isotropic before. Thus, it is reasonable to exploit this fact and drop this dependencies, reducing the complexity of associated calculations while introducing an error which is small compared to other sources of uncertainty, see e.g., Hubeny and Mihalas (2014, ch. 12) for more details.

Thompson scattering, on the one hand, labels the process of photons scattering on free electrons and its cross section is given by

$$\sigma_e = \frac{8\pi e^4}{3m_e^2 c^4} = 6.65 \cdot 10^{-25} \text{cm}^2. \quad (2.5.17)$$

It is independent of the photon’s wavelength in the limit of low photon energies, i.e. $\frac{hc}{\lambda} \ll mc^2$, which is an appropriate assumption for most stellar atmospheres. The given cross section is, for the reason stated above, already angle-averaged. Thompson scattering process is most prominent in hot stars (e.g O-stars), due to the high degree of ionisation and the resulting abundance of electrons.

Rayleigh scattering, on the other hand, “can be important in the atmospheres of stars of moderate temperature (spectral type G and K)”(Mihalas, 1978, p. 107), including Sun-like stars, the subjects of our interest. In this process photons scatter with electrons bound to atoms or molecules. In contrast to Thompson scattering, Rayleigh scattering shows a strong wavelength dependency owed to the involved transitions of bound electrons in atoms. The Rayleigh cross section

$$\sigma_k \propto f_{l,u} \sigma_e \left(\frac{\lambda_{l,u}}{\lambda} \right)^4 \quad (2.5.18)$$

is proportional to the Thompson scattering cross section, the classical oscillator strength $f_{l,u}$, its transition wavelength $\lambda_{l,u}$ and the photon wavelength λ , being valid for wavelengths $\lambda \gg \lambda_{l,u}$. Its exact form differs for each species k and usually has to be considered only for a few species - like hydrogen, hydrogen anions and hydrogen molecules, depending on the system's local temperatures.

2.5.2 Collisional rates

As is true for radiation, colliding particles can change the electronic configuration of their collision partners in addition to transferring momentum between one another. Earlier in section 2.5 we argued that electrons may mediate and equilibrate the local temperature by being the most frequent collision partner amongst all massive particles, if all massive particle species including electrons follow the Maxwell-Boltzmann distribution (see eq. (2.5.3)). Taking only electrons into account as collision partner we may write the upward (excitation) collisional rate as

$$C_{l,u} = n_e \int_{v_0}^{\infty} \alpha_{l,u,e}(\mathbf{v}) \mathbf{v} f(\mathbf{v}) d\mathbf{v} \equiv n_e q_{l,u}(T). \quad (2.5.19)$$

The electron collision cross section $\alpha_{l,u,e}(\mathbf{v})$, indicated by the subscript e , depends on the relative velocity \mathbf{v} between the electron and its collision partner. The threshold velocity v_0 is related to the required excitation energy for the transition at hand and $f(\mathbf{v})$ is the velocity distribution function. The cross section $\alpha_{l,u,e}$ as well as the integrated cross section $q_{l,u}(T)$ which are “required to compute [such] rates are found either experimentally or by rather complicated quantum-mechanical calculations” (Hubeny and Mihalas, 2014). Using, once again, detailed balance arguments we can correlate the collisional downward (de-excitation) rates to the collisional upward rates, since the electron velocity distribution is Maxwellian by prior assumption.

$$C_{u,l} = \frac{n_l^*}{n_u^*} C_{l,u} \quad (2.5.20)$$

In solar- and later-type stars the electron density decreases drastically and inelastic collisions with neutral hydrogen gain importance, and thus have to be taken into account.

The static atmosphere rate equation eq. (2.5.2) can then be rewritten in terms of radiative and collisional rates $R_{ii'}$ and $C_{ii'}$, respectively, using the actual population numbers n_i and the so-called LTE population numbers n_i^* introduced in equation 2.5.7 for in the TE case.

$$\begin{aligned}
& \sum_{i' < i} n_i \frac{n_{i'}^*}{n_i^*} (R_{i,i'} + C_{i',i}) + \sum_{i' > i} n_i (R_{i,i'} + C_{i,i'}) \\
& = \\
& \sum_{i' < i} n_{i'} (R_{i',i} + C_{i',i}) + \sum_{i' > i} n_{i'} \frac{n_i^*}{n_{i'}^*} (R_{i',i} + C_{ii'})
\end{aligned} \tag{2.5.21}$$

2.6 Radiative Transfer

In the previous sections we defined the specific intensity $I(t, \vec{r}, \lambda, \vec{n})$ as a central quantity for the description of the radiation field by connecting it to the photon distribution function $f_R(t, \vec{r}, \lambda, \vec{n})$ and the differential of the total energy in the system dE with eq. (2.3.3). Furthermore, we showed how the population numbers depend on the radiative and collisional up- and downward rates and linked these rates to their individual properties like quantum mechanical cross sections and profile functions. Though the absorption and the emission profile functions are not equal in general, most practical applications assume their equality by imposing the *complete redistribution* of the photons energy over the profile function.

*If the particle density is high, it is reasonable to assume that the particle distribution is (almost) isotropic and that there are numerous collisions with other excited particles before it is re-emitting a photon. This process reshuffles the excited electrons of the atoms “over the substates of the upper state before emission occurs” (Mihalas, 1978). In this limiting case, called **complete redistribution** (abbreviated CRD), the wavelength of the emitted photon will be uncorrelated with the previously absorbed photon. Under these conditions the (angle-averaged) absorption and emission profile functions $\Phi_{l,u}(\lambda) = \Psi_{u,l}(\lambda)$ are equal.* (Def. 10)

The particle density of earlier type stellar atmospheres is not very high and even decreases with increasing altitude. The approximation is, nevertheless, reasonable good in most situations, i.e., the number of collisions per excitation-time-scale required to perform this reshuffling is rather small if the system is sufficiently close to its statistical equilibrium. Deviations become apparent only once the system’s particle density is too low for an efficient reshuffling or if the system is already significantly out of local thermodynamic equilibrium for a given radiative or collisional process. A prominent example for the breakdown of this assumptions are strong resonance lines like Ly α , Ca II h&k and Mg II h&k, see, e.g., Hubeny and Lites (1995).

A direct consequence of the equality of absorption and emission profile is that the up- and downward cross sections for radiative transitions $\alpha_{l,u}(\lambda)$ and $\alpha_{u,l}(\lambda)$ no longer differ, i.e., $\alpha_{l,u}(\lambda) = \alpha_{u,l}(\lambda)$.

It is common practice to connect material properties to these cross sections and scattering coefficients, the so-called *emission* and *extinction coefficients* $\eta(t, \vec{r}, \lambda, \vec{n})$ and $\kappa(t, \vec{r}, \lambda, \vec{n})$, since they can be used to construct a general *radiative transfer equation* and are a measure of the material's opacity/transparency for a given wavelength.

The change of the specific intensity $I(t, \vec{r}, \lambda, \vec{n})$ along a path $s(\vec{r})$ can be written as

$$\frac{I(t, \vec{r}, \lambda, \vec{n})}{ds} = \eta(t, \vec{r}, \lambda, \vec{n}) - \kappa(t, \vec{r}, \lambda, \vec{n})I(t, \vec{r}, \lambda, \vec{n}). \quad (2.6.1)$$

In favour of a shorter notation the dependencies on location \vec{r} , point in time t and propagation direction \vec{n} will be suppressed from here on.

Each bound-bound emission coefficient

$$\eta_{i,i'}(\lambda) = \frac{2hc^2}{\lambda^5} \frac{g_i}{g_{i'}} \alpha_{i',i}(\lambda) n_j, \quad (2.6.2)$$

bound-bound extinction coefficient

$$\kappa_{i,i'}(\lambda) = \alpha_{i,i'}(\lambda) n_i - \alpha_{i',i}(\lambda) \frac{g_i}{g_{i'}} n_j, \quad (2.6.3)$$

bound-free emission

$$\eta_{i,i^+}(\lambda) = \frac{2hc^2}{\lambda^5} \alpha_{i,i^+}(\lambda) n_{i^+}^* \exp\left(-\frac{hc}{k_B T \lambda}\right) \quad (2.6.4)$$

and extinction coefficient

$$\kappa_{i,i^+}(\lambda) = \left[n_i - n_{i^+}^* \exp\left(-\frac{hc}{k_B T \lambda}\right) \right] \alpha_{i,i^+}(\lambda) \quad (2.6.5)$$

contributes to the total emission and extinction coefficient for each available transition.

Summing up all possible transitions $i \rightarrow i'$ with $i' > i$ we can write the transition emission and extinction coefficient as

$$\{\eta_{tr}(\lambda), \kappa_{tr}(\lambda)\} = \sum_{i < i'} \{\eta_{i,i'}(\lambda), \kappa_{i,i'}(\lambda)\} + \sum_{i, i^+} \{\eta_{i,i^+}(\lambda), \kappa_{i,i^+}(\lambda)\}. \quad (2.6.6)$$

Scattering processes are another source of opacity and their collected contributions can be

written as

$$\sigma(\lambda) = \sum_k \sigma_k(\lambda) \quad (2.6.7)$$

for each species scattering coefficient $\sigma_k(\lambda)$, e.g $\sigma_e(\lambda) = \sigma_e n_e$. Further opacity sources (like free-free transitions) are usually expressed and combined in terms of background emission and extinction coefficients $\tilde{\eta}(\lambda)$ and $\tilde{\kappa}(\lambda)$.

The *total emission coefficient* can be expressed by summing up all contributions

$$\eta(\lambda) = \eta_{tr}(\lambda) + \tilde{\eta}(\lambda), \quad (2.6.8)$$

while the *total extinction coefficient* can be represented by

$$\kappa(\lambda) = \kappa_{tr}(\lambda) + \tilde{\kappa}(\lambda) + \sigma(\lambda). \quad (2.6.9)$$

It is often more intuitive and practical to parametrise quantities to typical scales. Defining the so-called *source function*

$$S(\lambda) = \frac{\eta(\lambda)}{\kappa(\lambda)} \quad (2.6.10)$$

as the ratio between emission and extinction coefficient and introducing the *optical thickness*

$$d\tau_\lambda = -\kappa(\lambda)ds \quad (2.6.11)$$

we can reformulate the radiative transfer eq. (2.6.1) as

$$\frac{dI(\lambda)}{d\tau_\lambda} = I(\lambda) - S(\lambda). \quad (2.6.12)$$

A optical thickness τ_λ of unity is directly linked to the (statistically) characteristic distance a photon of wavelength λ can travel before being absorbed or scattered. In the same manner, the source function $S(\lambda)$ gives a quantifiable measure for the in-/decrease of radiation for a wavelength λ at that location (and direction) of the medium. If we knew the source function $S(\lambda, \tau(\vec{r}))$ for all positions $\tau(\vec{r}, \lambda, \vec{n})$ along the path we could write the *formal solution* of the radiative transfer problem as

$$I(\lambda, \tau_\lambda) = I(\lambda, \tau_\lambda = 0) \cdot \exp(-\tau_\lambda) + \int_0^{\tau_\lambda} S(\lambda, t) \cdot \exp(t - \tau_\lambda) dt. \quad (2.6.13)$$

In reality we know neither the source function nor the emission and extinction coefficients but rather have to compute them in our effort to solve the differential equation given above. However, “in NLTE transfer, the source terms are implicitly non linear because the occupation numbers of the material, and hence its opacity and emissivity, which determine the radiation field, are determined by the radiation field” (Hubeny and Mihalas, 2014). Since non-linear differential equations can not be solved directly, iterative approaches have to be used in order to obtain a solution.

Radiative transfer equations are most commonly solved computationally and, therefore, it is reasonable to adjust the nomenclature by indicating the discretisation of functions and operators. The following expressions are, nevertheless, valid for continuous and discretised quantities alike. The formal solution eq. (2.6.13) can be re-written as an operator equation

$$I_{\lambda, \vec{n}} = \Lambda_{\lambda, \vec{n}}[S_{\lambda, \vec{n}}], \quad (2.6.14)$$

where the (direction dependent) Λ -operator $\Lambda_{\lambda, \vec{n}}$ acts on the source function $S_{\lambda, \vec{n}}$ returning the specific intensity $I_{\lambda, \vec{n}}$. A similar equation can be written for the mean intensity

$$J_{\lambda} = \Lambda_{\lambda}[S_{\lambda}], \quad (2.6.15)$$

by integration over all solid angles and using the traditional Λ -operator $\Lambda_{\lambda} \equiv \oint \Lambda_{\lambda, \vec{n}} d\Omega$.

It is known that even in the case of LTE calculation, simple iteration schemes may converge very slowly or fail to converge altogether (see e.g., Hubeny and Mihalas (2014, pp. 381-383) if scattering processes are of importance for the problem. Applying different iteration schemes, e.g., using a *operator splitting method* (in this context often called approximate lambda method) as suggested by Cannon (1973), can drastically improved the rate of convergence for radiative transfer problems. Operator splitting methods reformulate the original operator by inserting a unity relation $\Lambda = \Lambda^* + (\Lambda - \Lambda^*)$, where Λ^* is a properly chosen approximate operator, and plugs these into a more beneficial iteration scheme

$$J_{\lambda}^{(\text{new})} = \Lambda_{\lambda}^*[S_{\lambda}^{(\text{new})}] + (\Lambda_{\lambda} - \Lambda_{\lambda}^*)[S_{\lambda}^{(\text{old})}]. \quad (2.6.16)$$

Given an explicit formulation for the source function $S(\lambda)$, it is possible to sort the arguments in eq. (2.6.16) such that there is a separation of new and old variables. For example, if the source

function can be expressed in terms of the mean intensity $J(\lambda)$, the Planck function $B(\lambda)$ and a *thermalisation* parameter $\epsilon(\lambda)$

$$S_\lambda = (1 - \epsilon_\lambda)J_\lambda + \epsilon_\lambda B_\lambda. \quad (2.6.17)$$

we may formulate the iteration scheme explicitly as

$$J_\lambda^{(\text{new})} = (1 - \Lambda_\lambda^*(1 - \epsilon_\lambda))^{-1} \left(J_\lambda^{\text{FS}} - \Lambda_\lambda^*[(1 - \epsilon)J_\lambda^{(\text{old})}] \right), \quad (2.6.18)$$

where $J_\lambda^{\text{FS}} = \Lambda_\lambda[S_\lambda^{(\text{old})}]$ is the result of the formal solution for the previous iteration, see e.g., Berkner (2015). Any appropriate iterative solver may then be used to compute the solution for a given problem. Wichert (2019, in prep.) has implemented a new, advanced iterative solver tailored for diagonal matrices of small bandwidth.

In analogy to the iterative procedure for the mean intensity we can apply the Λ -operator scheme to the rate eq. (2.5.21), too. Defining the *rate-operator* for upward transition $[R_{l,u}]$ and the density population operator $[n]$ we can write a radiative rate as

$$R_{l,u} = [R_{l,u}][n]. \quad (2.6.19)$$

As was stated before, we do require the number densities $n_{i,k}$ of all level i for all species k to calculate the source function and a approximation of the radiation field, which themselves depend on the radiation field through the rate equations. Hence, we need to seek for a simultaneous solution for both problems by correcting one another's solution each iteration. Writing the rate equations with the given operator definitions we can see the non-linearity of the rate equations in the number densities.

$$\begin{aligned} \sum_{i' < i} n_{i'} ([R_{i',i}][n] + C_{i',i}) + \sum_{i' > i} n_{i'} \frac{n_i^*}{n_{i'}^*} ([R_{i',i}][n] + C_{i,i'}) \\ = \\ n_i \left\langle \sum_{i' < i} \frac{n_{i'}^*}{n_i^*} ([R_{i,i'}][n] + C_{i,i'}) + \sum_{i' > i} ([R_{i,i'}][n] + C_{i,i'}) \right\rangle \end{aligned} \quad (2.6.20)$$

Further non-linearities can be found through the electron density dependence of the collisional rates and the additional need to close the system of equations (e.g., by particle and charge conservation) introducing another implicit non linearity. Once more, since there is no direct

way to solve the system of equations, we need to solve this system iteratively. More details on the iteration scheme, the explicit generation of the operators and convergence behaviour are presented in the aforementioned paper series by Hauschildt and Baron.

Let us recall the assumptions and approximations that were applied through out this section to derive a description of the radiative transfer problem and its solution. In general we assumed that

- the gas in the atmosphere may be characterised as ideal gas (see definition 2),
- the velocity distribution of all massive particles can be described by the Maxwell-Boltzmann eq. (2.5.3), i.e., each species moves in correspondence to the local kinetic temperature,

as the conditions seem to be in excellent agreement with these assumptions in most stellar atmospheres. Furthermore, since a full 3D NLTE treatment (eventually including magnetohydrodynamics) is still not feasible, a number of additional approximations need to be applied. These approximations include

- the calculation of a static steady state solution for the rate eq. (2.5.2),
- complete redistribution of energy in any radiative transition resulting in the equality of the absorption and emission profile function,
- isotropic profile functions and isotropic scattering

and reduce the complexity of the rates, rate equations, the source function and overall problem by a great margin.

2.6.1 Implementation - Phoenix/3D

The computation and analysis of the radiative properties of a 3D Sun-like stellar atmosphere under consideration of NLTE effects is the basis for the objective of this thesis.

Even today the computational costs in terms of CPU time, memory and disk storage for such tasks is extremely high and can easily become prohibitive at a certain level of detail. Thus, it is necessary to work with highly efficient and specialised software utilising high performance computing centres and their massive parallel computation powers.

Phoenix (Hauschildt and Baron, 2006) is a general-purpose state-of-the-art atmosphere code. It can calculate atmospheres and spectra of stars all across the Hertzsprung Russel-diagram including main sequence stars, giants, white dwarfs, stars with winds, T Tauri stars, novae, supernovae, brown dwarfs and extrasolar giant planets, utilising parallelisation multi-threading interfaces/libraries (e.g., MPI and SMP) and applying parallel-programming concepts like *domain-decomposition* and *vectorisation*. Phoenix has two different main modes of operation, namely Phoenix/1D and Phoenix/3D. Both modes calculate the equation of state, generate (N)LTE opacities and may solve the multi-level NLTE rate and radiative transfer equations. The solution of radiative transfer equation in both modes is calculated along characteristics, i.e., the path along a pencil ray of radiation. While Phoenix/1D can be used to solve time-dependent, special relativistic radiative transfer problems in spherical or plane-parallel geometry, Phoenix/3D is used to compute the radiation field for pre-computed 3D hydrodynamic models given in Cartesian, cylindrical or spherical coordinate systems. In addition, Phoenix/1D provides a temperature correction procedure such that the total energy of the system is conserved by adapting the thermal structure of the model, iteratively. This temperature correction serves as one of a few convergence indicator. Since Phoenix/3D does not evolve the hydrodynamic structure, there is neither a temperature correction implemented currently, nor would it be a useful convergence indicator in the above sense. The change in the electron density, the departure coefficients, the population numbers and the synthetic spectra can be used as proxies for convergence of a model in both modes. An in-depth description of the Phoenix/1D features can be found in Hauschildt (1993) paper on 1D multi-level NLTE while the series of papers Hauschildt and Baron (2006) to Hauschildt and Baron (2014) describe the theory and application of Phoenix/3D in detail.

Without going into too much detail, we could outline the work-flow of a typical Phoenix/3D run as follows:

1. set up run configuration, i.e. wavelength grid, NLTE species, number of solid angles, etcetera
2. read and load the model structure
3. solve the equation of state for each species and calculate their population numbers
4. for all wavelength points in the pre-set grid
 - (a) calculate the monochromatic opacity and emissivity coefficients

- (b) solve the radiative transfer equation
- (c) calculate the (new) radiative rates
- 5. calculate the (new) collisional rates
- 6. build the rate matrix, solve the rate equations and update the population numbers
- 7. repeat steps 4. to 6. until the model is converged to a satisfactory degree

The equation of state solver currently used in step 3. is ACES-EOS (Astrophysical Chemical Equilibrium Solver-Equations of State). It is based on the VCS method by Smith and Missen (1982) and calculates an ideal gas stoichiometric equilibrium in steady state. Current work has been and is being done to implement the new EOS-solver SESAM, see, e.g., (Meyer, 2017). The calculations in steps 4. (a)-(c) prerequisite the knowledge of many quantum mechanical cross sections. Phoenix uses atomic and molecular line data from a number of different sources to compute (N)LTE opacities and rate coefficients.

The CPU-time, disk and main memory required for a single iteration of Phoenix/3D on a hydrodynamic model of moderate spatial resolution treating NLTE species may still exceed the capabilities of today's high performance computing facilities. Thus, restart files are of particular importance for the feasibility of calculating and converging 3D NLTE radiative transfer models. Phoenix/3D stores i.a. the population numbers, the departure coefficients, the chemical composition and thermodynamic information after each successful iteration, but does neither store the specific intensity nor any of its moments in normal operation. The mean intensities, the flux vectors and source function values - the angle averaged radiation field quantities - can be stored on demand but generate enormous amounts of data. Using these data the specific intensity for all solid angles can be recalculated by performing a formal solution.

The formal solution in Phoenix/3D uses a *full characteristic* approach, following a ray through the structure in a given direction $\vec{n}(\theta, \phi)$. Periodic boundary conditions in the horizontal x-y plane are usually imposed for “box of a star” models and rays trespassing the boundaries are being wrapped around and followed along, correspondingly.

The rate of convergence and the accuracy of the solution depend on many different factors, e.g. the spacial resolution, thermodynamic properties and spatial gradients of the hydrodynamic structure, the number and choice of wavelength points used to sample the wavelength integrals, the number of gas species (and levels of the former) treated in NLTE and the solid angle resolution.

CHAPTER 3

INSPECTION AND ANALYSIS OF DATA

Having introduced the basic concepts of magnetohydrodynamics and radiative transfer we are about to inspect and analyse the data for a set of given structures and models. We saw that Phoenix/3D requires a hydrodynamic structure as input based on which the radiation field is then iteratively calculated. Thus, it comes naturally to start with a detailed characterisation and depiction of these structures, followed by a discussion of the radiation fields' properties and the resulting spectra. In addition we will compare the radiation field of the different models with one another and with a 1D simulation.

3.1 Hydrodynamic structure

At the beginning of the project, five magnetohydrodynamic models resembling a quiet Sun's atmosphere were acquired via private communication with Wedemeyer-Böhm (2015, 2017).

The models' initial magnetic field configuration featured homogeneous, vertically directed field lines with a predefined magnetic field strength of 10 to 200 G depending on the model. Each model was simulated for many time-steps guaranteeing relaxation as well as a properly developed magnetic field configuration and atmosphere structure. In-depth information as well as details on the generation of similar magnetohydrodynamic simulations and their time-dependence can be found, for example, in Leenaarts and Wedemeyer-Böhm (2006) and Wedemeyer-Böhm et al. (2012).

The inspection of these different models revealed interesting and non negligible differences in the thermodynamic properties and resulted in shortlisting the 50 G and the 200 G structure, since they showed distinctly different behaviours. Trial calculations, however, uncovered huge differences in the rate of convergence between the 50 G and the 200 G structure favouring the

latter. While a fast rate of convergence is always desirable, it is indispensable in the light of the exceedingly high demand on computational resources and time for the calculation for each iteration of the 3D NLTE radiation transfer problem. Consequently, the 200 G structure, referenced as structure 1 for here on, is the most sensible choice as input structure for Phoenix/3D. In the following section this structures and its properties will be presented.

Considering the immense amount of space needed to solve and store 3D NLTE radiative transfer simulations, it is both, expedient to include only a few selected atomic/molecular species in NLTE and indispensable to scale back the resolution of the magnetohydrodynamic data. Structures of a lower resolution were generated by binning the original structural information in the directions x and y onto a more coarse grid using linear interpolation. The vertical resolution along the z -direction remained unaltered for all model structures.

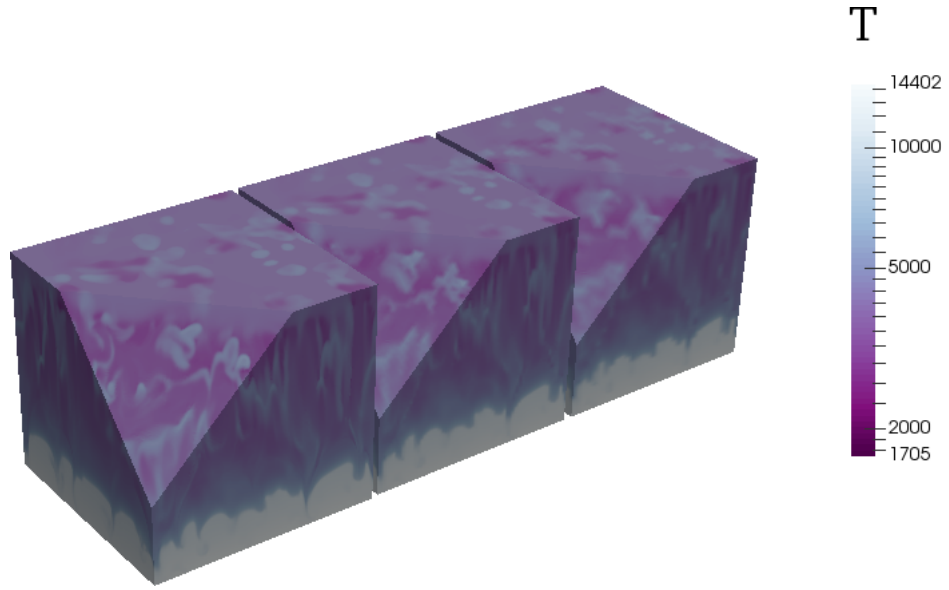
Even after this significant reduction of the structures resolution it is still infeasible to treat more than just a few selected atomic/molecular species in NLTE when calculating the 3D radiative transfer and rate equations.

3.1.1 Structure 1

In this section the general properties of structure 1, the available snapshot from a model with an initially vertical magnetic field strength of 200 G, will be displayed and discussed. The structure's gas temperature displayed in fig. 3.1 shows a color-coded 3D view presenting four partial surfaces, two vertical model-box boundaries, the horizontal top-layer boundary and a 45° slice through the upper 2/3 of the structure. It features the original resolution $nx = 286$, $ny = 286$, $nz = 233$ (left), and two reduced resolutions $nx = 65$, $ny = 65$, $nz = 233$ (middle) and $nx = 33$, $ny = 33$, $nz = 233$ (right) with a geometric extent of 7800 km in x - and y -direction with constant step-width and a total depth of about 3100 km in the vertical z -direction.

First and foremost this color-coded 3D view provides a representative picture of the structure's thermodynamic nature and gives a first impression of the loss of information induced by the reduction of resolution, which results in a diminished temperature contrast. The general shape of turbulent features does not change significantly, however. The temperature, ranging from about 1700 K to 14400 K, shows the expected variations both along the vertical and the horizontal direction, exhibiting a trend of decreasing temperature from its lower layers towards the higher altitudes.

Figure 3.1



Gas temperature T [K] of structure 1 in a 3D Color-coded view shown for the original resolution $nx = 286$, $ny = 286$, $nz = 233$ (left) and two reduced resolutions $nx = 65$, $ny = 65$, $nz = 233$ (middle) and $nx = 33$, $ny = 33$, $nz = 233$ (right).

Furthermore, fig. 3.1 highlights the existence of many, mostly small scaled, comparably hot, turbulent structures in cooler environments. These features are caused by a combination of hydrodynamic instabilities like shocks (see, e.g., Leenaarts and Wedemeyer-Böhm, 2006), the influence of the magnetic field and convection phenomena and are characteristic for (magneto-) hydrodynamic structures.

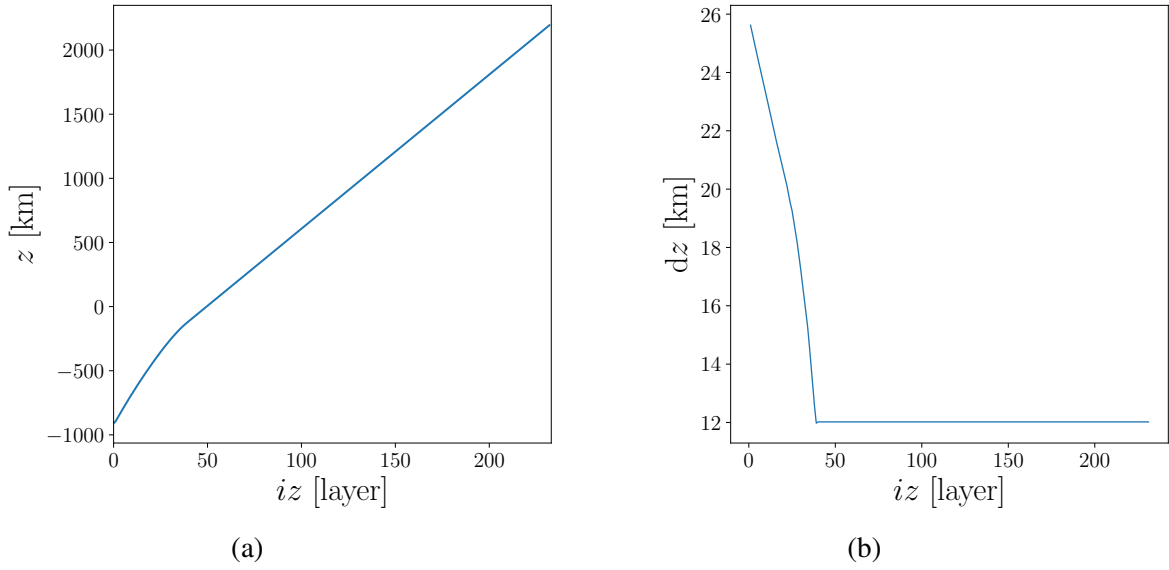
The distances between the vertical layers of the structure are not constant, however, and need to be described by a mapping $z(iz)$, where iz corresponds to the layer's index, referred to as *z-map*.

Both the *z-map* $z(iz)$ and its gradient $dz(iz)/diz$ are illustrated in figs. 3.2a and 3.2b. Inspection reveals that the *z-map* is monotonically increasing and features a gradually decreasing slope within the layers $iz = 0$ to 43 and a near linear slope of about $12\text{km}/iz$ throughout the rest of the structure's layers.

Note that the 3D view in fig. 3.1 does not account for these variation in the z -coordinate and instead exhibits a constant step-width in z -direction as well. This distorted representation is, however, very helpful as it over-emphasises layers with small *z-map* gradients $dz(iz)/diz$ and, thus, regions with a higher numeric resolution.

Moreover, the structure exhibits a temperature gradient of up to 120 [K/km] , assuming the

Figure 3.2



Z-map $z(iz)$ (a) and its gradient $\frac{dz(iz)}{diz}$ (b) per layer iz .

structure's thermodynamic quantities to be differentiable. The temperature variation is less pronounced in the lower and on average hotter layers and increases notably in the upper layers. The particle density and the gas pressure (on average) decreases with height and, therefore, collisional energy redistribution is hampered leading to bigger local temperature deviations.

It is convenient to introduce labels for different regions in the structure, relating them to well known, and phenomenologically defined, atmospheric zones.

The *convection zone* is, by definition, the region in a star which is unstable to convection. Whether material is stable against convection or not depends on its local thermodynamic properties and can, in first approximation, be determined by the well known *Schwarzschild criterion*.

The beginning of photosphere may be defined by an optical depth of unity (or $2/3$ depending on the author). The optical depth, however, does not only explicitly depend on the (observation) wavelength but is also very sensitive to the actual distribution of matter in the structure, thus, prohibiting a unique definition of the corresponding altitude. Additionally, the typical extension of a Sun-like photosphere is set to about 500 km. The end of the convection zone and the beginning of the photosphere happen to coincide rather well in Sun-like atmospheres. The (lower) chromosphere is located above photosphere and shows a comparatively low particle

density and gas pressure. It is, therefore, especially susceptible to shocks and presents itself as a turbulent region featuring networks and patches of matter exhibiting vastly differing properties, like temperature, next to one another.

The bottom of the structure from -900 to ~ 0 km exhibits comparatively large temperatures, pressures and densities and will be referred to as the upper most part of the convection zone. The layers in between ~ 0 and ~ 500 km may accordingly be called photosphere, and the layers from ~ 500 to 2200 km can be associated with the (lower) chromosphere.

Please note that the region's borders defined above must not be mistaken for exact boundaries but primarily serve to label the corresponding altitude ranges and may, in addition, be understood as approximate transitional altitudes.

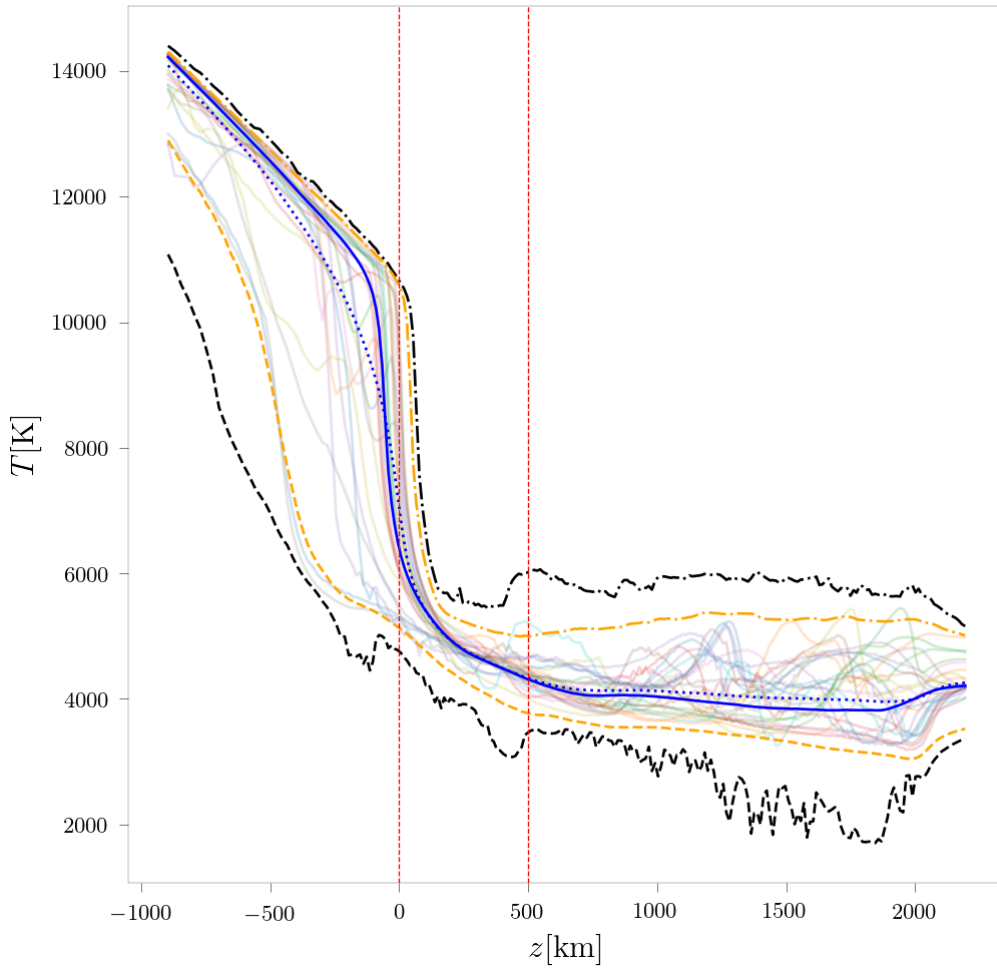
More information can yet be gained by taking a closer look at the structure's properties column by column. These vertical columns will be referred to as a quantity's *profiles* in the following. Figure 3.3 presents the maxima, minima, mean, median as well as the fifth- and ninety-fifth percentiles at altitude $z(iz)$ of the temperature T and a small set of temperature profiles, where iz refers to the number of the corresponding horizontal layer. The red dashed vertical lines show the previously defined borders from the convection zone to the photosphere and from the photosphere to the chromosphere. The number of columns along the z -axis, $n_x \cdot n_y = 81786$ in the structure at original resolution, is enormous, thus, it is sensible to visualise only a few representative profiles.

Both, the set of actual profiles and percentile lines indicate that the maxima and minima do not correspond to a few extreme columns generating most of the maxima/minima but rather to a large number thereof. In fact over 53% of all temperature curves along the z -columns contribute to the fifth- and ninety-fifth percentiles in at least one layer of the atmosphere.

The averaged temperature quantities exhibit a notable temperature decrease with rising altitude from the convection zone throughout the photosphere and reach a rather stable plateau in the chromospheric layers. Also, it is remarkable that the maximum to minimum variation reaches a minimum in the photosphere.

Figures 3.4a and 3.4b depict the associated averages, extrema, percentiles and the same set of column profiles for the gas pressure P_{gas} and, respectively, the particle density ρ . Both show the characteristic abatement with rising altitude, except for a small plateau in the density's mean and median around the beginning of the photosphere. Moreover, only about 24% and 28% of

Figure 3.3



Gas temperature T vs. altitude z from the outermost convection zone to upper chromosphere. The maxima (black dash-dots), minima (black dashes), mean (blue dots), median (blue solid), fifth- and ninety-fifth percentiles (orange dash-dots and orange dashes) calculated at each altitude z (iz) of layer iz as well as a small set (pallid colors, thin solid) of its columns along the z -axis.

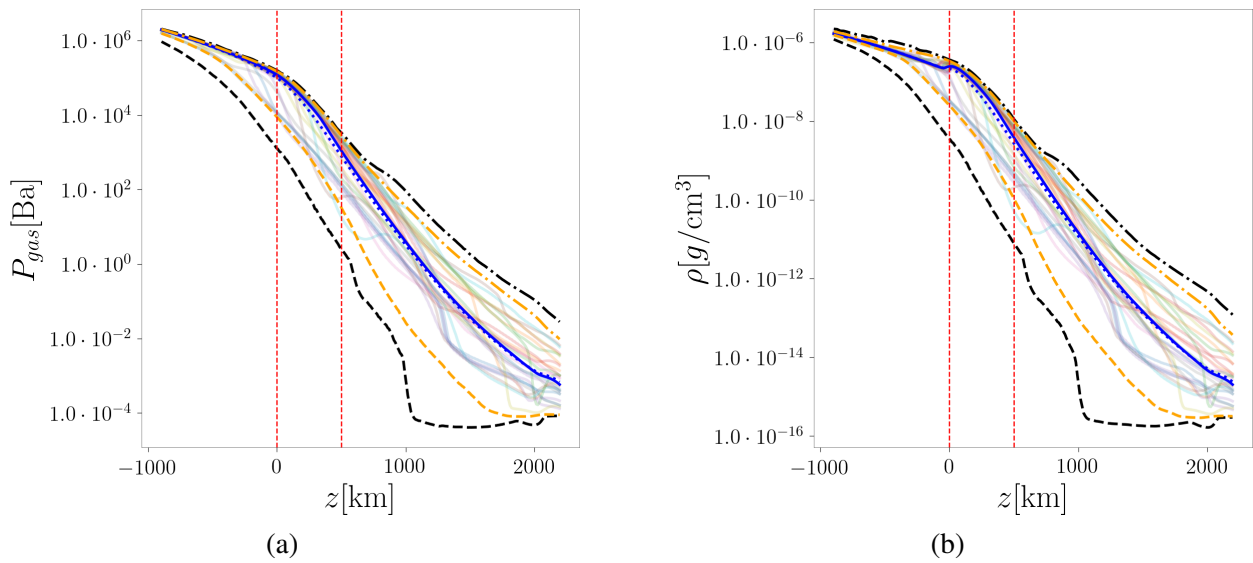
The vertical lines (red dashes) indicate the approximate transition height from convection zone to photosphere and from photosphere to chromosphere.

all pressure and density profiles, respectively, contribute to the fifth- and ninety-fifth percentiles at least once.

Due to the existence of the previously mentioned, small scale structures throughout most of the atmosphere it is certainly worth to have a look at the structure's temperature distribution, layer by layer.

Such a temperature distribution for all horizontal layers is presented as histogram-data with a bin width of 100 K in fig. 3.5. The lower layers display a clear population maximum at high temperatures. The temperatures associated with this population maximum slowly drop

Figure 3.4

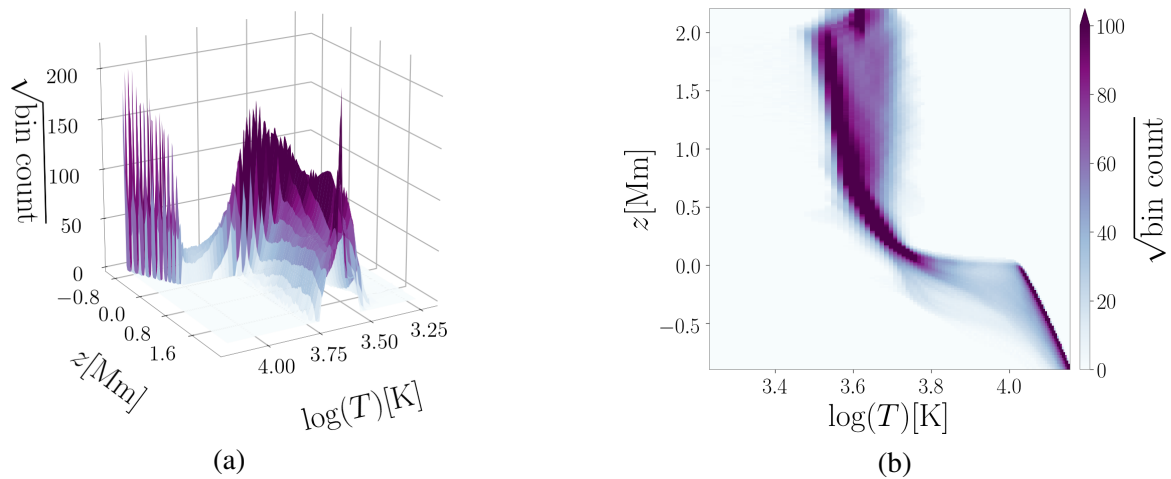


Gas pressure P_{gas} (a) and particle density ρ (b) vs. altitude z from the outermost convection zone to upper chromosphere.

The maxima (black dash-dots), minima (black dashes), mean (blue dots), median (blue solid), fifth- and ninety-fifth percentiles (orange dash-dots and orange dashes) calculated at each altitude $z(iz)$ of layer iz as well as a small set (pallid colors, thin solid) of its columns along the z -axis.

The vertical lines (red dashes) indicate the approximate transition height from convection zone to photosphere and from photosphere to chromosphere.

Figure 3.5



Color-coded 3D (a) and 2D (b) temperature histogram-data.

Histogram for each layer iz showing the square-root bin counts of the gas temperature $\log(T)$ [K] in bins of 100 K width.

to about 10000 K ($\log(T) = 4.0$) throughout the convection zone. Note that the entropy at the lowermost layer of the structure is pre-defined by model construction, which results in a very stable temperature in the structure's convection zone. Closing in on the photosphere a significant population shift is visible caused by the transition of the energy transport mode from convection to radiation, favouring a temperature of about 6000 K ($\log(T) = 3.75$).

Exhibiting a clear bin count maximum at the lower end of the temperature distribution the temperature slowly drops with rising altitude and fans out exceedingly in the chromosphere. A massive depopulation of the lower temperatures can be found in the uppermost layers of the chromosphere, leading to a bin count peak at temperatures of about 6000 K ($\log(T) = 3.75$). This suggests a massive deposition of energy in the respective layers at about 2000 km height, which is likely to be directly related to a shock process. Unfortunately, the lack of further information on higher atmospheric layers does not permit a justifiable interpretation of this feature.

The coexistence of hot and cold material side by side inevitably leads to an increase of turbulent behaviour in the corresponding layers and offers opportunities for various non-equilibrium effects, including departures from LTE occupation numbers.

These observations are of major importance for the interpretation and significance of averaging procedures and their application to the thermodynamic quantities. Neither mean nor median can be expected to be representative for the structures actual behaviour for big parts of the overall structure, especially so in the chromosphere. Independent of the layer's altitude they do, nevertheless, yield meaningful information on the quantities' order of magnitude and may be useful for the detection of trends, especially when paired with some measure of deviation.

3.2 Radiative transfer models

A detailed 3D treatment of the radiation transfer problem in NLTE is, as has been stated before, computationally extraordinary expensive. Therefore, it is still infeasible to include large numbers of atomic species in NLTE, let alone molecular species. The latter may, nevertheless, be considered utilising a super-level approach as has been shown by, e.g., Berkner (2015); Schweitzer et al. (2000). Still, a deliberate selection and reduction of the number of species treated in NLTE is a necessity for 3D radiative transfer simulations.

Hydrogen (H) is the most abundant atomic species in most stellar objects and consequently plays a crucial role in their atmospheres' radiation and energy transfer. Many (magneto-) hy-

hydrodynamic model theories as well as codes, including CO⁵BOLD, rely on this very fact and utilizing the one-fluid approximation to produce reasonable detailed models. Hence, it is unsurprising that each of the models discussed below calculate the NLTE number densities and level populations of hydrogen. Following the chain of nucleosynthesis reactions as well as noting the importance of certain lines in observed solar spectra, Helium (He) and a combination of carbon (C), nitrogen (N), oxygen (O), magnesium (Mg), calcium (Ca) and iron (Fe) lines were also treated in NLTE, if feasible.

Phoenix/3D calculates the occupation numbers and rate equations for all selected species in NLTE given a predefined number of ionisation stages and a maximum number of eligible NLTE levels in each ionisation stage. Transitions excluded by this selection were not neglected but instead treated in LTE. Being able to limit these numbers is especially helpful when dealing with species which exhibit enormous numbers of line transitions and ionisation stages, like iron. Additionally, all models were supplied with a huge number of LTE atomic and molecular line data, as described further above.

The resolution of the hydrodynamic structures is yet another important factor when judging practicability of such radiative transfer simulations. Consequently, simulation were performed for structure 1 with two different resolutions considering various species in NLTE. Table 3.1 lists the models' properties corresponding to each structure for easy referencing. Owing to time constraints and computational cost, the calculation of models featuring systematic variations, i.e., of their resolutions given a fixed species set-up, were disregarded in favour of calculations and discussions of models with a different NLTE species.

Table 3.1

Name	Structure	Resolution (nx, ny, nz)	NLTE species
model 1	structure 1	65, 65, 233	H I, He I-II, (C , N, O, Mg, Ca) I-III
model 2	structure 1	33, 33, 233	H I, He I-II, Fe I-III

List of general model properties

showing the corresponding structure, resolution and species treated in NLTE. The species letters are followed by their considered ionisation stages. Bracketed species share the same number of ionisation stages.

Phoenix/3D solves the radiative transfer problem for a given hydrodynamic structure and approach convergence, stepwise, by iteratively adapting the population numbers of all species considered in NLTE as described above in section 2.6.1.

However, the rate of convergence for a given structures is unknown a priori and difficult to

judge in general. Even in the best case scenario, in which all species present a fast, ever decreasing change of population numbers, it can be difficult to define meaningful convergence criteria, since it is not the amplitude but the rate of change which is most important in the determination of convergence of a model.

The non-linear coupling between the species has it that such simple behaviour may not be seen at all. It may, just as well, be exhibited by only a few species' levels while the rate of change in other species' levels may not be (as) rapidly decreasing, show strong fluctuations or not be decreasing at all. Furthermore, the observed non-locality of the radiation field couples voxels of disjoint regions featuring potentially vastly different physical properties.

Therefore, it can be interesting to look at the general and individual development of the model's convergence with regards to its population numbers, but this will not be demonstrated in this thesis.

At the same time one should always be aware of the fact that the contribution and importance of any given voxel's population numbers to the model's overall radiation field may vary heavily. Actually, the rate of change in the radiative flux or the specific intensity may prove to be a more useful and result-orientated proxy of NLTE convergence.

Phoenix/3D generates a restart-file after every finished iteration of the radiative transfer equation. This is not only a fail-safe feature protecting the results from possible system instabilities, but is also a necessity as the number of required iterations is too large to be calculated in one run and since the computational cost, in terms of CPU-time, per iteration can be huge.

On top of general model- and set-up-information each restart-file contains the list of all species treated in NLTE as well as their LTE and NLTE population numbers n_i^* and n_i for all voxels. It does, however, not contain any wavelength dependent quantities such as any moment of the specific intensity, the opacities or the approximate lambda-operator, mainly due to their massive demands on additional disk space. Instead, these will be recalculated from scratch each iteration.

In addition, the information about the radiative flux $\vec{F}(\lambda)$, the source function $S(\lambda)$, the mean intensity $J(\lambda)$ and the values of the Planck function B for all voxels in the model may be stored on demand, e.g., if a synthetic spectrum is to be calculated for a finished model. This further permits a simple creation of the models accompanying LTE spectrum making direct comparisons straightforward. The previously mentioned spectra are derived from the vertical directed radiative flux F_z for the outermost calculated layer (referenced as surface below). They measure

the radiative energy escaping from the model atmosphere and can be understood as an approximation of an observable flux.

Phoenix/3D calculates the radiative transfer equations for a huge number of wavelength points, approximating the wavelength integral by a predefined wavelength grid. It consists of a user-defined (usually non-equidistant) wavelength point grid which is being refined by sets of additional wavelength points about each transitions wavelength corresponding to the respective atomic species considered in NLTE. These additional wavelength points can be, and have been, included in the corresponding LTE models as well.

In the following sections each model will be inspected individually, disclosing the models computational set-up, inspecting its spectrum in the wavelength ranges 700 to 3500 Å, 3500 to 7000 Å and 7000 to 10^5 Å, referred to as ultra-violet, visible and infrared, and discussing a number of selected line features. For the sake of comparability and a better graphical representation, the flux figures displayed below do not show the data in their original wavelength resolution. Instead, the data were post-processed by interpolating them to a wavelength-grid of constant step-width and smoothing them to a given resolution with a Gaussian function. On the one hand, the post-processing resolution for the ultra-violet, the visible and the infrared wavelength range demonstrations were chosen to be 0.1Å, 0.1Å and 10Å, respectively, showing most important overview properties while not overburdening the figures with too many details. On the other hand, selected line profiles are displayed with a post-processing resolution of 0.01Å, guaranteeing a adequate sampling rate for all features in the discussion.

3.2.1 Model 1

Model 1 is based on structure 1 that has been discussed above. It was mentioned earlier that the original resolution of the structure is way too high to be treated in NLTE within reasonable amounts of time with Phoenix/3D. Therefore its resolution was decreased by a layer-wise linear interpolation keeping geometric extents of the original structure. The resulting input structure has a resolution of 65 by 65 by 233 voxel, the latter being the number of horizontal layers along the z -direction. A visual inspection of the structures readily reveals an expected decrease in sharpness and a minor reduction of the overall temperature contrast as has been shown in fig. 3.1.

Starting with a wavelength of 50 Å, the wavelength set-up reaches up to $1 \cdot 10^7$ Å in non-

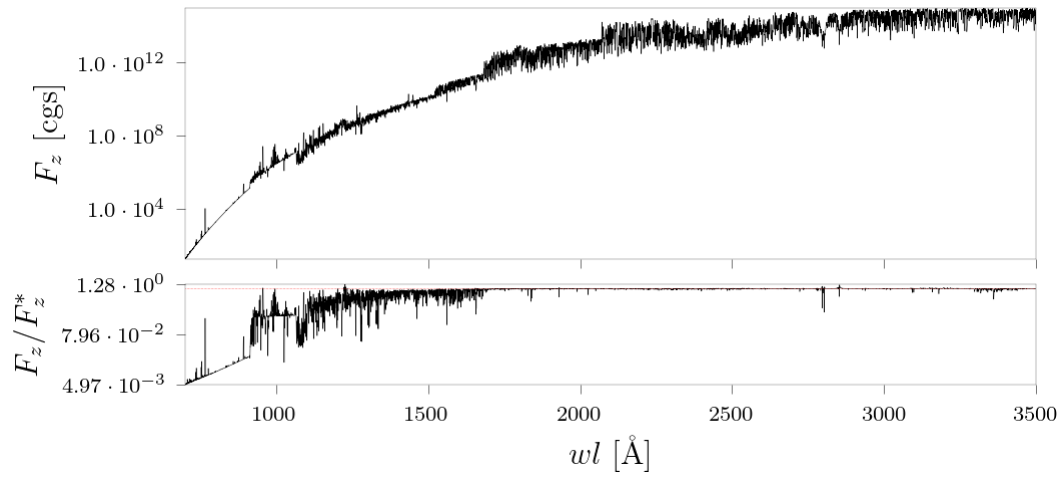
equidistant steps. The model includes hydrogen, helium, carbon, nitrogen, oxygen, magnesium and calcium with up to three considered ionisation stages in NLTE. Therefore, a total number of 2178 atomic levels, 23076 line transitions and 41540 coupled lines were considered in NLTE in addition to the remaining LTE lines.

The vertical directed flux $F_z(\lambda)$ is, as stated above, one of the generic output information received from the radiative transfer simulations with Phoenix/3D. By averaging, i.e., usually applying the geometric mean, horizontally over this quantities outermost voxels in the model, synthetic spectra can be inferred. It is useful to start describing the features of these spectra by looking at large wavelength ranges before going into detail by looking at specific, characteristic lines. Figures 3.6a to 3.6c present the mean of the vertical directed flux F_z (top) as well as their relative deviation from their respective LTE counterparts $F_z(\lambda)/F_z^*(\lambda)$ (bottom, $F_z^*(\lambda)$ is the LTE flux) in the ultra-violet, visible and infrared wavelength range, respectively. The general shape of the spectra is in line with the expectations for a Sun-like atmosphere, featuring the highest monochromatic flux values $F_z(\lambda)$ in the visible and near ultra-violet wavelength range and peaking at around 4030 Å for this model. Moreover, some characteristic absorption features like H α (centred at 6564.6 Å), the singly ionised magnesium doublet Mg II H and K (centred at 2803.5 Å and 2796.3 Å) and the singly ionised calcium doublet Ca II H and K (centred at 3969.6 Å and 3934.7 Å) can already be spotted on this scale. Furthermore, fig. 3.6a exhibits two flux edges around 1690 Å (close to the Mg I ionisation edge 1621 Å) and 2090 Å (close to the Ca I ionisation edge 2028 Å), changing the flux by more than a half magnitude over a range of only a few Angstroms.

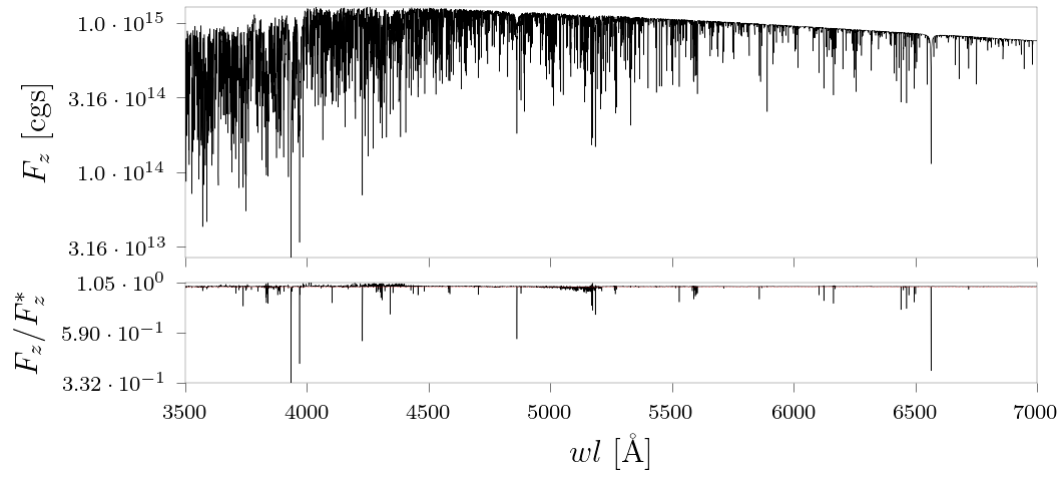
A glance at the NLTE to LTE flux ratio in the lower panels of figs. 3.6a to 3.6c reveals many minor and a handful major differences between their resulting averaged fluxes. In both, the visible and the infrared wavelength ranges, the NLTE effects on the flux seem to be confined to the immediate proximity around their transition wavelength. The regions further away from these transitions, that may be regarded as “continuum”, neither appear to be shifted nor distorted to a significant margin. Yet the ultra-violet range displays a non-negligible, systematic reduction of flux towards higher energies as opposed to its complementary LTE flux closing in to the 700Å mark.

However, iron, a species known to be of major importance in the high energy ultra-violet wavelength range, has not been considered in NLTE in this model. Therefore, caution should be

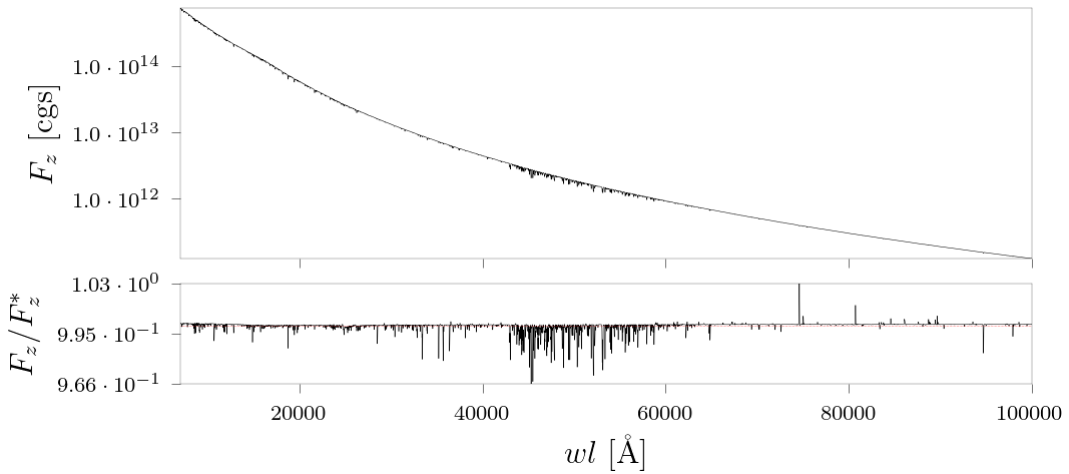
Figure 3.6



(a)



(b)



(c)

Surface flux F_z vs. wavelength λ (top) and NLTE to LTE surface flux ratio F_z/F_z^* vs. wavelength λ (bottom)

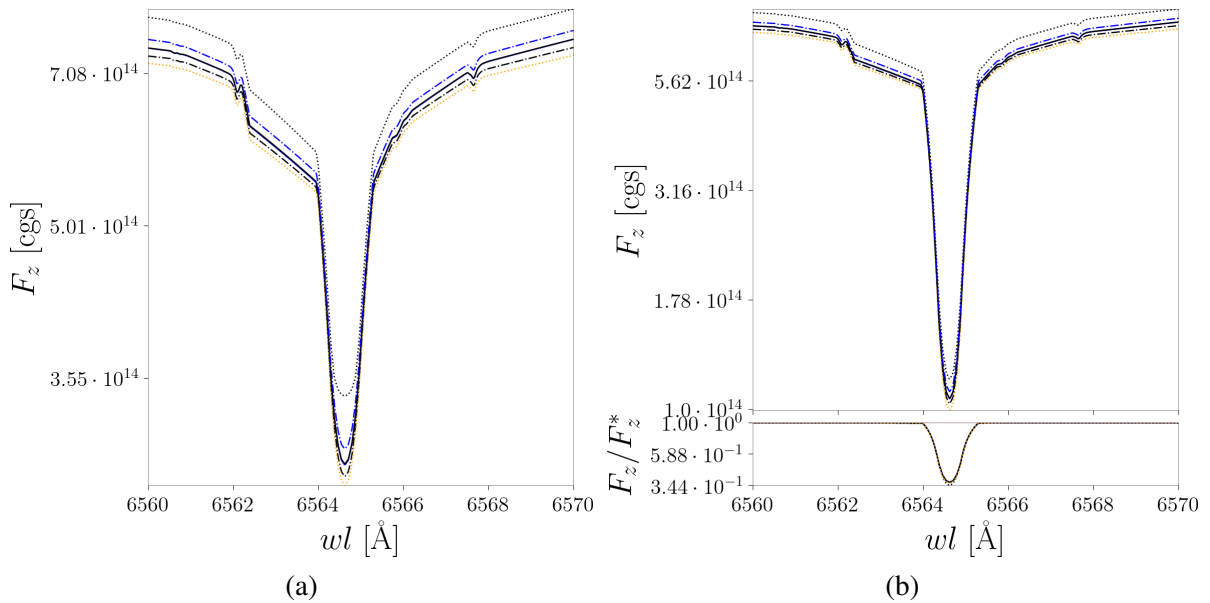
in the ultra-violet (a), visible (b) and infrared (c) wavelength range for model 1.

The red dotted line in the bottom panel is a visual guideline representing unity.

exercised with regards to the latter result. A comparison with model 2 below, treating iron and two of its ionisation stages in NLTE, will give a better basis of assessment for this problem. It is interesting to note that the lines $H\alpha$ (centred at 6564.6 \AA), the Ca II H and K doublet (centred at 3969.6 \AA and 3932.8 \AA) and the Mg II H and K doublet (centred at 2803.5 \AA and 2796.3 \AA) and $Ly\alpha$ (centred at 1215.6 \AA), commonly discussed in and considered for structural atmosphere analyses (see, e.g., Staath and Lemaire, 1995), show relatively strong deviations from their LTE values in terms of central line depth. Therefore, it is worthwhile to investigate a few of the previously mentioned lines closely in search for possible explanations for the discrepancies between LTE and NLTE results.

The differentiation of line profiles from the background continuum can be difficult, especially so when dealing with lines that exhibit wide profile wings, such as alkali and alkaline earth metals including Mg and Ca. The centre of lines, however, is always well defined and well known by definition and, hence, will be prioritised in the following presentation.

Figure 3.7

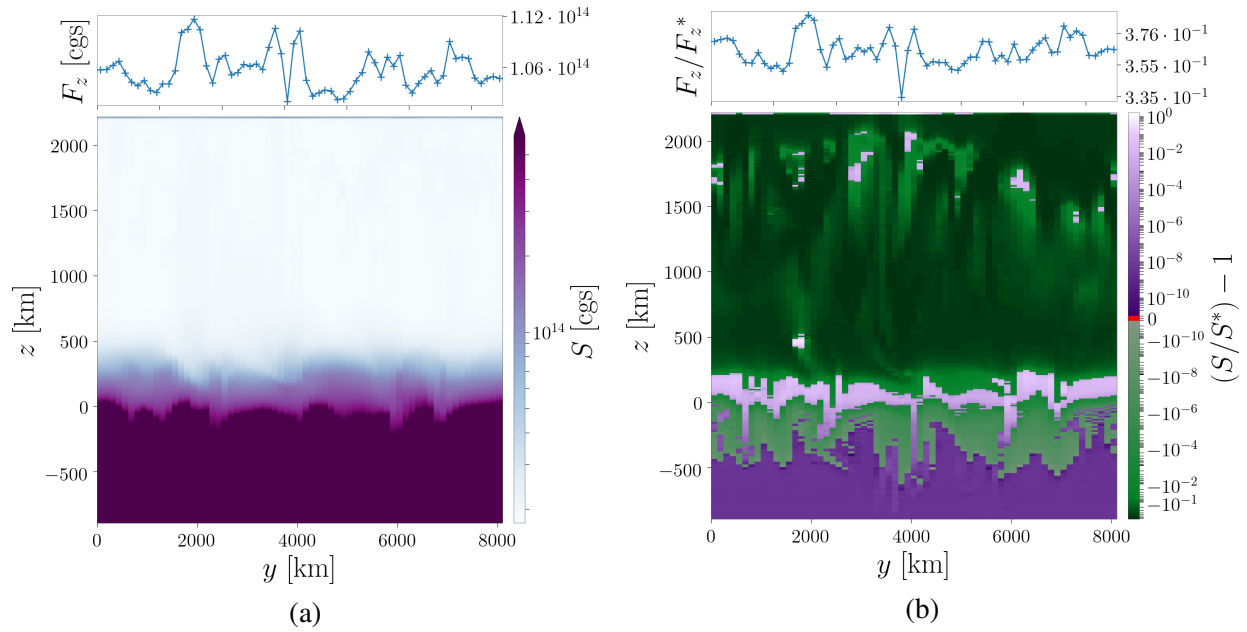


The vertical directed flux F_z^* in LTE (a), vertical directed flux F_z in NLTE (b, top) and the NLTE to LTE ratios F_z/F_z^* (b, bottom) around the line centre of $H\alpha$ for model 1.

Each figure depicts the maximum (black dotted line), minimum (orange dotted line), mean (solid orange line), median (solid blue line), ninety-fifth percentile (blue dashed and dotted line) and fifth percentile (black dashed and dotted line) computed for the outermost layer of the model atmosphere.

Each figure presents the maximum, minimum, mean, median values as well as the ninety-fifth and fifth percentiles of the vertical directed flux F_z^* in LTE, the vertical directed flux F_z in NLTE

Figure 3.8



The vertical directed flux F_z vs. latitude y in NLTE at the surface (a, top), a color-map of the source function S (a, bottom), the NLTE to LTE vertical directed flux ratios F_z/F_z^* vs. latitude y at the surface (b, top) as well as a color-map of the reduced NLTE to LTE source function ratio $(S/S^*) - 1$ in the line centre of $H\alpha$ for an arbitrary vertical slice through model 1.

and the quantities ratios F_z/F_z^* calculated for the outermost layer of the atmosphere model.

$H\alpha$ is the least energetic transition featured in the detailed description and exhibits small flux variations on the surface as can readily be found in figs. 3.7a and 3.7b. Its minimum to maximum ratio in the line center amounts to about the 12%. The percentiles indicate that most surfaces voxels' flux variations are indeed even smaller and much closer to the mean and median value. Also mean and median values are close to being inseparable and all layer averaged quantities profile shapes present near identical slopes.

The NLTE to LTE ratio F_z/F_z^* shows a simple but rather interesting behaviour. All these layer averaged quantities experience a basically uniform and strong reduction of flux. The ratio decreases steadily towards the line centre, which displays a relative flux reduction of 65% with respect to its LTE value. A closer inspection of the atmosphere's properties in deeper layers is inevitable for a thorough interpretation of this result. The source function, being the ratio of the total emissivity to the total extinction, may be used here to demonstrates the impact of NLTE effects on the surface flux. Hence, figs. 3.8a and 3.8b present color-maps of the source function S in NLTE and the reduced NLTE to LTE ratio $(S/S^*) - 1$ for the arbitrary vertical

slice $ix = 40$ through the model atmosphere, as well as the vertical directed flux F_z in NLTE and its NLTE to LTE ratio F_z/F_z^* at the surface of this slice. The NLTE source function S presents itself matching the apparent uniformity of the surface layer flux quantities through out the chromospheric layers, while only varying perceivable in the photosphere and below. The source function in the chromosphere is not only most uniform but also its value is small in comparison to the photosphere and below.

This is, in its own right, not surprising since the source function is sensitive to the particle density, which decreases with rising altitude. A look on the NLTE to LTE source function ratio, though, reveals that the LTE source function S^* in the chromosphere is anything but uniform and that NLTE effects lead to a significant reduction of the source function through out (most) of the chromosphere. Moreover, a few bright (pink to white) patches, associated with an actual increase in the source function, can be found in the shifted source function ratio and seem to be correlated rather well with the LTE to NLTE flux ratio, especially when its altitude dependence via the particle density is taken into account.

In sum this is an excellent example for the non-locality aspect of the NLTE radiative transfer leading to a nearly complete loss of contrast in the chromospheric layers' source function. On the contrary, the photosphere and the upper convection zone show notable fluctuations. The source function ratio in the convection zone present, expectedly, only marginal deviations from the LTE values and shows a slight increase in the photosphere.

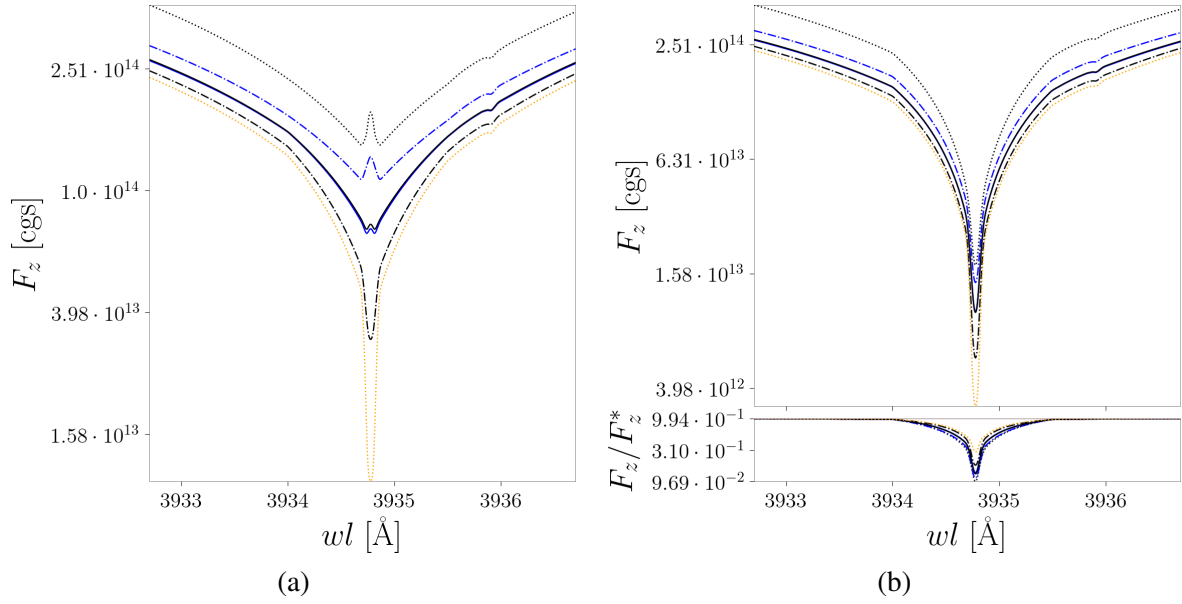
The vertical directed flux at the surface of this slice represents the shape of the source function at the lower photospheric altitudes about 0 km reasonable well, but by no means perfectly. This is what one would expect due to the cumulative nature of the flux being the first-order moment of the angle dependent specific intensity.

It is, nevertheless, widely accepted and most commonly applied that $H\alpha$ can be used to probe the structure of the photosphere. The results shown above are in good agreement with this statement, especially under consideration of NLTE effects causing the source function to be reduced and levelled in the chromospheric layers.

The Ca II H and K doublet lines are primarily formed in the upper photosphere and above and are, therefore, often regarded as a good indicator for chromospheric activity. The Ca II K line, shown in figs. 3.9a and 3.9b, presents considerable differences between the near line centre profile shapes in LTE and NLTE.

In stark contrast to the uniform reduction of the vertical directed surface flux F_z with respect to

Figure 3.9



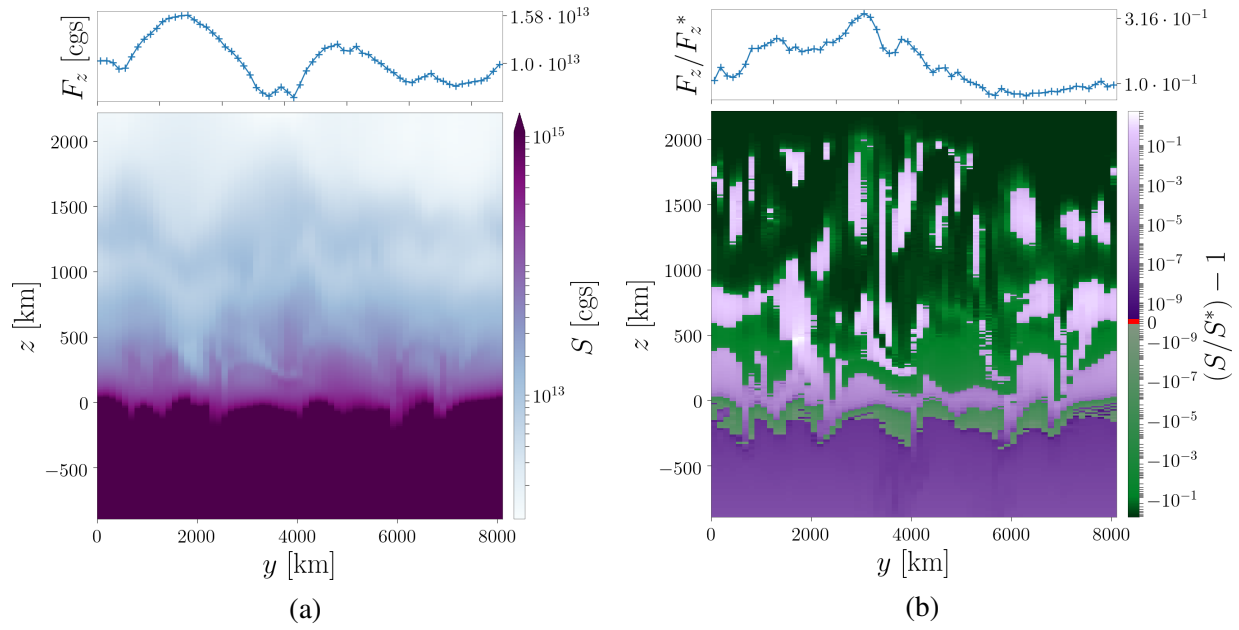
Vertical directed flux F_z^* in LTE (a), vertical directed flux F_z in NLTE (b, top) and the NLTE to LTE ratios F_z/F_z^* (b, bottom) around the line centre of the Ca II K line for model 1.

Each figure depicts the maximum (black dotted line), minimum (orange dotted line), mean (solid orange line), median (solid blue line), ninety-fifth percentile (blue dashed and dotted line) and fifth percentile (black dashed and dotted line) computed for the outermost layer of the model atmosphere.

its LTE value F_z^* in $H\alpha$, the Ca II K line exhibits a significant variation between most of the layer averaged quantities. Not only do all displayed averaged NLTE flux quantities indicate a clear flux reduction when compared to the LTE counterparts but they also experience a noteworthy cutback in the relative deviation of complementary quantities, like the minimum and maximum flux. This is to say that the surface flux contrast decreases as a result of NLTE-effects. The mean and median values are, again, very close to each other over the full presented range and demonstrate a similar level of absolute flux reduction in the line centre as $H\alpha$.

Inspecting the source function S in NLTE in fig. 3.10a non negligible structures can be spotted in all layers of the model's atmosphere. However, the shifted source function ratio $(S/S^*) - 1$, depicted in fig. 3.10b, reveals that many prominent structural features of the source function in LTE are being washed out by NLTE-effects in all layers above the photosphere. This loss of structural features in the chromosphere's source function goes well with the reduction of the surface flux contrast observed above and may well explain the line profile's steepening towards its line centre.

Figure 3.10



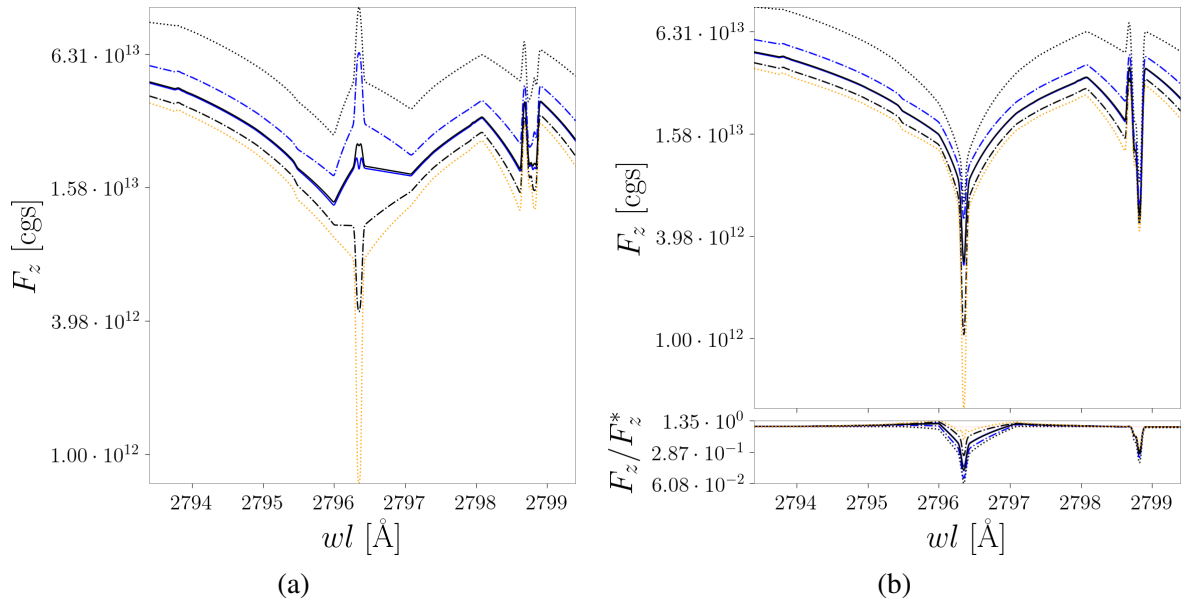
The vertical directed flux F_z vs. latitude y in NLTE at the surface (a, top), a color-map of the source function S (a, bottom), the NLTE to LTE vertical directed flux ratios F_z/F_z^* vs. latitude y at the surface (b, top) as well as a color-map of the reduced NLTE to LTE source function ratio $(S/S^*) - 1$ in the line centre of the Ca II K line for an arbitrary vertical slice through model 1.

The Mg II H and K lines are also regarded as prominent indicators for chromospheric activity as they exhibit a “larger opacity [than the Ca II H and K doublet] and hence, are very sensitive to temperature, density and velocity gradients in the chromosphere” (Staath and Lemaire, 1995). Figures 3.9a and 3.9b show the vertical directed flux at the surface F_z^* in LTE, F_z in NLTE and their associated LTE to NLTE flux ratios for the Mg II K line.

On the one hand, the Mg II K line’s LTE averaged quantities present distinctly different profile shapes accompanied by huge divergences in the values of complementary quantities. While the maximum, ninety-fifth percentile, mean and median flux exhibit increasing emission towards the line centre, the opposite is presented by the fifth percentile and minimum flux. Furthermore it is noteworthy that the mean and median flux show non vanishing differences close to the line centre.

On the other hand, the NLTE flux reveals a very different Mg II K line in almost all regards. All of its surface average quantities show a significant decrease of flux towards the core and a rapprochement of the complementary quantities. Aside from that, there are notable differences between the maximum, mean and minimum profile shapes about 0.5 \AA from the line centre at

Figure 3.11



Vertical directed flux F_z^* in LTE (a), vertical directed flux F_z in NLTE (b, top) and the NLTE to LTE ratios F_z/F_z^* (b, bottom) around the line centre of the Mg II K line for model 1.

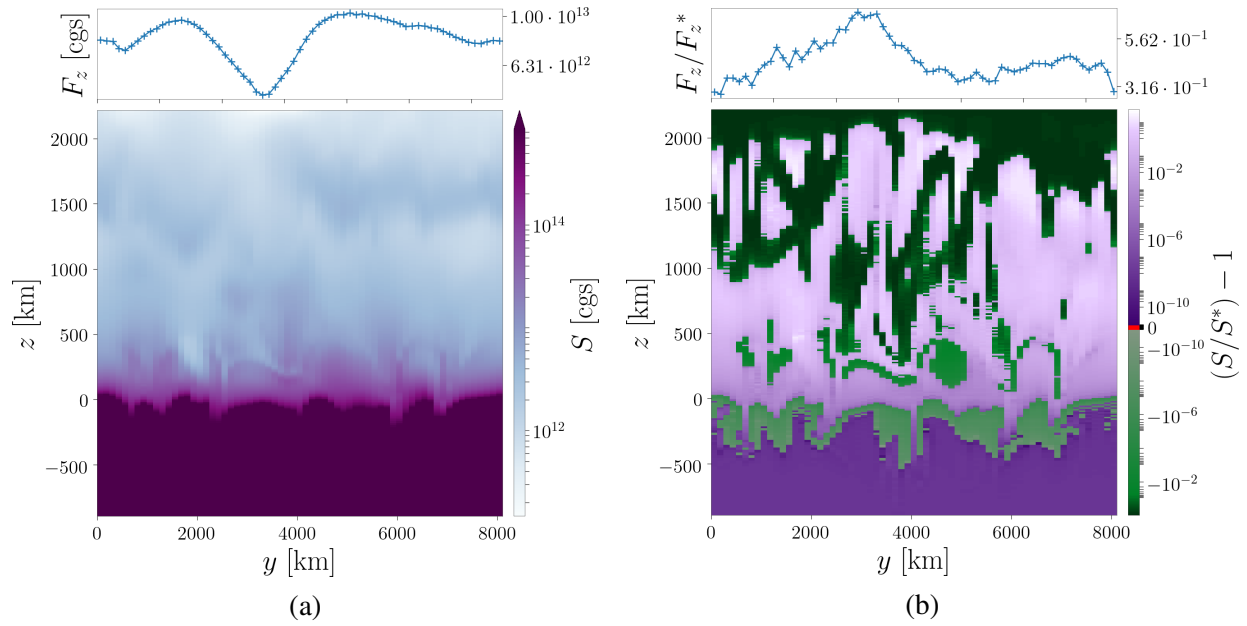
Each figure depicts the maximum (black dotted line), minimum (orange dotted line), mean (solid orange line), median (solid blue line), ninety-fifth percentile (blue dashed and dotted line) and fifth percentile (black dashed and dotted line) computed for the outermost layer of the model atmosphere.

about 2796 Å (referenced blue region) and 2797 Å (referenced red region) manifesting themselves, for example, as a visible kink in the curvature of the surface averaged flux quantities at about the blue region.

The NLTE to LTE flux ratios display further properties, especially about the aforementioned regions. In both regions all flux quantities but the maximum flux show a marginal flux increase when compared to the LTE value, whereas the ratio corresponding to the maximum flux decreases. Closing in to the line centre all flux quantities fall below their respective LTE values again.

Bearing in mind the similar interpretation value and proposed line generation altitude, it comes as no surprise that the color-map of the NLTE source function for the Mg II K line centre looks very much alike the corresponding color-map for the Ca II K line centre. A look at the shifted LTE to NLTE source function ratio reveals, once more, that much of the LTE structures are being levelled by NLTE effects. Interestingly, the shifted source function ratios of H α and the Ca II K line predominantly show a strong reduction of the source function in the chromosphere. This is not entirely true for the Mg II K line. Throughout most of its chromospheric layers it

Figure 3.12



The vertical directed flux F_z vs. latitude y in NLTE at the surface (a, top), a color-map of the source function S (a, bottom), the NLTE to LTE vertical directed flux ratios F_z/F_z^* vs. latitude y at the surface (b, top) as well as a color-map of the reduced NLTE to LTE source function ratio $(S/S^*) - 1$ in the line centre of the Mg II K line for an arbitrary vertical slice through model 1.

shows large patches of relative increase of the source function with respect to its LTE value. Nevertheless, a strict decrease of the surface flux and reduction of the source function in all the uppermost layers of this model's atmosphere can be found.

At the same time, and possibly by coincidence, the NLTE to LTE flux ratio shows a good correlation with the perceived cumulative brightness/darkness along the columns of the source function. That is to say that the NLTE to LTE flux ratio decreases the least for columns featuring many bright (white to pink) voxel and few dark (green to black) voxel. Similar observations can also be made for $H\alpha$ and the Ca II K line.

3.2.2 Model 2

The hydrodynamic structure of model 2 is also based on structure 1. This model treats iron and its first two ionisation stages (Fe I-III), hydrogen (H I), helium and ionised helium (He I-II) in NLTE. For the sake of feasibility, the resolution of the underlying input structure for this model had to be decreased to 33 by 33 by 233 voxel, in x -, y - and z -direction respectively. It was derived in the same way as described above for model 1. This procedure obviously and

notably reduces the contrast of the thermodynamic quantities, as presented in fig. 3.1. In return it permits the inclusion of iron in the 3D NLTE calculations, exhibiting a huge number of states and line transitions and, therefore, demanding massive amounts of computational resources.

The wavelength grid set-up is identically to the set-up in model 1, starting at 50 Å and reaching up to $1 \cdot 10^7$ Å in non-equidistant steps. In addition to the mandatory remaining LTE lines, a total of 2413 atomic levels, 59642 line transitions, 116600 coupled lines and 2410 coupled continua were considered in NLTE.

The importance and meaning of the vertical directed, surface flux $F_z(\lambda)$ has been stated before. Consequently, it is of great interest to inspect its shape and properties both in general and for specific lines. Figures 3.13a to 3.13c show the geometric mean over the surface voxels of the vertical directed flux F_z and its relative deviations from its corresponding LTE value F_z/F_z^* .

The general shape of the model's flux is, unsurprisingly, very similar to that presented in model 1 as the model is based on the same hydrodynamic structure. The model, anew, shows the typical characteristics of a Sun-like atmosphere featuring its highest monochromatic flux values in the visible and near ultra-violet wavelength range and peaking at around 4100 Å.

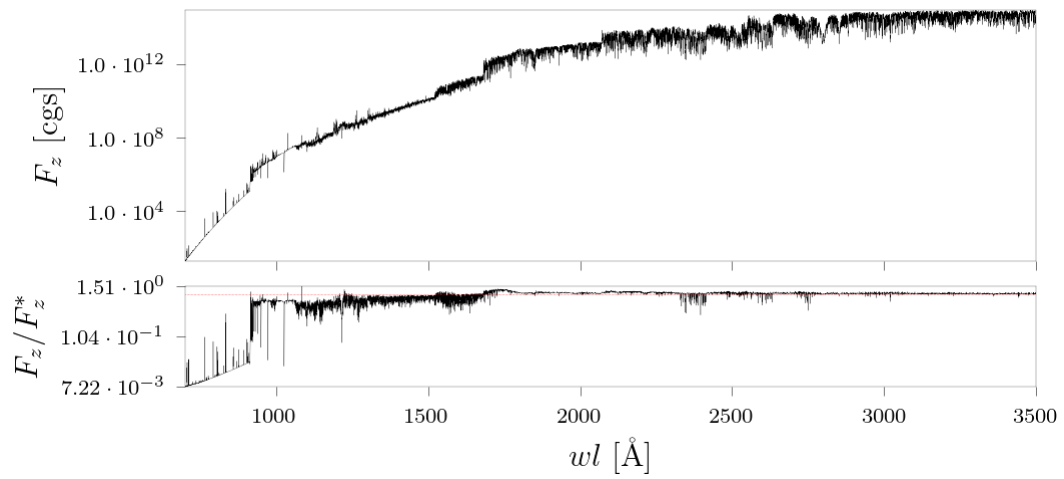
The biggest relative differences between the NLTE- and the LTE-calculations are found in the (far) ultra-violet. Moving towards higher photon-energies, starting at about the neutral iron photoionisation edge at 1575Å, the NLTE to LTE flux ratio decreases drastically.

In the visible range the relative deviations are generally smaller than in the ultra-violet. The $H\alpha$ line at 6564.2 Å exhibits some of the biggest relative differences deepening the line centre by about 60% in comparison to its LTE flux value. Closing in on the ultra-violet bulks of iron (NLTE) lines demonstrate their effect on the mean of the outward directed surface flux by displaying many perceivable NLTE to LTE flux ratio variations. While the majority of NLTE lines shows a line deepening with respect to their LTE values, there is also a great number of lines showing a NLTE to LTE flux ratio notably about unity.

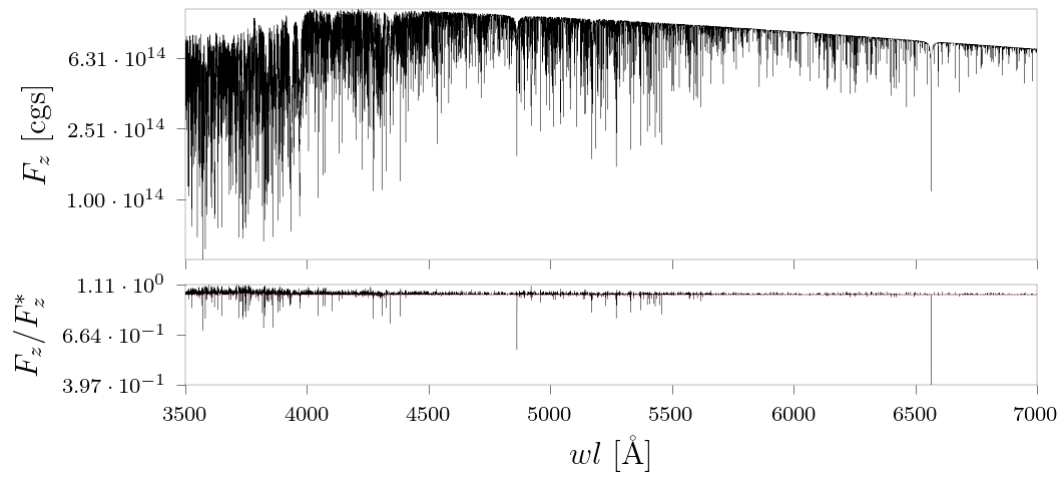
The infrared, however, shows next to no responds in terms of flux changes. A maximum of 2% in the flux ratio is reached by only one line, whereas the vast majority of deviations are much closer to zero.

Moving on to the discussion of individual lines, a set of interesting lines from the NLTE line species pool needs to be found. It is sensible to include $H\alpha$ in this analysis once more, as it

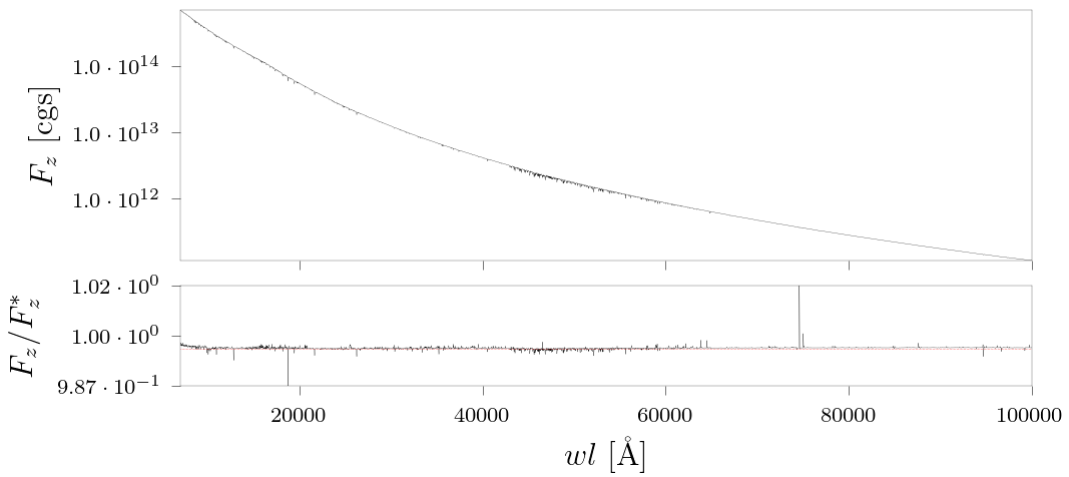
Figure 3.13



(a)



(b)



(c)

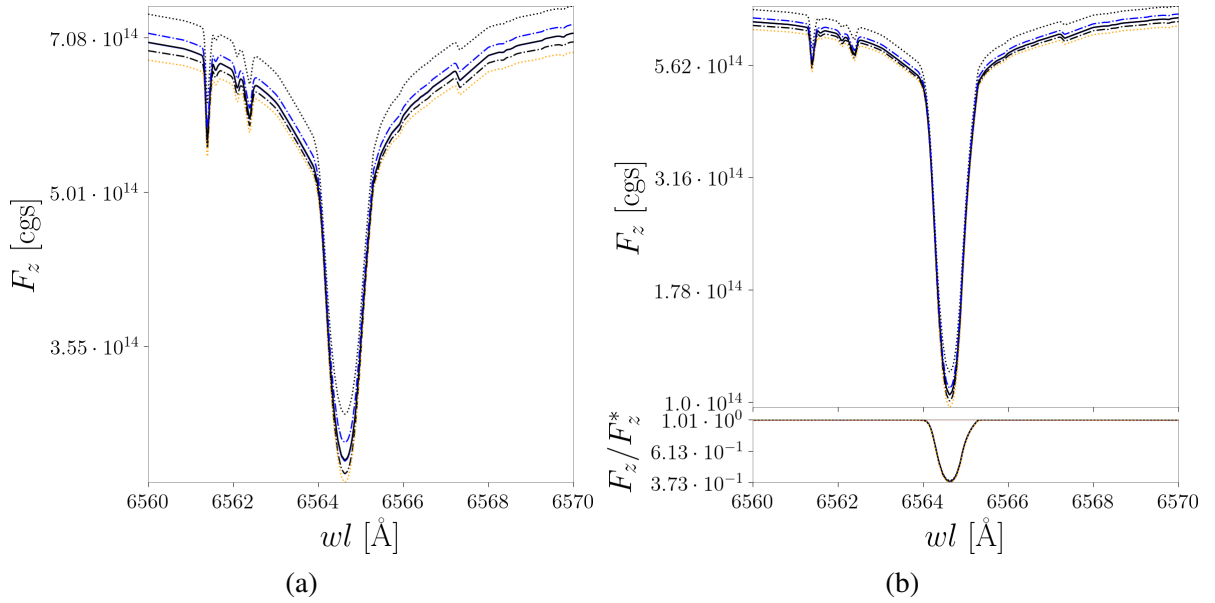
F_z vs. wavelength λ (top) and F_z/F_z^* vs. wavelength λ (bottom) in the ultra-violet (a), visible (b) and infrared (c) wavelength range for model 2. The red dotted line in the bottom panel is a visual guideline representing unity.

shows a significant deviation from its LTE flux value and, moreover, has also been discussed for model 1 above.

Additionally, it is interesting to have a look at the Fraunhofer iron e-line centred at 4384.8 \AA , representing a strong line of neutral iron under solar conditions. A singly ionised iron line, like Fe II 4585.1 \AA , may as well be worth a closer inspection, since “the lines of singly ionized iron (Fe II) [...] are very often formed far from LTE” (sic., Viotti et al., 2014, preface).

Starting with $H\alpha$, each of the previously introduced lines will be presented and discussed by inspecting the properties of the surface averaged quantities, i.e., maximum, minimum, fifth and ninety-fifth percentile, mean and median values, of the vertical directed flux F_z in the direct proximity of the line centres’ and the corresponding source functions S for the arbitrary selected vertical slice $ix = 20$ of the model.

Figure 3.14



Vertical directed flux F_z^* in LTE (a), vertical directed flux F_z in NLTE (b, top) and the NLTE to LTE ratios F_z/F_z^* (b, bottom) around the line centre of $H\alpha$ for model 2.

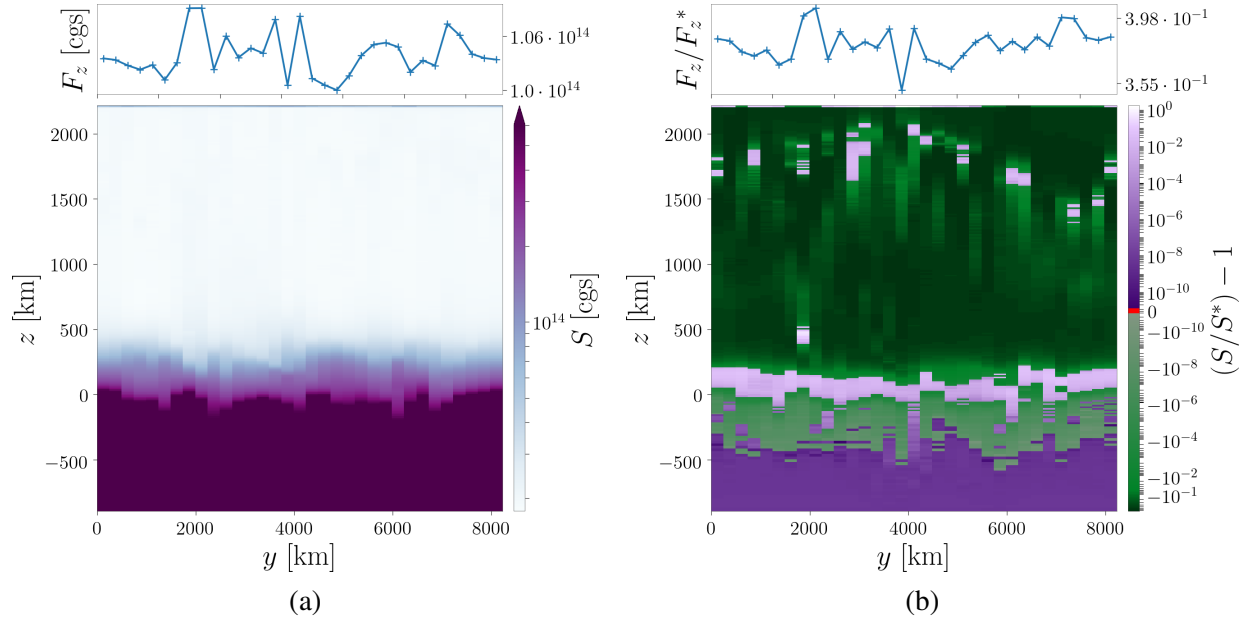
Each figure depicts the maximum (black dotted line), minimum (orange dotted line), mean (solid orange line), median (solid blue line), ninety-fifth percentile (blue dashed and dotted line) and fifth percentile (black dashed and dotted line) computed for the outermost layer of the model atmosphere.

The surface averaged quantities of the vertical directed flux in LTE F_z^* and NLTE F_z as well as their ratio are presented in figs. 3.14a and 3.14b. The general shape of both the LTE and NLTE line is very similar. Nevertheless, the NLTE to LTE flux ratio on the bottom righthand side of the figure clearly shows that the line depth is much higher in the NLTE case.

While there are notable differences between the surface averaged quantities, in both LTE and NLTE, there is no apparent variation between them in the flux ratios.

Assuming only small deviations from the LTE conditions in the line forming region a significant and rather uniform opacity increase, emission reduction or a combination of both in the layers above the lines formation region, the photosphere, would be the most likely explanation for the observed effect.

Figure 3.15



The vertical directed flux F_z vs. latitude y in NLTE at the surface (a, top), a color-map of the source function S (a, bottom), the NLTE to LTE vertical directed flux ratios F_z/F_z^* vs. latitude y at the surface (b, top) as well as a color-map of the reduced NLTE to LTE source function ratio $(S/S^*) - 1$ in the line centre of $H\alpha$ for an arbitrary vertical slice through model 2.

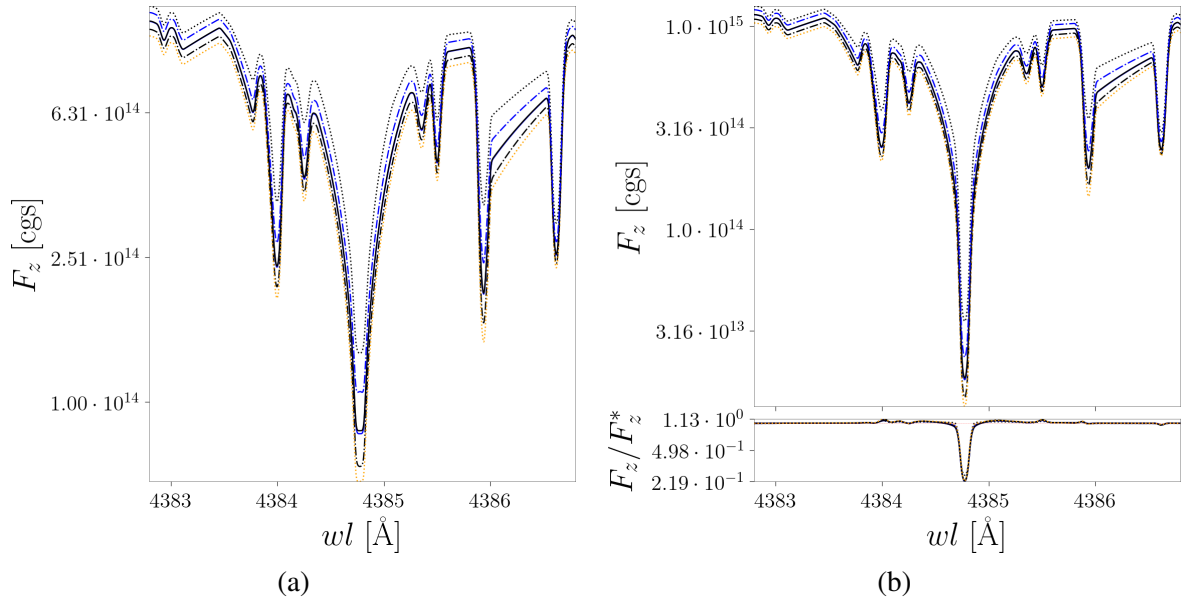
This hypothesis can be tested by looking at the NLTE source function and the reduced NLTE to LTE source function ratio presented in figs. 3.15a and 3.15b, respectively. The source function readily reveals that it is nearly uniform and low valued in the layers above the photosphere. In the opposite direction the source function increases by over 1 magnitude towards the upper convection zone at about $z = 0$ km.

The source function's high value (cut-off) edge, visible in the upper convection zone and lower photosphere, corresponds very well with the region in which the NLTE and LTE source functions are basically alike. It can also be expected to coincide with an optical depth value of well above unity for this line centre, meaning that photons in the regions below are essentially

trapped and are in fact very close to fulfilling the LTE assumptions.

Moreover, the NLTE source function substantially exceeds the LTE source function directly above of the previously discussed edge only to exhibit a sharp drop to values far below its LTE values in the region just atop. In most layers above the lower chromosphere notable variations can be spotted in the reduced NLTE to LTE source function ratio. These variation massively reduce the LTE source function's contrast and, therefore, result in a almost perfectly uniform NLTE source function.

Figure 3.16



Vertical directed flux F_z^* in LTE (a), vertical directed flux F_z in NLTE (b, top) and the NLTE to LTE ratios F_z/F_z^* (b, bottom) around the line centre of the Fe e-line for model 2.

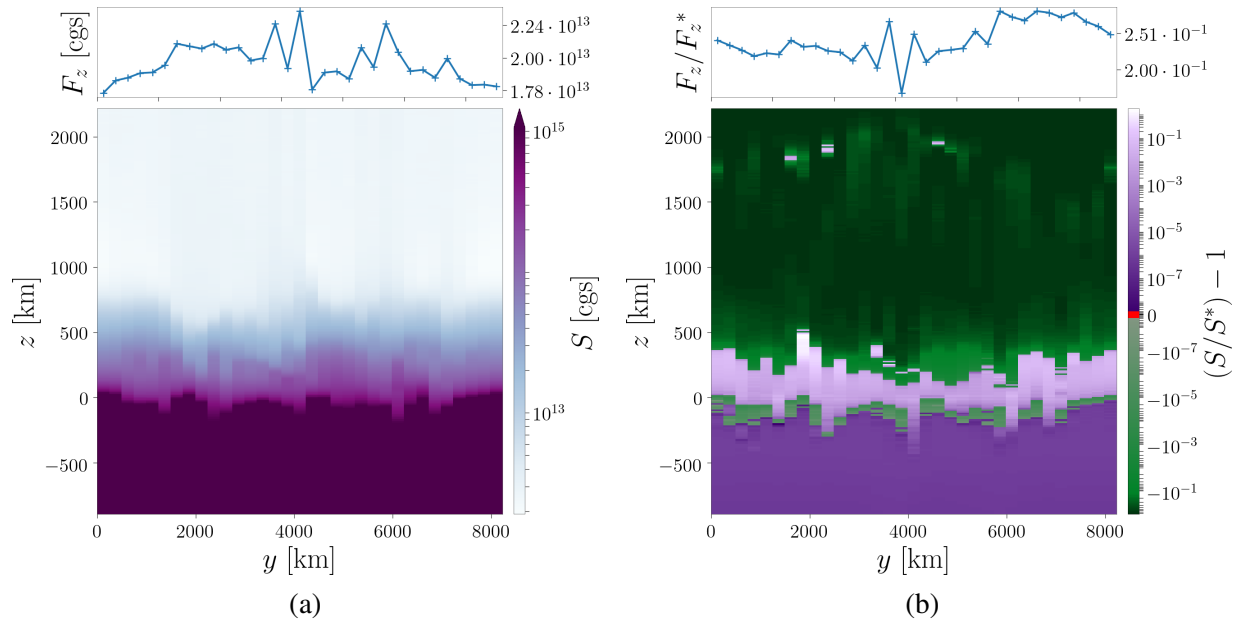
Each figure depicts the maximum (black dotted line), minimum (orange dotted line), mean (solid orange line), median (solid blue line), ninety-fifth percentile (blue dashed and dotted line) and fifth percentile (black dashed and dotted line) computed for the outermost layer of the model atmosphere.

The Fe I e-line is a well known and good example for a strong (neutral) iron absorption line in the Sun. The surface averaged quantities of the vertical directed flux in NLTE F_z and LTE F_z^* as well as their ratio F_z/F_z^* are presented in figs. 3.16a and 3.16b. While the general behaviour of this line is quite similar to the one observed in $H\alpha$, the plot also exhibit a few noteworthy differences.

Once more, the NLTE effects have a reasonably strong impact on the central line depth of the iron e-line, demonstrating a relative NLTE to LTE flux reduction of about 78%. All flux quantities show near identical depth increases next to the line's centre. The only perceivable

exception to this can be detected for the surface averaged maximum flux showing a marginally less pronounced relative flux reduction. Therefore, the minimum to maximum deviation decrease, overall causing a small reduction of surface flux contrast in and about the line centre. Quantitatively, the iron e-line centre demonstrates a behaviour comparable to that of $H\alpha$ in this model.

Figure 3.17



The vertical directed flux F_z vs. latitude y in NLTE at the surface (a, top), a color-map of the source function S (a, bottom), the NLTE to LTE vertical directed flux ratios F_z/F_z^* vs. latitude y at the surface (b, top) as well as a color-map of the reduced NLTE to LTE source function ratio $(S/S^*) - 1$ in the line centre of Fe e-line for an arbitrary vertical slice through model 2.

Further knowledge can be gained by inspecting the NLTE source function S and the reduced NLTE to LTE ratio $(S/S^*) - 1$, presented in figs. 3.17a and 3.17b. The source function is expectedly very close to LTE conditions in the convection zone but it presents itself massively super-thermal for the majority of the voxels in the photospheric layers.

Nonetheless, this source function excess seems to be counteracted by a predominately sub-thermal source function in nearly all voxel in the layers above the photosphere, which is in accordance with the mostly uniform relative flux reduction in the line centre mentioned above. Taking a look at the NLTE source function above the photosphere indicates that the few voxel displaying a super-thermal source-function in the reduced NLTE to LTE ratio are most likely the result of levelling NLTE effects.

In sum, a striking resemblance between the reduced NLTE to LTE source function ratios of the iron e-line and $H\alpha$, at their respective line centre wavelength, can be found. The width of the super-thermal region in the photosphere differs most notably and may, possibly, cause the slightly less pronounced relative reduction of the maximum flux.

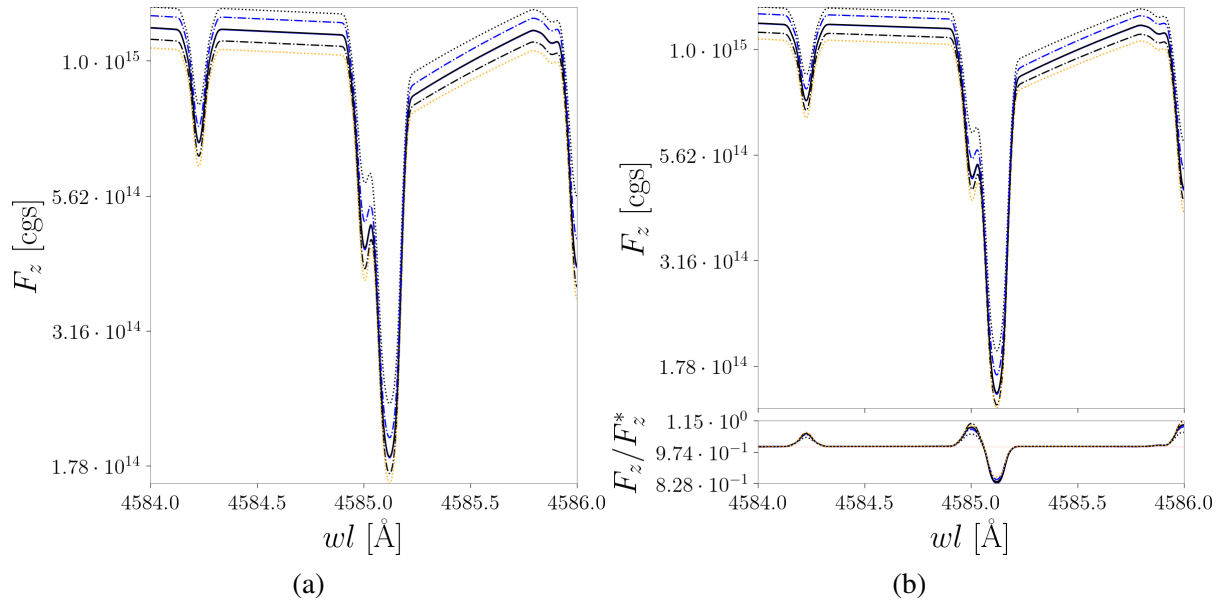
As pointed out above, many singly ionised iron lines are said to be rather sensitive to NLTE effects with respect to their line formation. Hence, the inspection of a Fe II line representative, centred at 4585.1 \AA , may provide additional information on this topic. Figures 3.18a and 3.18b present this line's surfaces averaged quantities of the vertical directed flux in LTE F_z^* and in NLTE F_z . As it is the case for most lines discussed so far, the Fe II line exhibits a notable deepening of about 17% at the line centre. There are no perceivable variations between the surface averaged quantities, indicating a resemblance with the behaviour of $H\alpha$, yet again.

In the blue line wing another neutral iron line centred at 4585.0 \AA can be identified. In contrast to the Fe II line, it displays an increase in all surface averaged quantities when compared to its LTE values. However, this neutral iron feature will not be discussed any further, since only an in-depth analysis, considering the occupation numbers and more, would be able to reveal a possible connection between both neighbouring lines.

The source function S and its reduced NLTE to LTE source function ratio $(S/S^*) - 1$ are displayed in figs. 3.19a and 3.19c. The NLTE source function is far from uniform and even shows clearly visible variations in the chromosphere and is, therefore, very unlike the $H\alpha$ - and the Fe e-line's source function. The reduced NLTE to LTE ratio exhibits large patches of connected sub-thermal regions facing comparably large patches of super-thermal region throughout the whole atmosphere starting in the photosphere. It is rather difficult to explain the uniform reduction of the surface averaged flux quantities in light of the source function and its ratio alone.

A closer look at the LTE source function reveals, nevertheless, that a significant reduction of the contrast level in the chromosphere has taken place for the NLTE source function when compared with its LTE values. In fact, most bright, white spots in the chromosphere, signalling source function values of below 10^{13} , correspond to a comparatively high LTE source function value of several 10^{14} , best seen in fig. 3.19b. Seeing these rather massive changes in the source function having next to no impact on the surface averaged flux quantities makes it plausible that the actual contribution to the surface flux is very limited in the layers above the lower photosphere. Based on the presented results it is save to say that the formation of this line is not

Figure 3.18

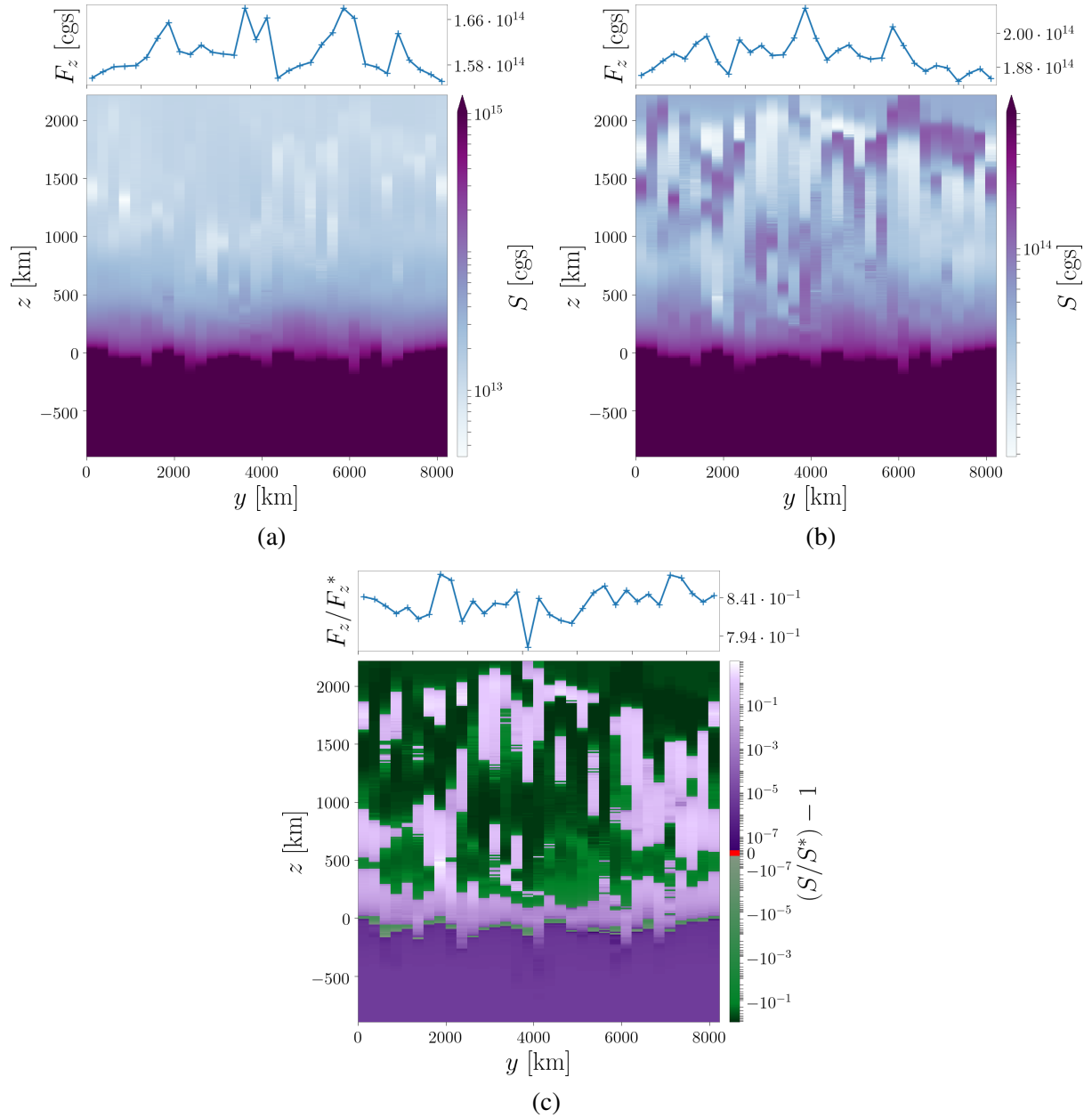


Vertical directed flux F_z^* in LTE (a), vertical directed flux F_z in NLTE (b, top) and the NLTE to LTE ratios F_z/F_z^* (b, bottom) around the Fe II line centred at 4585.1 Å for model 2.

Each figure depicts the maximum (black dotted line), minimum (orange dotted line), mean (solid orange line), median (solid blue line), ninety-fifth percentile (blue dashed and dotted line) and fifth percentile (black dashed and dotted line) computed for the outermost layer of the model atmosphere.

as easily described as it was the case for H α and the Fe e-line. The effect of the NLTE treatment on the averaged surface flux quantities of this Fe II line is, however, surprisingly similar to the effects observed for the other lines in this model.

Figure 3.19



The vertical directed flux F_z vs. latitude y at the surface and in NLTE (a, top) and in LTE (b, top), a color-map of the respective source function S (a, bottom) and (b, bottom), the NLTE to LTE vertical directed flux ratios F_z/F_z^* vs. latitude y at the surface (c, top) as well as a color-map of the reduced NLTE to LTE source function ratio $(S/S^*) - 1$ in the line centre of the Fe II line centred at 4585.1 Å for an arbitrary vertical slice through model 2.

3.3 Model comparison

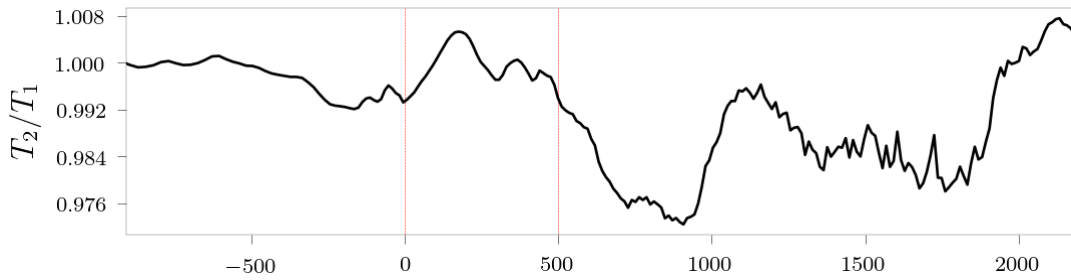
Having inspected the general properties and a few hand-selected spectral line features of the two radiative transfer models models 1 and 2 in the previous sections, further insight can be

gained by comparing their results to one another. In addition to this comparison, it is of major interest to compare the results to a suitable 1D NLTE radiative transfer model.

3.3.1 3D model comparison

As described above the models' input structures differ only in the number of voxel per layer. In consequence, there are minor deviations between the models' layer averaged quantities, like the mean of the temperature, gas pressure and density. Due to the linearity of the interpolation procedure the mean temperature, gas pressure and density ratios T_2/T_1 , $P_{gas,2}/P_{gas,1}$ and ρ_2/ρ_1 behave exactly alike, where the subscripts 1 and 2 refer to model 1 and 2, respectively. Figure 3.20 shows the ratio of the layer averaged mean temperature profile and exhibits no de-

Figure 3.20



Layer averaged mean temperature ratio T_2/T_1 vs. altitude z from the outermost convection zone to upper chromosphere.

The subscripts 1 and 2 refer to model 1 and 2, respectively.

The vertical lines (red dashes) indicate the approximate transition height from convection zone to photosphere and from photosphere to chromosphere.

viations larger than 2.8% for any given altitude between both models. It is difficult to assess the impact of these deviations a priori, since the mean temperature ratio varies significantly throughout the atmosphere. The ratio is, however, way less pronounced in the photospheric layers. This observation is of major importance, since the photosphere is the region of an atmosphere from which most of the radiation in the visible range originates.

A very crude but informative estimate of the relative error induced by these deviation can be obtained by comparing the energy densities of two *black bodies* at different temperatures. A black body's energy density can be calculated by integrating the Planck function eq. (2.5.9) over the wavelength space and is proportional to the fourth power of its temperature T^4 . Consequently, the energy density ratio goes with the fourth power of the temperature ratio $(T_2/T_1)^4$. If

the continua or spectral lines were to be formed close to the aforementioned temperature ratio peak of 0.972 at about 900 km, the resulting expected deviation would be of order 11%.

An inspection of numerous layer averaged mean flux profiles indicates, however, that the optical continua are, in fact, generated within the region between convection zone and photosphere and the photosphere itself. The temperature ratio in the photospheric layer is, however, less than 1.008. Thus, relative energy density differences of about a 3% could be presumed between both the models.

And while the calculation of another reference model would remove the necessity of such an estimate, it would require significant additional computational resources. Therefore, such simulations could be suited very well for follow up projects as they could probe the effect of convoluted data on 3D radiative transfer problems.

On the base of the estimates given above, it is reasonable to expect relative surface flux deviations of similar order caused by the resolution scaling. Hence, relative differences going beyond this 3% level can be most likely attributed to the effect of differing NLTE species between the models.

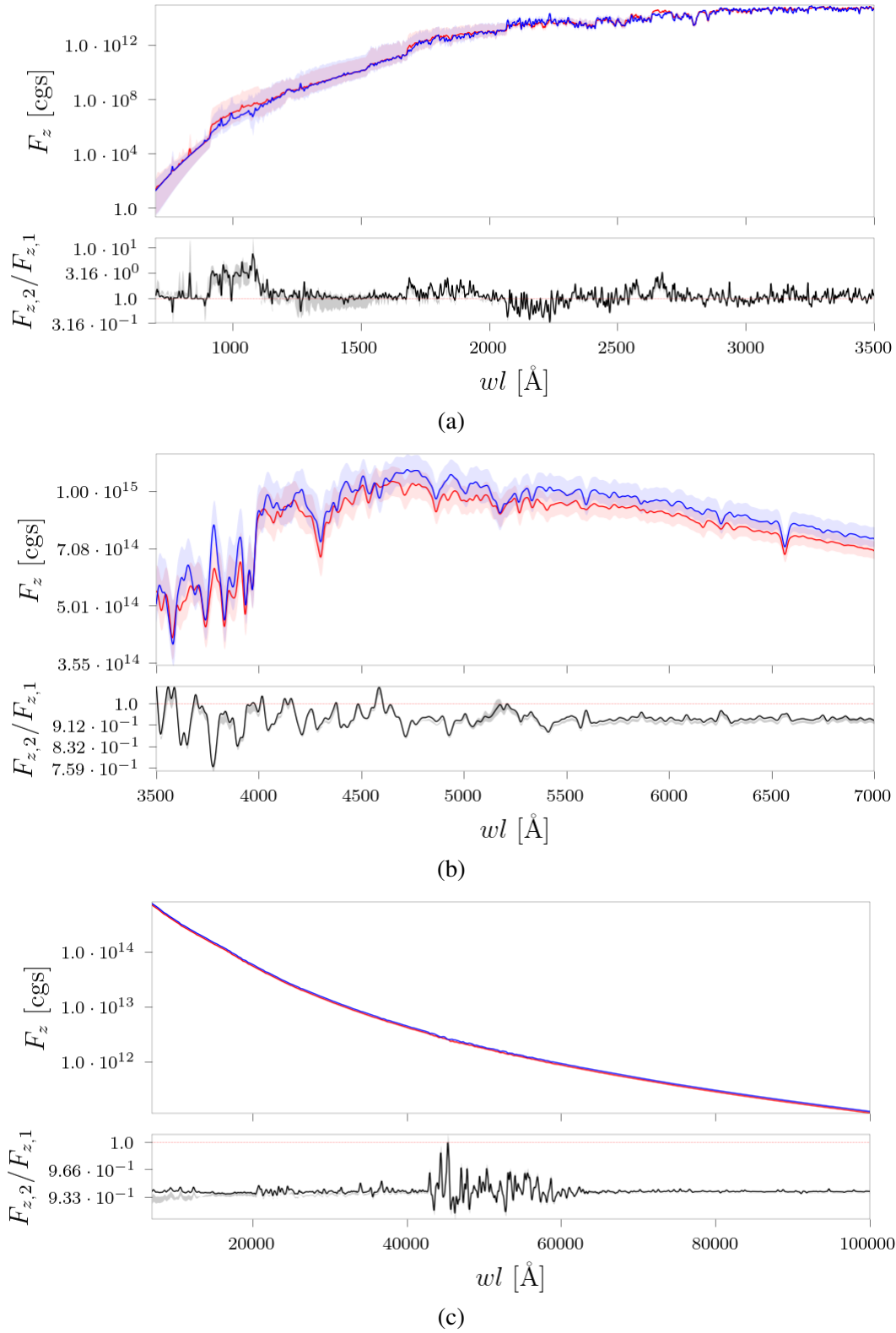
In the style of the previous section the flux information will be presented for the ultra-violet, the visible and the infrared wavelength ranges. Figures 3.21a to 3.21c present the surface averaged mean of the vertical directed flux of both models, their respective minimum to maximum span, and their flux ratio interpolated to a resolution of 2, 10 and 100Å, respectively. Consequently, most line features are massively blended in this representation highlighting the models' differences in their continua.

The most significant relative change in flux between the two models can be found in the ultra-violet wavelength range, featuring a plateau with a ratio value of close to 3 at about 1000 Å. Moreover, there are many wavelength ranges displaying flux ratios, both, notably below and above unity.

Having a look at the maximum to minimum span two interesting properties are eye-catching. First, there is a massive decrease in the relative deviation between maximum to minimum flux values towards larger wavelength in the upper panel. Second, the maximum and minimum flux ratios in the lower panel closely resembles the mean flux ratios, showing perceivable differences only in the wavelength range below 1600 Å.

The picture is notably different in the visible wavelength range. The most distinct feature is

Figure 3.21



Surface averaged vertical directed flux F_z vs. wavelength λ (top) for model 1 (blue) and model 2 (red) and their ratios $F_{z,2}/F_{z,1}$ vs. wavelength λ (bottom) in the ultra-violet (a), visible (b) and infrared (c) wavelength range.

The solid lines represent the corresponding mean values, while the pallid region cover the respective minimum to maximum values.

The subscripts 1 and 2 refer to their associated model and the red dotted line in the bottom panel is a visual guideline at unity.

a clear shift in the baseline of the flux between model 1 and model 2. Throughout nearly the entire wavelength range model 2 shows a significant relative deviation, peaking at about 3780 Å with a ratio of 0.76 and stabilizing at about 0.91 towards the infrared.

The flux ratio in the infrared exhibits a close to constant value about 0.93. It only comes close to unity at about 45300 Å, while also showing its largest variations in the range between 45000 Å and 60000 Å.

Negative hydrogen H^- and, to a lesser extent, the Paschen-continuum (corresponding to the hydrogen $n = 3$ bound-free transitions) are the major contributors to a Sun-like atmosphere's continuum opacity in the visible wavelength range. Hence, it is reasonable to relate the described behaviour to a change in the electron and the hydrogen number densities induced by the NLTE treatment of iron in model 2.

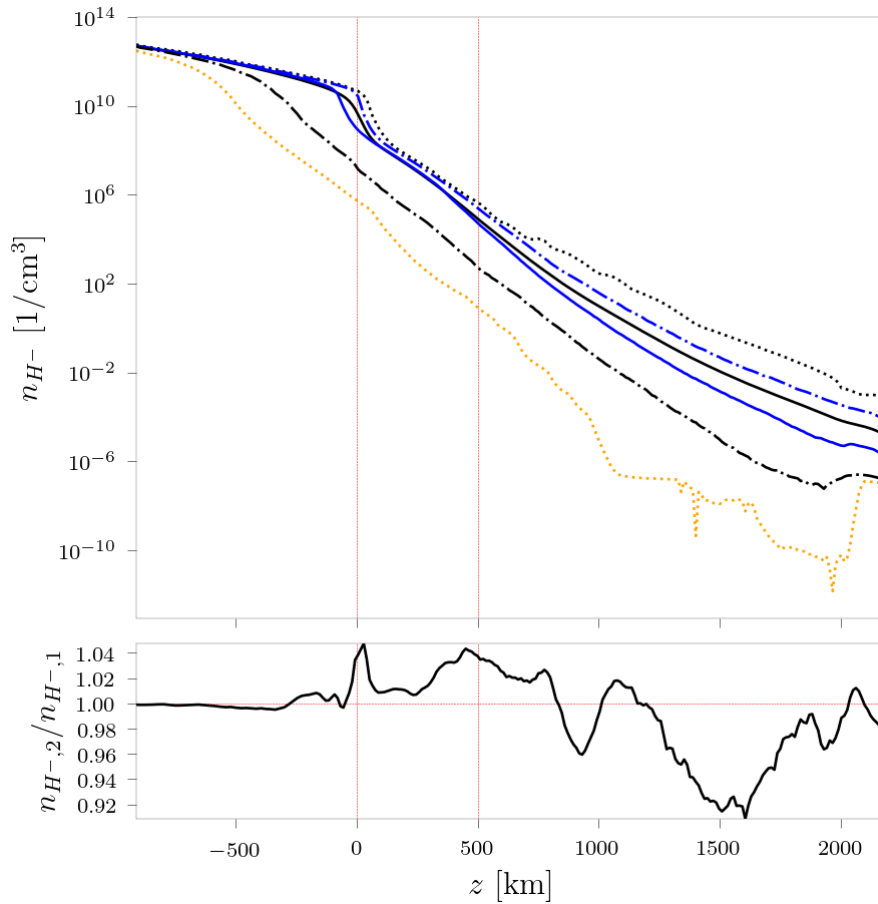
For this reason figs. 3.22, 3.23a and 3.23b display the layer averaged maximum, minimum, ninety-fifth and fifth percentile, mean and median for the number densities of negative hydrogen and hydrogen $n = 3$ as well as the electron number densities from model 2. Additionally, the inter-model mean ratio for each of the above number densities is given, e.g., the mean electron density ratio $n_{e,2}/n_{e,1}$ with subscripts corresponding to model 1 and model 2, respectively.

In the number density of negative hydrogen n_{H^-} , found in fig. 3.22, three regions of distinctly differing slopes can be identified. Throughout most of the convection zone the number density decreases slowly and the mean value of both models are in good agreement with one another. At the same time the difference between the layer averaged minimum and maximum increase steadily while both mean and median values stay well aligned.

Closing in on the photosphere the number density's behaviour starts to change drastically. The maximum, ninety-fifth percentile, mean and median number density values drop about 3 magnitudes over a small number of layers. Moreover, the mean and median values start to show notable deviations and the inter-model mean ratio reaches up to hit its peak value at the beginning of the photosphere showing a relative increase of about 4.7% in model 2. For quick reference, the mean temperature, gas pressure and density inter-model ratio value is smaller than 0.8% at comparable altitudes.

In the photosphere the maximum to minimum, as well as the ninety-fifth to fifth percentile differences reach a global minimum and slowly start to increase again towards the chromosphere. At altitudes about this minimum the inter-model number density ratio is close to unity and rises,

Figure 3.22



Number density n of H^- (top) vs. altitude z of model 2 and the mean number density ratio n_2/n_1 vs. altitude z as compared to model 1 (bottom).

The maxima (black dash-dots), minima (black dashes), mean (blue dots), median (blue solid), fifth- and ninety-fifth percentiles (orange dash-dots and orange dots) calculated at each altitude z of layer iz along the z -axis.

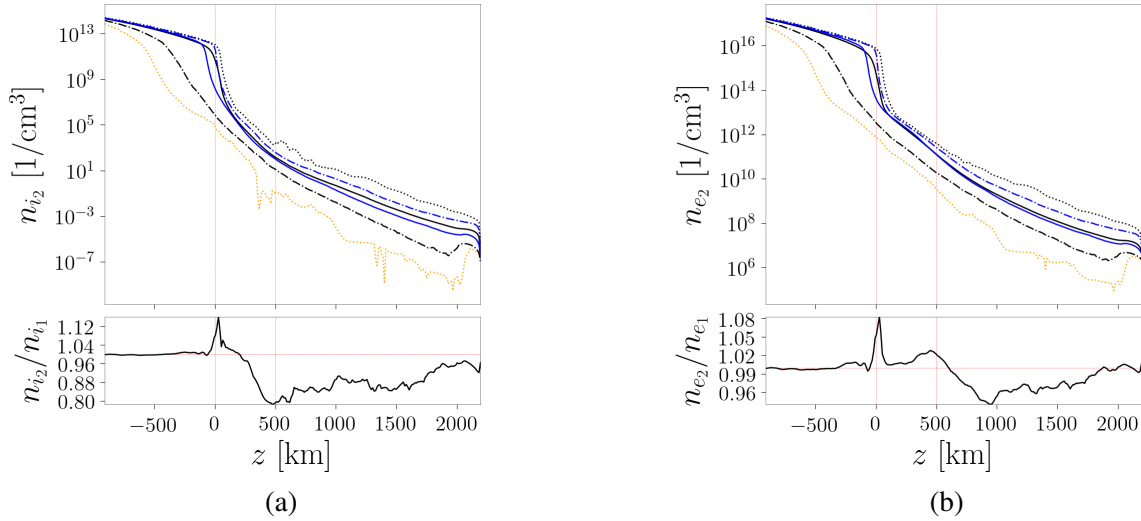
The subscripts 1 and 2 refer to their associated model and the vertical lines (red dotted) indicate the approximate transition height from convection zone to photosphere and from photosphere to chromosphere.

once more, to values just below the previous peak value in the upper photosphere.

Rising in altitude, the negative hydrogen number density decreases steadily and slowly towards the models surface. Its inter-model ratio, however, varies notably, dropping to a ratio value of 0.96 at about 930 km, reaching up again to just below 1.02 at about 1070 and falling to its global minimum of 0.9 at 1600km. Closing in on the model's surface a rapprochement of mean number density values can be observed.

Putting these results into context, a correlation between the systematically reduced flux in the visible wavelength range and the relative increase of the local H^- abundance can be seen. These increases can be found in a narrow but strong peak in the transition region between the convec-

Figure 3.23



Occupation number n_i for hydrogen in its second excited state (a, top) and electron number density n_e (b, top) vs. altitude z for model 2 and their respective mean ratios $n_{i,2}/n_{i,1}$ and $n_{e,2}/n_{e,1}$ as compared to model 1 (a & b, bottom).

The maxima (black dash-dots), minima (black dashes), mean (blue dots), median (blue solid), fifth- and ninety-fifth percentiles (orange dash-dots and orange dots) calculated at each altitude $z(i, z)$ of layer i, z along the z -axis.

The subscripts 1 and 2 refer to their associated model and the vertical lines (red dotted) indicate the approximate transition height from convection zone to photosphere and from photosphere to chromosphere.

tion zone and photosphere as well as in a wider but slightly less pronounced peak in the upper photosphere. The photosphere is usually regarded as the formation region of the continua and many lines in the visible wavelength range. This corresponds very well to the relative rise of the H^- number density found in the photosphere since its associated opacity increases which leads to a reduced flux in the visible wavelength range. The opposed relative reduction of the H^- number density in the chromosphere does not seem to have a substantial influence on the flux and indicates that it does not play a crucial part in the formation of the visible continua.

Another, but not quite as important, opacity source in the visible wavelength range is associated to the bound-free transition of the second excited state of hydrogen, as stated above. The number density of this hydrogen state is presented in fig. 3.23a. Its general shape is rather similar to that of the negative hydrogen's number density.

The inter-model mean number density ratio shows a pronounced relative increase in the region between convection zone and photosphere and an even stronger relative decrease to about 0.8 in the transition region from photosphere to chromosphere. This ratio stays well below

unity throughout most of the chromosphere but re-approaches unity in the upper chromospheric layers, again.

In the lower photosphere, both, the number density of negative hydrogen and of the second excited state of hydrogen display substantial relative increases with respect to model 1. In the upper photosphere, however, they demonstrate opposing behaviour. Depending on the actual formation altitude of the Paschen-continuum the relative decrease of its corresponding number density would lead to different expectations.

Taking into account the non-locality imposed by the NLTE treatment of hydrogen and other species in addition to the huge differences in the total number density, the detailed identification and correlation of the previously discussed features is unfortunately anything but trivial.

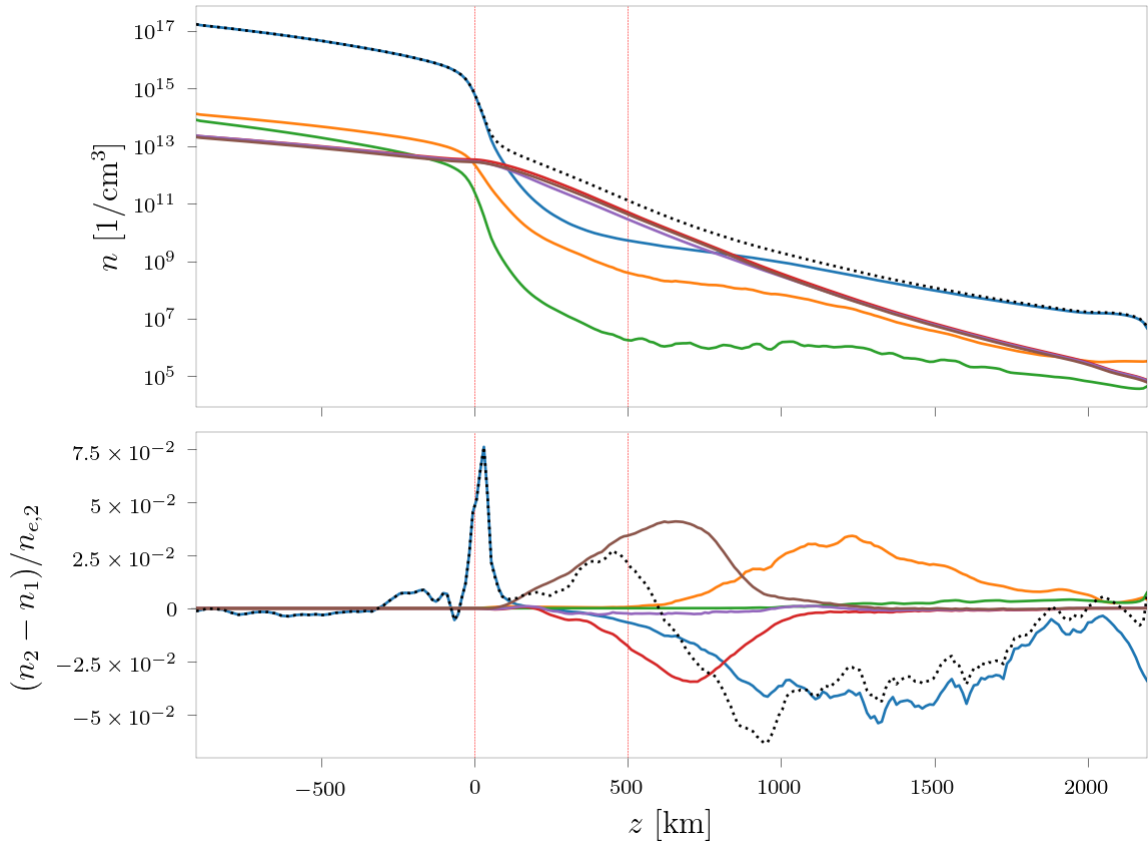
Being a prerequisite for the existence of negative hydrogen, the electron number density and its behaviour are tightly correlated with the number density of negative hydrogen. Therefore, it is hardly surprising that, both, the general shape and the inter-model number density ratio demonstrate very similar behaviour.

While both peaks discussed for the negative hydrogen inter-model ratio can also be found in the corresponding electron number density ratio, the first peak at the beginning of the photosphere is notably larger. In turn, the second peak is less pronounced in the mean electron number density ratio. Nevertheless, both ratios follow a rather similar trend.

Following the same train of thought, it is instructive to have a look at the most important electron donators. Looking for the 3 largest mean number densities of ionised atomic species in each layer result in a list of 6 ionised species, namely H II, C II, O II, Mg II, Si II and Fe II. Figure 3.24 presents the number densities for each of these species and the electron of model 2, as well as their inter-model differences with respect to model 1, normalised to the electron number density corresponding to model 2. Inspecting the top panel of this figure readily reveals the selected ionised species' contributions to the electron number densities. Ionised hydrogen serves as the biggest electron donator for large parts of the model's atmosphere. The only exception can be found in the region between the photosphere and the lower chromosphere, ranging from about 100km and just below 1000km, where, both, ionised magnesium and ionised iron show number densities surpassing that of ionised hydrogen.

The normalisation to the electron number density of model 2 on the bottom panel provides a very clear picture of which species' number density changes have a significant impact on

Figure 3.24



Number densities n (top) vs. altitude z of model 2 and their absolute differences normalised to the electron number density $(n_2 - n_1)/n_{e,2}$ vs. altitude z as compared to model 1 (bottom).

The layer averaged mean number densities and their normalised inter-model differences are displayed for a set of selected ionised species H II (blue line), C II (orange line), O II (green line), Mg II (red line), Si II (purple line) and Fe II (brown line) as well as for the electron (black dotted line). The subscripts 1 and 2 refer to their associated model and the vertical lines (red dotted) indicate the approximate transition height from convection zone to photosphere and from photosphere to chromosphere.

the electron number density ratio discussed above. On the one hand, there is no doubt that the prominent peak in the normalised differences of both ionised hydrogen and the electron at about 100km is caused by a considerable increase of ionised hydrogen in model 2. Note that the electron number density ratio, discussed above, reduced by 1 is exactly equivalent to the normalised electron number density difference displayed here.

The second peak in the normalised electron number density difference, on the other hand, is closely related to the notable increase of ionised iron and overshadows the relative decrease of ionised magnesium and ionised hydrogen in the transition region between photosphere and chromosphere. As the latter gains importance once more, the normalised electron number den-

sity difference drops to its global minimum and basically follows the trend of the ionised hydrogen throughout the rest of the chromospheric layers.

3.3.2 3D to 1D model comparison

Having inspected the difference between both 3D models, it is interesting to compare the results to a suitable 1D model of a Sun-like atmosphere.

The 1D model presented here is based on a Phoenix/1D simulation with an effective temperature of $T_{\text{eff}} = 5770$, features a large number of NLTE species, namely H I, He I-II, C I-IV, N I-IV, O I-IV, Mg I-III and Fe I-IV, and will be referred to as model 3. Consequently, the model covers every NLTE species treated in the 3D models, except for calcium, and includes many additional ionisation stages.

There are a number of important differences between Phoenix/1D and Phoenix/3D radiative transfer models. While the latter calculates the radiation field for a given, unalterable 3D hydrodynamic input structure, Phoenix/1D finds a simultaneous solution for a static atmosphere structure and its radiation field, iteratively adapting the atmosphere structure to the new radiation field and vice versa by default.

The 1D model structure and its radiation field should, consequently, be understood as laterally and time-averaged result which is in stark contrast to the 3D models which are time snapshot of an evolving atmosphere. Given a large number of continuous time snapshots a time averaged surface flux should be representative for the simulated object, in this case a Sun-like stellar atmosphere. However, the hydrodynamic structure, as well as its radiation field and its correlated surface flux, vary due to the time-dependent of the simulation.

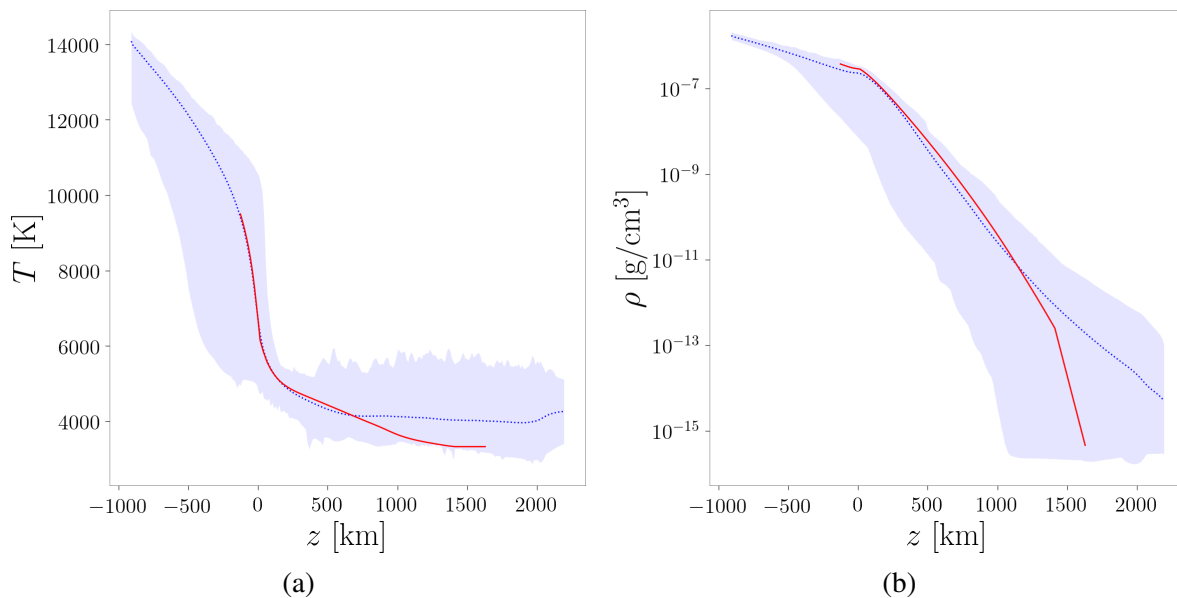
Hence, systematic deviations of the surface flux between the static 1D model and the 3D models have to be expected.

It is extremely challenging to find an adequate, static one dimensional description of the highly variable and fluctuating chromosphere. In 1D radiative transfer models generated with Phoenix/1D the chromosphere can not be generated self-consistently but can, however, in principle be treated semi-empirically by adding an arbitrary, predefined temperature structure as was demonstrated by Fuhrmeister (2005). For this reason, it is not included in the 1D model presented here.

A more consistent description of stellar atmospheres including the chromosphere can be ob-

tained by calculating time-dependent magnetohydrodynamic structures on which the previously presented 3D models are based. The chromosphere should be expected to contribute little to the flux in the visible and infrared wavelength ranges. In the ultra-violet wavelength range, however, the chromosphere can be anticipated to cause substantial changes on the surface flux.

Figure 3.25



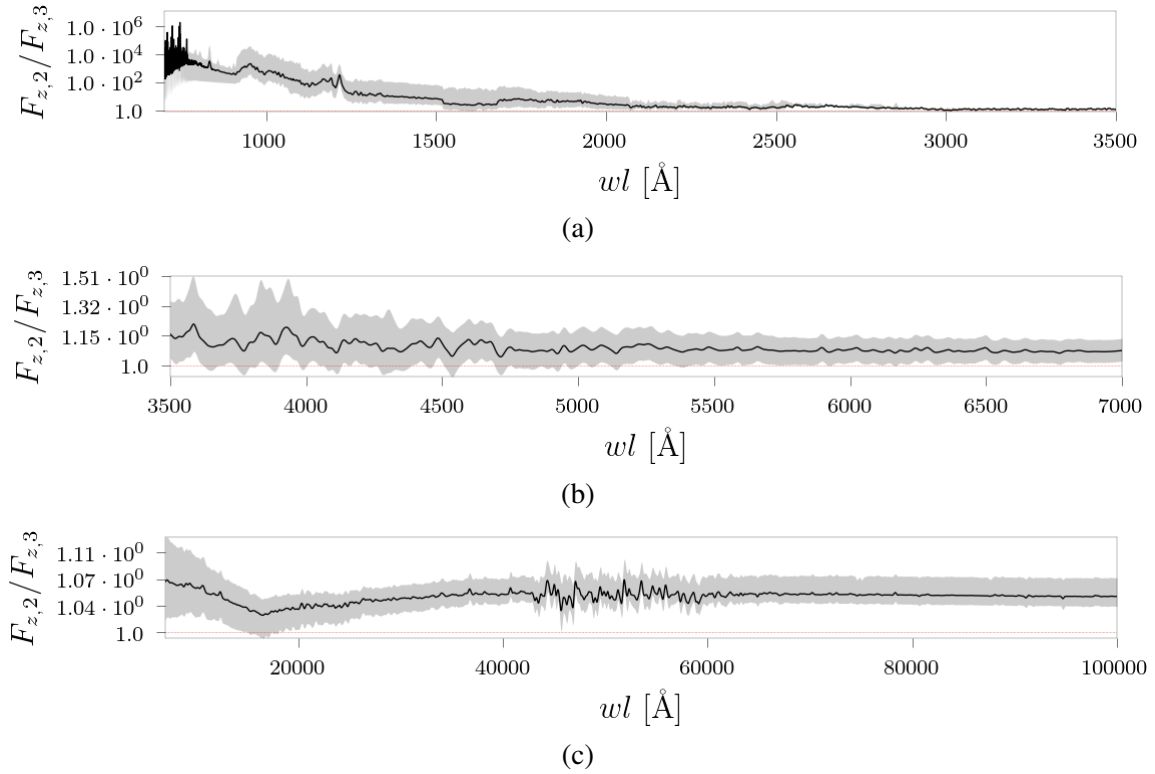
Temperature T vs. altitude z (a) and pressure p vs. altitude z (b)

The vertical temperature and density profiles for model 3 (red solid line) as well as the corresponding layer averaged mean (blue dotted line) profile for model 2. The pallid blue coloured regions span between their respective layer averaged minimum and maximum profiles.

The differences in the model structures can readily be understood by inspection of figs. 3.25a and 3.25b showing the vertical temperature and density profiles for model 3 as well as the corresponding mean, minimum and maximum profiles for model 2 (representing both 3D models' hydrodynamic structures). For comparability the radius information for the 1D model was shifted such that the temperature at its deepest layer corresponds to a layer of similar layer averaged mean temperature in the 3D model. The temperature profiles match very well in the convection zone and demonstrate only small deviations in the photosphere. Starting at about 700 km the temperature corresponding to model 3 drops significantly below the layer averaged mean temperature of model 2 and closes in on the latter's layer averaged minimum temperature.

The densities of both models are similar for large parts of the atmosphere but differ, once again, notably at higher altitudes.

Figure 3.26



Inter-model flux-ratio $F_{z,2}/F_{z,3}$ vs. wavelength λ

The surface averaged vertical directed flux of model 2 divided by the surface flux of model 3 in the ultra-violet (a), visible (b) and infrared (c) wavelength range. The solid lines represent the corresponding mean values, while the pallid region cover the respective minimum to maximum values.

The subscripts 2 and 3 refer to their associated models and the red dotted line in the bottom panel is a visual guideline representing unity.

Figures 3.26a to 3.26c present the ratios between model 3's surface flux and the mean, maximum and minimum surface averaged surface flux of model 2 in the ultra-violet, visible and infrared wavelength ranges, respectively.

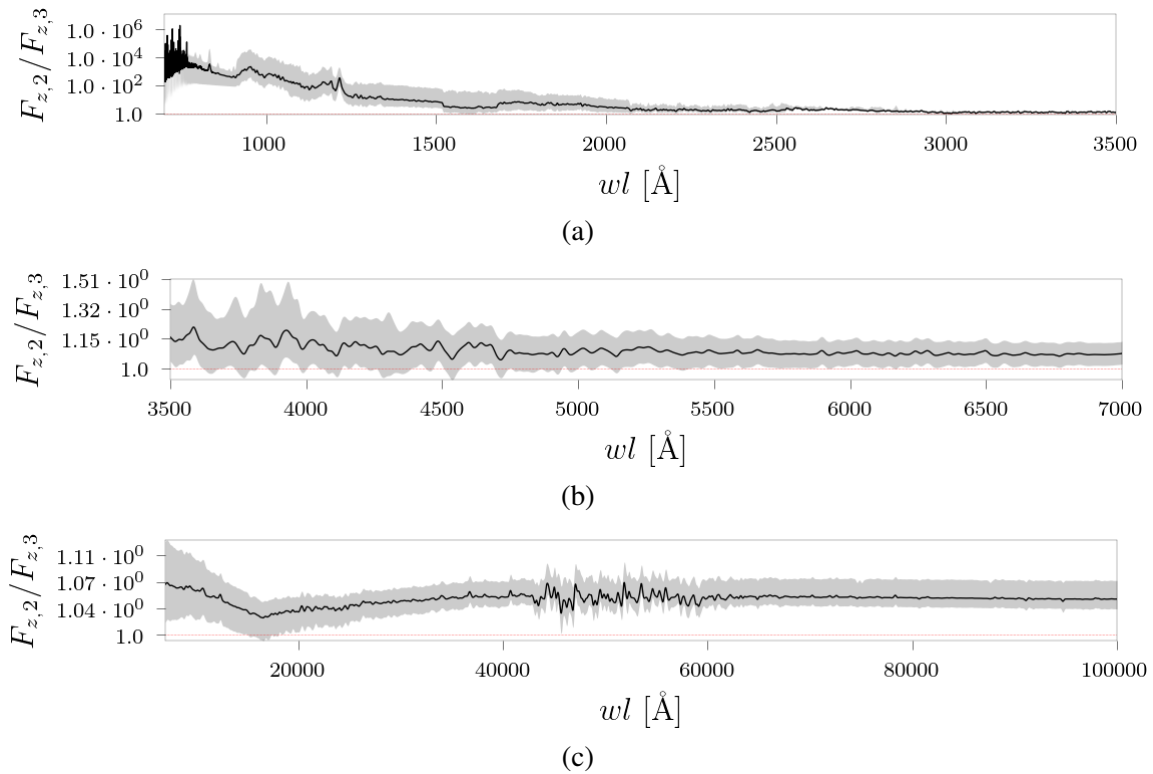
It takes little effort to identify both proposed differences in the flux ratios. Model 2 exhibits a surface flux increase with respect to model 3 throughout all wavelength ranges. The most substantial flux deviations can be found in the ultra-violet wavelength regime as the flux ratio steadily increases towards smaller wavelength and demonstrates relative differences of up to 4 magnitudes. It is, nevertheless, worth to remember that the absolute flux values in these regions tend to be rather small for Sun-like atmospheres and barely contribute to the integrated flux.

The flux ratios in the visible wavelength range, displayed in fig. 3.26b, vary slightly about

the value 1.15, stabilizing and slowly decreasing further to about 1.07 in the infrared. It is interesting that the ratio of the surface averaged minimum flux with respect to the 1D surface flux is very close to unity for large parts of this wavelength range.

In the infrared wavelength range the mean flux ratio decreases to about 1.02 at about 16542 Å and rises again to about 1.05. Except for distinct but minor variations in the region between 45000 Å and 60000 Å this value does not change significantly in the depicted range.

Figure 3.27



Inter-model flux-ratio $F_{z,1}/F_{z,3}$ vs. wavelength λ

The surface averaged vertical directed flux of model 1 divided by the surface flux of model 3 in the ultra-violet (a), visible (b) and infrared (c) wavelength range. The solid lines represent the corresponding mean values, while the pallid region cover the respective minimum to maximum values.

The subscripts 1 and 3 refer to their associated models and the red dotted line in the bottom panel is a visual guideline representing unity.

Demonstrating very similar behaviour, the surface flux ratios between model 3 and model 1 will not be discussed in detail but are presented in figs. 3.27a to 3.27c for reference.

Summarising, we find notable differences between the 3D and the 1D models in all wavelength ranges. The massive flux deviation in the ultra-violet is a direct consequence of the additionally

considered part of the chromosphere in the 3D models. We also observed distinct surface flux differences in the visible and infrared. Yet, these differences may be heavily snapshot dependent and have to be expected to vary not only with time, but also with the magnetic field strength. The explicit treatment of the chromosphere in models 1 and 2 should result in systematic deviations from the one-dimensional models, nonetheless.

CHAPTER 4

RESULTS AND FUTURE PROSPECTS

In the sections 3.1, 3.2.1, 3.2.2 and 3.3 we investigated the hydrodynamic and radiative properties of two models based on a three-dimensional magnetohydrodynamic structure of a Sun-like atmosphere.

This structure demonstrated the expected turbulent behaviour and, consequentially, exhibited a huge spread in thermodynamic properties with respect to their layer averaged mean values of temperature, gas pressure and density. It is apparent that a description of a 3D structure in terms of a layer averaged mean is bound to be incomplete and may even be inadequate at times, best seen in fig. 3.5 demonstrating the temperature stratification in a histogram.

The thermodynamic quantities also hinted at the existence of three distinctly different regions within the model's atmosphere, which were labelled and related to the convection zone, the photosphere and the lower chromosphere. Analyses of the radiation field throughout sections 3.2.1, 3.2.2 and 3.3 repeatedly affirmed the validity of the proposed transition-regions at about 0 km and 500 km vertical depth and their associated zones in the model structure.

Furthermore, we had a look at the thermodynamic quantities at different resolutions and found a perceivable but by no means enormous reduction in the quantities' contrast. While the decrease of the structure's resolution obviously lead to minor deviations from its origin and between the two input structures of models 1 and 2, their relative differences are small but not negligible when compared to the impact of differing species treated in NLTE.

Interestingly enough, the 1D model's temperature structure is in rather good agreement with the layer averaged mean temperature of the hydrodynamic structures of the 3D models for large parts of the photosphere but deviates exceedingly towards the layer averaged minimum of the 3D models in the 1D model's outermost layers. While the similarities in the photosphere had to be expected and are in fact reassuring with respect to the quality of, both, the one- and the

three-dimensional atmosphere modelling, an actual time and layer averaged mean of the latter could potentially resemble the one-dimensional structure even better. However, the deviations at higher altitudes can be explained just as well, since Phoenix/1D does not attempt to generate a chromospheric structure and, thus, it can not feature its properties sufficiently.

Moreover, we inspected and analysed the general LTE and NLTE flux properties of both 3D models, discussed a number of representative lines and, lastly, compared their synthetic spectra with one another and with the formerly mentioned 1D model. These results can be summarised by stating that the NLTE treatment of important atomic species has a notable impact on the associated line depths and shapes, most notably for the lines $H\alpha$ (models 1 and 2) and Ca II H and K (model 1). The remarkable non-locality of the radiation field and its associated quantities, like the source function, has been exhibited repeatedly and illustrates the importance of the NLTE treatment. Furthermore, the NLTE treatment also induces significant changes in the continua of the ultra-violet part of the spectrum.

Comparing models 1 and 2 we found considerable differences between their respective, surface averaged flux values in all wavelength ranges. This is especially true in the visible wavelength range demonstrating relative flux deviations of almost constantly 9% and about 7% in the infrared. This suggests that the (additional) treatment of iron and its ionisation stages does have a significant effect on the models properties and its radiation field. This statement is also supported by the notable deviations in the inter-model ratios of the number densities for important continuum species, like electrons and negative hydrogen displayed in fig. 3.24.

In addition, the deviations between the 1D model and the 3D models are notable but, thankfully, they are not large enough to render the former invalid for most applications, like debris disks. This is a saving grace from a practical point of view, since the simulation of such detailed 3D NLTE radiative transfer models is vastly more expensive in terms of computational resources.

On the one hand, debris disks are typically observed in the far infrared regime in which the relative differences of the mean flux between the models are of the order of a several percent. Serving only as the host star reference flux in the infrared, such small deviations are usually of minor importance for the determination of the disks properties. On that account, the 3D model results may be used to estimate the magnitude of the errors induced by the one-dimensional

treatment of the atmosphere.

On the other hand, the systematic deviations from the one-dimensional models may indeed change the outcome of debris disk models to some degree, since contributions from all wavelength ranges have to be considered.

The models discussed above outline the capabilities of today's state of the art radiative transfer and magnetohydrodynamic simulations. That being said, there is still room and reason for improvement for, both, the magnetohydrodynamic and the radiative transfer models.

Firstly, the presented models could be readily enhanced by expending the number of species (and ionisation stages) treated in NLTE, e.g., by including iron in addition to hydrogen, helium, carbon, nitrogen, oxygen, magnesium and calcium. It is reasonable to assume that such an expansion will lead in a rapprochement of the results of models 1 and 2. However, it is impossible to predict the actual outcome beforehand but the calculation of such model is unfortunately infeasible nowadays due to computing time and memory limitations.

Secondly, it would be invaluable to calculate the 3D radiative transfer for a number of different points in time and with different magnetic field strength for the hydrodynamic model to get a hold on its variability and to derive meaningful time averages.

While the treatment of arbitrary velocity fields have already been implemented in Phoenix/3D, enabling this option would considerably raise the memory demand, yet again. Furthermore, it would be beneficial to lift the complete redistribution assumption since it is known to break down for lines like $\text{Ly}\alpha$, Ca II h&k and Mg II h&k, all of which are important indicators for many different stellar properties. Once more, it is the significant increase in required computational resources that prevents us from solving the radiative transfer problem using the physically correct but usually overcomplicated partial redistribution formulation.

Additionally, we know that the magnetohydrodynamic structures were calculated using the one-fluid approximation supported by a simple radiative transfer. One of the major restrictions in the one-fluid approximation is the fact that the relative abundances of all elements are immutable at all points and for all times within the computational domain. While this approximation drastically reduces the number of equations and, therefore, the computational demand, it begins to break down in optically thin regions of stellar atmospheres. Since the thermodynamic properties vary rapidly in the photosphere and above, notable local differences in the chemical

composition have to be expected. In addition, the non-locality of the radiation field can couple physically disjoint regions in the structure and may, thereby, cause NLTE excitations and ionisations of atomic and molecular species.

Such deviations are clearly visible in the number densities, on the one hand, and the drastic change in the NLTE radiation field of the radiative transfer models presented above, on the other hand, and point at the intrinsic problem with these prerequisites. That is to say that the relative abundances depend on the local properties of the thermodynamic quantities and the non-local radiation field. This demonstrates why it would be useful to apply a multi-fluid approach coupled to a detailed NLTE radiative transfer solver to simulate consistent magnetohydrodynamic structures.

It is, however, difficult to judge the actual impact of these approximations on the structure and the resulting radiation field. Thus, it is likely that these and other problems may need to be revised in the future, since the lack of computational power and, likewise, absence of a suitable code render such task impractical as of today.

While the models described above were calculated under the constraints of many approximation, we find that their results match our expectations to a high degree and describe the underlying physics of a Sun-like atmosphere and its radiation field very well.

LIST OF FIGURES

3.1	Gas temperature T [K] of structure 1	37
3.2	Z-map $z(iz)$ and its gradient $d z(iz)/d iz$ per layer iz	38
3.3	Gas temperature T vs. altitude z	40
3.4	Gas pressure P_{gas} and particle density ρ vs. altitude z	41
3.5	Color-coded 3D (a) and 2D (b) temperature histogram-data	41
3.6	Surface flux F_z vs. wavelength λ and NLTE to LTE surface flux ratio F_z/F_z^* vs. wavelength λ for crefexample:pm32	47
3.7	Vertical directed flux F_z^* in LTE , vertical directed flux F_z in NLTE and the NLTE to LTE ratios F_z/F_z^* around the line centre of $H\alpha$ for model 1	48
3.8	Vertical directed flux F_z vs. latitude y in NLTE at the surface, a color-map of the source function S , the NLTE to LTE vertical directed flux ratios F_z/F_z^* vs. latitude y at the surface and a color-map of the reduced NLTE to LTE source function ratio $(S/S^*) - 1$ in the line centre of $H\alpha$ for an arbitrary vertical slice through model 1	49
3.9	Vertical directed flux F_z^* in LTE, vertical directed flux F_z in NLTE and the NLTE to LTE ratios F_z/F_z^* around the line centre of the Ca II K line for model 1	51
3.10	Vertical directed flux F_z vs. latitude y in NLTE at the surface, a color-map of the source function S , the NLTE to LTE vertical directed flux ratios F_z/F_z^* vs. y at the surface and a color-map of the reduced NLTE to LTE source function ratio $(S/S^*) - 1$ in the line centre of the Ca II K line for an arbitrary vertical slice through model 1	52
3.11	Vertical directed flux F_z^* in LTE, vertical directed flux F_z in NLTE and the NLTE to LTE ratios F_z/F_z^* around the line centre of the Mg II K line for model 1	53

3.12	Vertical directed flux F_z vs. latitude y in NLTE at the surface, a color-map of the source function S , the NLTE to LTE vertical directed flux ratios F_z/F_z^* vs. latitude y at the surface and a color-map of the reduced NLTE to LTE source function ratio $(S/S^*) - 1$ in the line centre of the Mg II K line for an arbitrary vertical slice through model 1	54
3.13	Surface flux F_z vs. wavelength λ and NLTE to LTE surface flux ratio F_z/F_z^* vs. wavelength λ for crefexample:pm16	56
3.14	Vertical directed flux F_z^* in LTE, vertical directed flux F_z in NLTE and the NLTE to LTE ratios F_z/F_z^* around the line centre of H α for model 2	57
3.15	Vertical directed flux F_z vs. latitude y in NLTE at the surface, a color-map of the source function S , the NLTE to LTE vertical directed flux ratios F_z/F_z^* vs. latitude y at the surface and a color-map of the reduced NLTE to LTE source function ratio $(S/S^*) - 1$ in the line centre of H α for an arbitrary vertical slice through model 2	58
3.16	Vertical directed flux F_z^* in LTE, vertical directed flux F_z in NLTE and the NLTE to LTE ratios F_z/F_z^* around the line centre of the Fe e-line for model 2	59
3.17	Vertical directed flux F_z vs. latitude y in NLTE at the surface, a color-map of the source function S , the NLTE to LTE vertical directed flux ratios F_z/F_z^* vs. latitude y at the surface and a color-map of the reduced NLTE to LTE source function ratio $(S/S^*) - 1$ in the line centre of Fe e-line for an arbitrary vertical slice through model 2	60
3.18	Vertical directed flux F_z^* in LTE, vertical directed flux F_z in NLTE and the NLTE to LTE ratios F_z/F_z^* around the Fe II line centred at 4585.1 Å for model 2	62
3.19	Vertical directed flux F_z vs. latitude y at the surface and in NLTE and in LTE, a color-map of the respective source functions S , the NLTE to LTE vertical directed flux ratios F_z/F_z^* vs. latitude y at the surface and a color-map of the reduced NLTE to LTE source function ratio $(S/S^*) - 1$ in the line centre of the Fe II line centred at 4585.1 Å for an arbitrary vertical slice through model 2	63
3.20	Layer averaged mean temperature ratio T_2/T_1 vs. altitude z	64
3.21	Surface averaged vertical directed flux F_z for model 1 and model 2 and their ratios $F_{z,2}/F_{z,1}$	66

3.22	Number density n of H^- vs. altitude z of model 2 and the mean number density ratio n_2/n_1 vs. altitude z as compared to model 1	68
3.23	Occupation number n_i for hydrogen in its second excited state and electron number density n_e (b, top) vs. altitude z for model 2 and their respective mean ratios $n_{i,2}/n_{i,1}$ and $n_{e,2}/n_{e,1}$ as compared to model 1	69
3.24	Number densities n vs. altitude z of model 2 and their absolute differences normalised to the electron number density $(n_2 - n_1)/n_{e,2}$ vs. altitude z as compared to model 1	71
3.25	Temperature T vs. altitude z and pressure p vs. altitude z	73
3.26	Inter-model flux-ratio $F_{z,2}/F_{z,3}$ vs. wavelength λ	74
3.27	Inter-model flux-ratio $F_{z,1}/F_{z,3}$ vs. wavelength λ	75

LIST OF TABLES

3.1	List of general model properties	43
-----	--	----

BIBLIOGRAPHY

Ivan De Gennaro Aquino. *3D NLTE Radiative Transfer Modelling of M-dwarf Atmospheres*. PhD thesis, Universität Hamburg, Von-Melle-Park 3, 20146 Hamburg, 2016. URL <http://ediss.sub.uni-hamburg.de/volltexte/2017/8368>.

Alexander Berkner. *3D Super Level non-LTE Radiative Transfer for Molecules*. PhD thesis, Universität Hamburg, Von-Melle-Park 3, 20146 Hamburg, 2015. URL <http://ediss.sub.uni-hamburg.de/volltexte/2015/7186>.

C. J. Cannon. Angular quadrature perturbations in radiative transfer theory. *jqsrt*, 13:627–633, 1973. doi: 10.1016/0022-4073(73)90021-6.

Claudio Chiuderi and Marco Velli. *Basics of Plasma Astrophysics (UNITEXT for Physics)*. Springer, 2016. ISBN 8847058708. URL <https://www.amazon.com/Basics-Plasma-Astrophysics-UNITEXT-Physics/dp/8847058708?SubscriptionId=0JYN1NVW651KCA56C102&tag=techkie-20&linkCode=xm2&camp=2025&creative=165953&creativeASIN=8847058708>.

J. Fraunhofer. Bestimmung des Brechungs- und des Farben-Zerstreuungs-Vermögens verschiedener Glasarten, in Bezug auf die Vervollkommnung achromatischer Fernröhre. *Denkschriften der Königlichen Akademie der Wissenschaften zu München*, 5:193–226, 1817. URL <https://books.google.de/books?id=2-AAAAAYAAJ>.

B. Freytag, M. Steffen, H.-G. Ludwig, S. Wedemeyer-Böhm, W. Schaffenberger, and O. Steiner. Simulations of stellar convection with CO5BOLD. *Journal of Computational Physics*, 231: 919–959, February 2012. doi: 10.1016/j.jcp.2011.09.026.

Birgit Fuhrmeister. *Chromospheric and coronal activity : Analysing optical spectra of M dwarfs*. PhD thesis, Universität Hamburg, Von-Melle-Park 3, 20146 Hamburg, 2005. URL <http://ediss.sub.uni-hamburg.de/volltexte/2005/2651>.

- P. H. Hauschildt and E. Baron. A 3D radiative transfer framework. I. Non-local operator splitting and continuum scattering problems. *aap*, 451:273–284, May 2006. doi: 10.1051/0004-6361:20053846.
- P. H. Hauschildt and E. Baron. A 3D radiative transfer framework. XI. Multi-level NLTE. *aap*, 566:A89, June 2014. doi: 10.1051/0004-6361/201423574.
- P.H. Hauschildt. Multi-level non-lte radiative transfer in expanding shells. *Journal of Quantitative Spectroscopy and Radiative Transfer*, 50(3):301 – 318, 1993. ISSN 0022-4073. doi: [https://doi.org/10.1016/0022-4073\(93\)90080-2](https://doi.org/10.1016/0022-4073(93)90080-2). URL <http://www.sciencedirect.com/science/article/pii/0022407393900802>.
- I. Hubeny and B.W. Lites. Partial redistribution in multilevel atoms. i. method and application to the solar hydrogen line formation. *Astrophysical Journal*, 455(1), 12 1995. doi: 10.1086/176584.
- Ivan Hubeny and Dimitri Mihalas. *Theory of Stellar Atmospheres: An Introduction to Astrophysical Non-equilibrium Quantitative Spectroscopic Analysis (Princeton Series in Astrophysics)*. Princeton University Press, 2014. ISBN 0691163286. URL <https://www.amazon.com/Theory-Stellar-Atmospheres-Astrophysical-Non-equilibrium/dp/0691163286?SubscriptionId=0JYN1NVW651KCA56C102&tag=techkie-20&linkCode=xm2&camp=2025&creative=165953&creativeASIN=0691163286>.
- G. R. Kirchhoff. *Untersuchungen über das Sonnenspectrum und die Spectren der chemischen Elemente*. Ferd. Dümmler’s Verlagsbuchhandlung, 1862-1863. doi: <http://dx.doi.org/10.3931/e-rara-59403>. Provided by the ETH-Bibliothek Zürich.
- Sebastian Knop. *General Relativistic Radiative Transfer*. PhD thesis, Universität Hamburg, Von-Melle-Park 3, 20146 Hamburg, 2007. URL <http://ediss.sub.uni-hamburg.de/volltexte/2007/3375>.
- Alexander V. Krivov. Debris disks: seeing dust, thinking of planetesimals and planets. *Research in Astronomy and Astrophysics*, 10:383–414, May 2010. doi: 10.1088/1674-4527/10/5/001.
- J. Leenaarts and S. Wedemeyer-Böhm. Time-dependent hydrogen ionisation in 3d simulations of the solar chromosphere - methods and first results. *A&A*, 460(1):301–307, 2006. doi: 10.1051/0004-6361:20066123. URL <https://doi.org/10.1051/0004-6361:20066123>.

- D. H. Menzel and G. G. Cillié. Hydrogen Emission in the Chromosphere. *apj*, 85:88, March 1937. doi: 10.1086/143804.
- Marlies Meyer. *A new EOS module for the atmosphere modelling code PHOENIX*. PhD thesis, Universität Hamburg, Von-Melle-Park 3, 20146 Hamburg, 2017. URL <http://ediss.sub.uni-hamburg.de/volltexte/2017/8643>.
- D. Mihalas. *Stellar atmospheres /2nd edition/*. W H Freeman and Co, 1978.
- Dimitri Mihalas and Barbara Weibel Mihalas. *Foundations of Radiation Hydrodynamics (Dover Books on Physics)*. Dover Publications, 2013. URL <https://www.amazon.com/Foundations-Radiation-Hydrodynamics-Dover-Physics-ebook/dp/B00A73FN70?SubscriptionId=0JYN1NVW651KCA56C102&tag=techkie-20&linkCode=xm2&camp=2025&creative=165953&creativeASIN=B00A73FN70>.
- Joachim Oxenius. *Kinetic Theory of Particles and Photons : Theoretical Foundations of Non-LTE Plasma Spectroscopy*. Springer Berlin Heidelberg, Berlin, Heidelberg, 1986. ISBN 978-3-642-70728-5.
- A. Schuster. Radiation Through a Foggy Atmosphere. *apj*, 21:1, January 1905. doi: 10.1086/141186.
- Andreas Schweitzer, Peter H. Hauschildt, and E. Baron. Non-LTE treatment of molecules in the photospheres of cool stars. *The Astrophysical Journal*, 541(2):1004–1015, oct 2000. doi: 10.1086/309461. URL <https://doi.org/10.1086%2F309461>.
- William R. Smith and Ronald W. Missen. *Chemical Reaction Equilibrium Analysis*. Wiley, 1982. ISBN 0471093475. URL <https://www.amazon.com/Chemical-Reaction-Equilibrium-Analysis-William/dp/0471093475?SubscriptionId=AKIAIOBINVZYXZQZ2U3A&tag=chimbori05-20&linkCode=xm2&camp=2025&creative=165953&creativeASIN=0471093475>.
- Boris V. Somov. *Plasma Astrophysics, Part I: Fundamentals and Practice: 391 (Astrophysics and Space Science Library)*. Springer, 2012. URL <https://www.amazon.com/Plasma-Astrophysics-Part-Fundamentals-Practice-ebook/dp/B00BLS4VIC?SubscriptionId=0JYN1NVW651KCA56C102&tag=techkie-20&linkCode=xm2&camp=2025&creative=165953&creativeASIN=B00BLS4VIC>.

- E. Staath and P. Lemaire. High resolution profiles of the MG II H and MG II K lines. *aap*, 295: 517–528, March 1995.
- Viotti, Roberto, Vittone, A. Alberto, and M. Friedjung. *Physics of Formation of FeII Lines Outside LTE: Proceedings of the 94th Colloquium of the International Astronomical Union Held in Anacapri, Capri ... 1986 (Astrophysics and Space Science Library)*. Springer, 2014. ISBN 9401082855. URL <https://www.amazon.com/Physics-Formation-FeII-Lines-Outside/dp/9401082855?SubscriptionId=AKIAIOBINVZYXZQZ2U3A&tag=chimbori05-20&linkCode=xm2&camp=2025&creative=165953&creativeASIN=9401082855>.
- S. Wedemeyer-Böhm, E. Scullion, O. Steiner, L. Rouppe van der Voort, J. de La Cruz Rodriguez, V. Fedun, and R. Erdélyi. Magnetic tornadoes as energy channels into the solar corona. *nat*, 486:505–508, June 2012. doi: 10.1038/nature11202.
- Sven Wedemeyer-Böhm. personal communication, 2015.
- Sven Wedemeyer-Böhm. personal communication, 2017.
- Sven Wedemeyer-Böhm, Eamon Scullion, Oskar Steiner, Luc Rouppe van der Voort, Jaime de la Cruz Rodriguez, Viktor Fedun, and Robert Erdélyi. Magnetic tornadoes as energy channels into the solar corona. *Nature*, 486:505 EP –, 06 2012. URL <http://dx.doi.org/10.1038/nature11202>.
- Viktoría Wichert. *Numerical Radiation Transport Algorithms for Emergent Computer Architectures*. PhD thesis, Universität Hamburg, Von-Melle-Park 3, 20146 Hamburg, 2019, in prep.
- W.H. Wollaston. A Method of examining refractive and dispersive Powers, by prismatic Reflection. *Philosophical Transactions of the Royal Society*, 92:365–380, June 1802. doi: <http://doi.org/10.1098/rstl.1802.0014>.

Eidesstattliche Versicherung / Declaration on oath

Hiermit versichere ich an Eides statt, die vorliegende Dissertationsschrift selbst verfasst und keine anderen als die angegebenen Hilfsmittel und Quellen benutzt zu haben.

Die eingereichte schriftliche Fassung entspricht der auf dem elektronischen Speichermedium.

Die Dissertation wurde in der vorgelegten oder einer ähnlichen Form nicht schon einmal in einem früheren Promotionsverfahren angenommen oder als ungenügend beurteilt.

Hamburg, den ____ . ____ . 2019

Mario Arkenberg